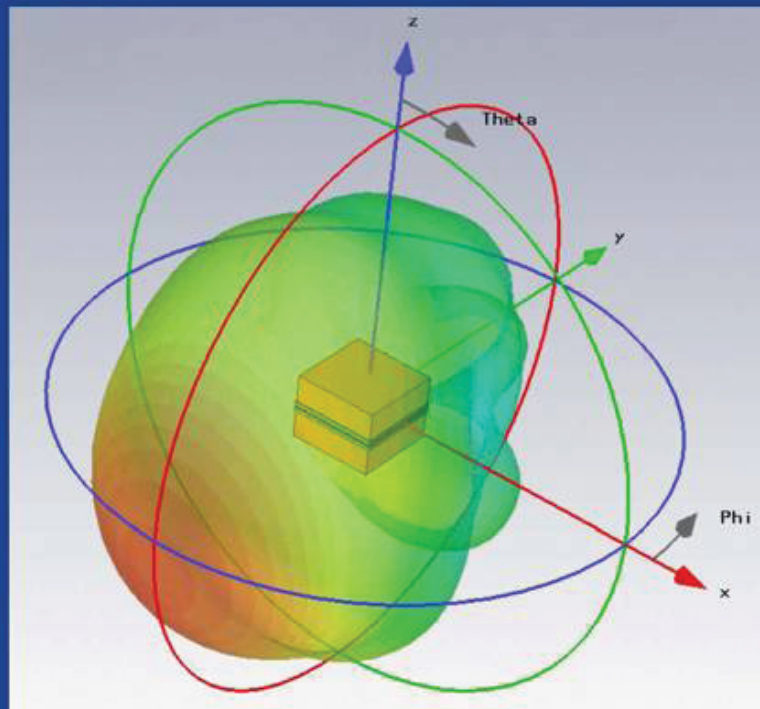


Finite-Difference-Frequency-Domain
Simulation of Electrically Large Micro-
wave Structures using PML and
Internal Ports



aus der Reihe:

Innovationen mit Mikrowellen und Licht

Forschungsberichte aus dem Ferdinand-Braun-Institut für Höchstfrequenztechnik

Band 7

Prodyut Kumar Talukder

Finite-Difference-Frequency-Domain Simulation of Electrically
Large Microwave Structures using PML and Internal Ports

Herausgeber: Prof. Dr. Günther Tränkle, Prof. Dr.-Ing. Wolfgang Heinrich

Ferdinand-Braun-Institut
für Höchstfrequenztechnik (FBH)

Gustav-Kirchhoff-Straße 4
12489 Berlin

Tel. +49.30.6392-2600
Fax +49.30.6392-2602

E-Mail fbh@fbh-berlin.de
Web www.fbh-berlin.de

Innovationen mit Mikrowellen und Licht

Forschungsberichte aus dem Ferdinand-Braun-Institut für Höchstfrequenztechnik

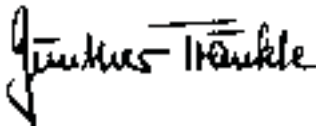
Vorwort der Herausgeber

Neue Ideen, Entwicklungen und Konzepte aus der Forschung sind die Basis von Fortschritt und Wettbewerbsfähigkeit. Als Inventionen erweitern sie den Stand des Wissens und der Technik, als innovative Produkte und Dienstleistungen schließlich findet ein Teil von ihnen Eingang in unsere Alltagswelt.

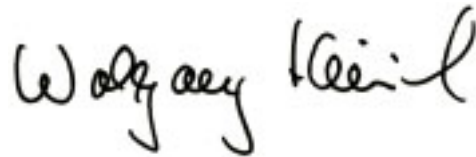
In diesem Sinne dokumentiert die Reihe „*Forschungsberichte aus dem Ferdinand-Braun-Institut für Höchstfrequenztechnik*“ aktuelle Forschungen und Entwicklungen aus dem Institut. Wir möchten Ihnen diese Ergebnisse zugänglich machen und zur weiteren Diskussion anregen – nicht zuletzt, damit möglichst viele Entwicklungen zu einem Teil unseres Alltags werden.

Der vorliegende Beitrag beschäftigt sich mit einem Thema aus dem Bereich der elektromagnetischen Simulation, der Verbesserung der offenen Randbedingung (PML) im Rahmen der Finite-Differenzen-Methode im Frequenzbereich. Auf diesem Gebiet wurden in den letzten Jahren große Fortschritte erzielt, allerdings gibt es auch – was weniger zur Sprache kommt – noch eine Reihe von Problemen, die in der vorliegenden Arbeit aufgegriffen werden.

Eine anregende Lektüre wünschen



Prof. Dr. Günther Tränkle
Direktor



Prof. Dr.-Ing. Wolfgang Heinrich
stellvertretender Direktor

Das Ferdinand-Braun-Institut

Das Ferdinand-Braun-Institut für Höchstfrequenztechnik erforscht elektronische und optische Komponenten, Module und Systeme auf der Basis von Verbindungshalbleitern. Diese sind Schlüsselbausteine für Innovationen in den gesellschaftlichen Bedarfsfeldern Kommunikation, Energie, Gesundheit und Mobilität. Leistungsstarke und hochbrillante Diodenlaser, UV-Leuchtdioden und hybride Lasersysteme entwickelt das Institut vom sichtbaren bis zum ultravioletten Spektralbereich. Die Anwendungsfelder reichen von der Medizintechnik, Präzisionsmesstechnik und Sensorik bis hin zur optischen Satellitenkommunikation. In der Mikrowellentechnik realisiert das FBH hocheffiziente, multifunktionale Verstärker und Schaltungen, unter anderem für energieeffiziente Mobilfunksysteme und Komponenten zur Erhöhung der Kfz-Fahrsicherheit. Kompakte atmosphärische Mikrowellenplasmaquellen mit Niederspannungsversorgung entwickelt es für medizinische Anwendungen, etwa zur Behandlung von Hauterkrankungen.

Das FBH ist ein international anerkanntes Zentrum für III/V-Verbindungshalbleiter mit allen Kompetenzen: vom Entwurf, über die Fertigung bis hin zur Charakterisierung von Bauelementen.

Seine Forschungsergebnisse setzt das FBH in enger Zusammenarbeit mit der Industrie um und transferiert innovative Produktideen und Technologien erfolgreich durch Spin-offs. In strategischen Partnerschaften mit der Industrie sichert es in der Höchstfrequenztechnik die technologische Kompetenz Deutschlands.

Finite-Difference-Frequency-Domain Simulation of Electrically Large Microwave Structures using PML and Internal Ports

vorgelegt von

M.Sc. Eng. Prodyut Kumar Talukder¹
aus Netrakona in Bangladesh

von der Fakultät IV - Elektrotechnik und Informatik -
der Technischen Universität Berlin
zur Erlangung des akademischen Grades

Doktor der Ingenieurwissenschaften
- Dr.-Ing. -

genehmigte Dissertation

Promotionsausschuss:

Vorsitzender: Prof. Dr.-Ing. Heino Henke

1. Gutachter: Prof. Dr.-Ing. Wolfgang Heinrich

2. Gutachter: Prof. Dr.-Ing. Georg Böck

Tag der wissenschaftlichen Aussprache: 30. Januar 2009

Berlin 2009
D-83

¹Ferdinand-Braun-Institut für Höchstfrequenztechnik, Berlin-Adlershof

Bibliografische Information der Deutschen Nationalbibliothek

Die Deutsche Nationalbibliothek verzeichnet diese Publikation in der Deutschen Nationalbibliografie; detaillierte bibliografische Daten sind im Internet über <http://dnb.ddb.de> abrufbar.

1. Aufl. - Göttingen : Cuvillier, 2009
Zugl.: (TU) Berlin, Univ. Diss., 2009

978-3-86955-067-1

© CUVILLIER VERLAG, Göttingen 2009
Nonnenstieg 8, 37075 Göttingen
Telefon: 0551-54724-0
Telefax: 0551-54724-21
www.cuvillier.de

Alle Rechte vorbehalten. Ohne ausdrückliche Genehmigung des Verlages ist es nicht gestattet, das Buch oder Teile daraus auf fotomechanischem Weg (Fotokopie, Mikrokopie) zu vervielfältigen.

1. Auflage, 2009
Gedruckt auf säurefreiem Papier

978-3-86955-067-1

*To my parents (Gita Rani Roy and Khagendra Nath Talukder),
my sister (Moumita Talukder) and my wife (Aditi Gupta)*

Acknowledgements

I sincerely acknowledge the Ferdinand-Braun-Institut für Höchstfrequenztechnik, Berlin (FBH) for providing me the opportunity to pursue my PhD. I am indebted to all the individuals of the Microwave Engineering Department for their cooperation and a healthy team work.

I incessantly express my gratitude to Prof. Dr.-Ing. Wolfgang Heinrich for his generous teaching. His insightful scientific approach directed me to professionalism and helped me to understand the complex aspects of the thesis work.

I am grateful to Dr.-Ing. Franz-Josef Schmückle for his guidance and unbounded support throughout my PhD work. Thanks to his presence and his valuable advices on the thesis work and personal matters.

My special thanks go to Dipl. Math. Rainer Schlundt for his valuable suggestions and easy-to-understand explanations of the F3D solver.

I gratefully remember the friendly and valuable assistance of Dr. Horst Zscheile, Dr.-Ing. Marco Kunze, Dr.-Ing. Thorsten Tischler and Dr.-Ing. Michael Buchta at the beginning of my work. Many thanks to Dr.-Ing. Nidhi Chaturvedi for her friendly suggestions during writing of the thesis.

Finally, I heartily acknowledge my inspirations, my parents, my sister and my wife for their love and affections. Special thanks to my wife for her personal motivation and support in the most struggling moments of my life.

Prodyut Kumar Talukder
06.03.2009

Contents

0.1	Abstract	1
0.2	Kurzfassung	3
1.	Introduction	5
1.1	Motivation	5
1.2	Finite Difference Frequency Domain (FDFD) Method	9
1.3	Anisotropic PML Absorbing Boundary Condition	10
1.4	Internal Ports	11
2.	PML Parameters and Convergence	13
2.1	Motivation and General Considerations	13
2.2	Overlapping PML Walls	18
2.3	PML Cell Size	23
	2.3.1 Single PML Wall: Micro-strip Structure	24
	2.3.2 Multiple PML Walls: Patch Antenna	29
	2.3.3 Slot Antenna	34
2.4	PML in Layered Media	35
2.5	Improved Numerical Solver	40
2.6	Conclusion	44
3.	Waveguide Port Simulation with PML	45
3.1	Physical and Artificial Modes	45
3.2	PML Modes and their Coupling to other Modes	51
3.3	Conclusion	55
4.	Internal Port	57
4.1	Relaxation Current Internal Port	58
4.2	Conduction Current Internal port (Line Current)	63
4.3	Parasitic Effects of Conduction Current Internal Ports	66
4.4	Analytical Formulation for the Parasitic Inductance	69
4.5	Simulation with Conduction Current Internal Port	74
	4.5.1 T-junction	74
	4.5.2 HEMT Structure	75
4.6	Conclusion	79

5.	4-Quadrant Slot Antenna	81
5.1	Introduction	81
5.2	Antenna Design	82
5.3	Simulation Results with FDFD	85
5.4	Realization and Measurement Results	91
5.5	Conclusion	95
6.	Summary	96
7.	Appendix	99
7.1	FDFD Discretization	99
7.2	PML Modes and their Coupling to other Modes	100
7.3	Excitation by Relaxation Current (Internal Port) Source	105
7.4	Excitation by Conduction Current (Internal Port) Source	107
7.5	Deembedding Conduction Current Internal Port Parasitics	109
7.6	Excitation with Waveguide Ports	112
7.7	Improvements in the F3D Solver	114
7.8	Acronyms and symbols	116
8.	Literature	119
9	Curriculum Vitae	123

0.1 Abstract

For EM simulations of complex MMIC structures, the usage of PML (Perfectly Matched Layer) absorbing boundary conditions is inevitable. PML provides a reflectionless open boundary condition and thus helps to keep the mesh size within a reasonable limit. On the other hand, structures completely enclosed by PML walls do not allow excitation by waveguide ports but require so-called internal ports. Such ports, which are introduced between two or more mesh points inside the structure, facilitate also to include lumped elements or entire networks thus enabling one to study active circuit, for instance.

This work treats both the PML boundary condition and the internal ports, in the framework of the frequency-domain Finite-Difference method (FDFD). It is shown that the presence of PML walls enlarges the magnitude range of the system matrix coefficients, encountered when calculating the fields. This makes the system matrix ill-conditioned and increases the number of iterations when solving the system and may even render this PML totally unusable for most practical applications. It is found that by avoiding any overlapping PML walls and by making the PML cell sizes the largest ones in the whole mesh the high count of the number of iterations can be lowered drastically.

The mode spectrum at waveguide ports with lateral PML walls consists of artificial PML and physical modes. We find that the coupling between PML modes and physical modes must be analyzed thoroughly in order to filter the artificial PML modes out in a reliable way.

Regarding the internal port, a line-current formulation proves to be the only practical choice. The parasitic inductances associated with it are found to be of significant influence. A closed-form expression for these inductances is developed in order to determine their values so that it can be deembedded from the results.

The optimized PML and internal port formulations are verified for the example of a 24 GHz slot antenna with integrated front-end MMIC, suitable for short range communications and sensor networks.

0.2 Kurzfassung

Bei Berechnungen des elektromagnetischen Verhaltens von komplexen MMIC-Strukturen ist die Verwendung von absorbierenden Randbedingungen in Form des sogenannten Perfectly Matched Layer (PML) unvermeidlich. Allseitig durch PML-Wände reflexionsfrei abgeschlossene Raumbereiche helfen die Anzahl der Diskretisierungszellen zu reduzieren. Sie lassen aber auch keine Wellenleitertore (mit Öffnungen in PML-Regionen) zu. In diesen Fällen sind interne Tore erforderlich. Derartige Tore erlauben darüber hinaus das Einbetten diskreter Elemente und ganzer Netzwerke und damit z.B. die Analyse aktiver Strukturen.

Diese Arbeit behandelt sowohl die PML-Randbedingung als auch die internen Tore und beschreibt ihr Verhalten im Rahmen des Finite-Differenzen-Verfahrens im Frequenzbereich (FDFD). Dabei werden insbesondere die unerwünschten parasitären Effekte ausführlich untersucht.

Zur Lösung des bei der FDFD-Methode auftretenden Gleichungssystems, das den Zusammenhang der elektromagnetischen Felder in der zu berechnenden Struktur beschreibt, wird ein iteratives (SSOR-)Verfahren benutzt. Die Konvergenz dieses Verfahrens wird sehr stark von der Kondition der Matrix bestimmt. Eine schlecht konditionierte Matrix vergrößert die Zahl der Iterationen und damit die Rechenzeit beträchtlich. Leider tritt dieser Fall bei der Anwendung von PML-Wänden deutlich in Erscheinung. Trotzdem kann die Zahl der Iterationen auf ein vernünftiges Maß beschränkt werden, wenn bestimmte Richtlinien eingehalten werden. In dieser Arbeit wurden verschiedene Möglichkeiten zur Reduzierung ansonsten hoher Iterationszahlen untersucht und bewertet, was von großem praktischen Nutzen ist.

In Strukturen, bei denen die PML-Wände als Berandung eines Wellenleiters eingesetzt werden, besteht das Modenspektrum (z.B. des entsprechenden Wellenleitertores) aus den physikalisch sinnvollen sowie aus unphysikalischen, künstlichen PML-Moden. Die künstlichen Moden lassen sich häufig durch geeignete Kriterien herausfiltern. Aber Beispiele zeigen, daß in vielen Fällen das Separieren physikalischer und künstlicher Moden nur nach einer umfassenden Betrachtung möglich ist.

Die Beschreibung interner Tore kann mit verschiedenen Ansätzen durchgeführt werden. Tatsächlich zeigt sich aber, daß nur der Ansatz mit der Linienstromformulierung praktikabel ist. Neben der reinen Implementierung werden in der vorliegenden Arbeit auch die parasitären Effekte wie die mit dem internen Tor verknüpften Induktivitäten diskutiert und Abschätzungsformeln entwickelt.

Abschließend wird der Einsatz der optimierten PML und der internen Tore am Beispiel einer 24 GHz-Schlitzantenne mit integriertem Frontend-MMIC, verwendbar für Kurzstreckenkommunikation und Sensor-Netze, demonstriert.

1 Introduction

1.1 Motivation

Mobile communications, satellite, radar, automobile and sensor technologies have fuelled the development of microwave integrated circuits (MMICs). For the growing demand of MMICs to work at higher frequencies, the miniaturisation of the circuit elements, i.e. the active and passive devices, is indispensable. Without proper and systematic design and optimisation of the circuit elements such MMIC's are not achievable. Since post-production changes are expensive and design cycles are short, accurate design tools are a must.

For the design and simulation essentially two important developments have emerged. On the one hand, there are network-oriented design simulators where active devices, lumped elements and simple passive distributed circuits are connected or interfaced. These simulators take into account only those coupling, mechanism known a priori and deal mostly with a single mode for transmission lines. It is very much important however to design the active and passive structures in such a way that any crosstalk and the dependencies between all modes are included. Presently simulation tools are offered which allow for deeper and thorough investigation of the electromagnetic fields and waves in passive structures. Such electromagnetic simulation tools (EM simulators) account for all the effects of the electromagnetic field behaviour, for example cross talk, surface waves, coupling effects and a series of other important issues.

The capabilities of the EM simulators have been extended significantly during the last decade, partly due to the advances in computer hardware, partly due to improvements in numerical mathematics with a various number of different approaches used. The most promising developments are Finite Differences (FD) and Finite Elements (FE), while in the beginning of these approaches simple assumptions were made to describe a structure, in the latest years more improvements arose which allow to cover the real nature of investigated structures more accurately. One of the most useful advances is the description of the open boundary. Using in the past electric and magnetic walls with all their disadvantages, e.g. error due to reflections from these walls, several new methods have been introduced approximating an open boundary, such that waves propagating to the direction of the boundary are absorbed by specially defined layers.

A preferable method in this sense is the Perfectly Matched Layer (PML) (Fig. 1.1) technique. It was introduced by Berenger [16] and, initially, is based on the splitting of Cartesian electric and magnetic field components into two subcomponents leading to a modified set of Maxwell's equations. Some of the limitations of this approach are indicated in [17, 19] and one of them is that the generating equations and thus fields in the PML medium are non-Maxwellian. Another approach of Chew and Weedon [22] is based on the incorporation of the complex coordinate stretching variables. In this case, Maxwell's equations are also to be modified and the complex co-ordinates provide no physical meaning. Alternatively, introduced by Sachs et al, a PML can be realized by introducing anisotropic material properties, with electric and magnetic conductivities, leading to permeability and permittivity tensors [3].

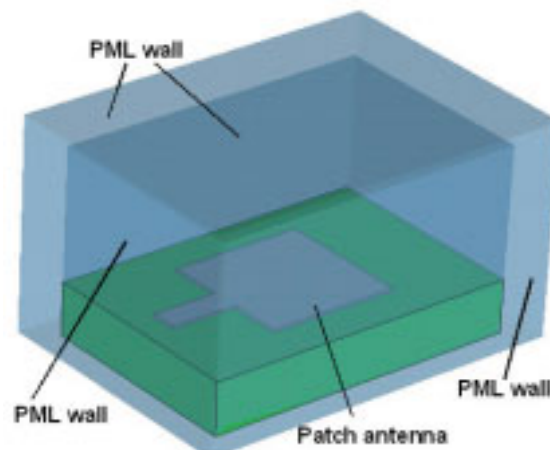


Fig. 1.1 Replacing the open boundaries of a patch antenna structure with the PML absorbing boundary conditions (PML walls) in order to absorb the radiations.

Today, PML forms a salient feature of all common 3D EM simulation methods, both in the time domain (FDTD [2,3], TLM [44]) and the frequency domain (finite-element method [45], FDFD). In the later case, mostly the anisotropic material approach [18] is applied because it can be easily implemented without any need to modify the basic equations.

However, the benefits of PML do not come for free. In the frequency-domain case, the material tensors worsen the numerical properties of the system of equations to be solved, which results in increased CPU time. In the time domain, mechanisms are not such clearly to be identified but similar effects are observed. Generally, the deteriorations depend strongly on the number and parameters of the PML layers and occur particularly if the PML layers overlap, e.g., at the edges and corners of the outer boundary of the computational domain.

Beyond this, PML gives rise to another problem, which is often overlooked in the literature: during waveguide port simulations, a PML boundary causes appearance of parasitic PML modes with complex propagation constants which must be dealt with attention in order to separate them from the desired physical modes. In [20, 25] a PPP (Power Part in PML) criterion is introduced for this separation. However, this does not give reliable results in all cases and further investigations are necessary to explore these effects.

Beside the PML definitions, another important feature of EM simulation methods is the implementation of so-called internal ports, which allow to feed the test structures internally. Like voltage or current sources internal ports are used to excite structures by placing them between two conducting lines (e.g. signal and ground lines) inside the structure. Unlike waveguide ports where a cross-section is defined on a boundary and a number of modes are excited, internal ports are based on a current-voltage description and thus can be used to interface the active / lumped circuit. Moreover, when a structure is surrounded by PML walls in all directions (e.g. Fig. 1.1), it is not possible to excite the structure by waveguide ports, the only option is the use of internal ports to excite the structure internally.

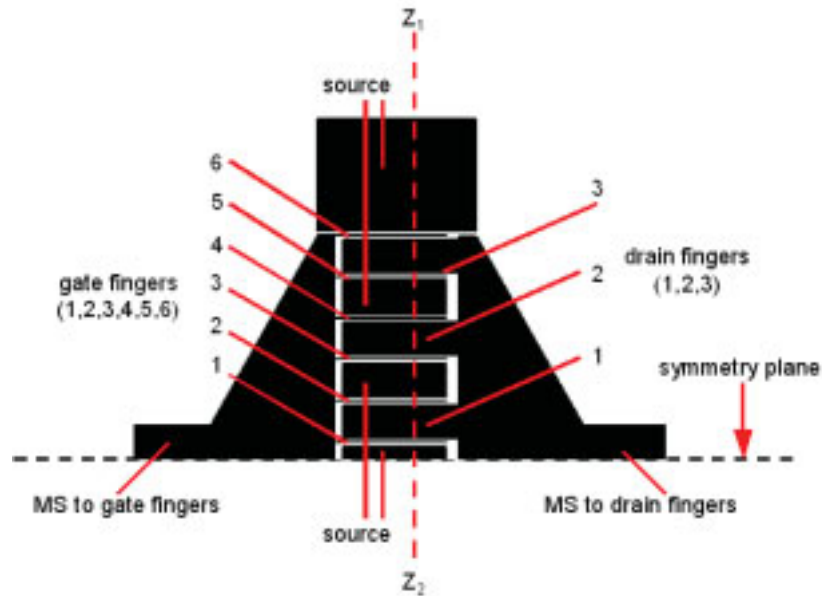
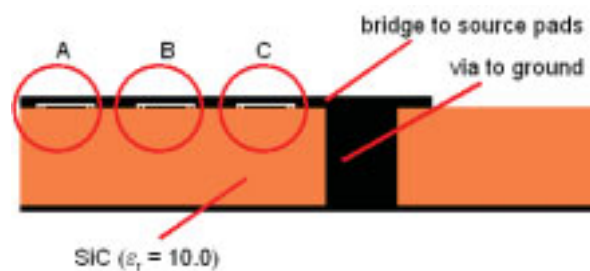
The necessity and use of internal ports are to be described here with the help of a taper shaped high electron mobility transistor (HEMT) structure [52] as given in Fig. 1.2. It is important to know the current distribution at each the gate finger when a couple of transistors are connected in parallel to a common feeding micro-strip line (Fig. 1.2.a). The same is true also for the drain fingers. Because if the current distributions at the gate fingers are not same, i.e. the input currents of the transistors are not identical, their performances are also not same even though identical transistors are used. In order to check these current distributions through 3D EM simulation internal ports have to be placed between the gate and source fingers as well as between the drain and source fingers (Fig. 1.2.b and c) while the micro-strip lines can be excited by waveguide or internal ports. A 3D simulation with all these internal ports provides a Z-matrix. When the output impedances of the gate and drain fingers are known, current distribution through the gate and drain fingers in relation to the input currents at the MS lines can be calculated out of the resulting Z-matrix which is usually done in network simulators. Thus internal ports can be used as interface between EM simulators and network simulators. The details of this HEMT structure as well as the simulation results are presented in Chapter 4.4.

The implementation of internal port in FDFD mesh can be carried out in two ways. In the first one two lumped time varying charges of equal magnitudes but of opposite polarities are inserted at the two nodes of the internal port and in the second one a rectangular shaped current carrying wire is assumed between two metal plates/lines within the structure under consideration. The previous works on the implementation of internal ports/lumped elements in FDTD method are presented in [28-30].

The purpose of the work presented here is to improve the capabilities of the Finite-Difference method in frequency domain (FDFD), when used for structures of complex geometry and with active elements. The main contributions are the derivation of PML parameters and the inclusion of internal port in the FDFD scheme. The parasitic effects of PML as well as internal ports are explored and the ways how to remove them are discussed. A 4-quadrant slot antenna with active circuits is treated as a good example where the use of both the PML walls and internal port is a must. In the following sub-chapters, the FDFD method, anisotropic version of PML boundary condition and internal port are discussed briefly.

The thesis is organized as follows: Chapter 2 describes the PML related convergence problems and how they can be circumvented. Chapter 3 addresses the influence of the PML on the mode spectrum of a waveguide with a PML lateral boundary. The mode spectrum consists of both PML and physical modes corresponding to the eigenvalues of the system matrix. The internal port implementation and the corresponding parasitic effects are given in Chapter 4. Finally, the results are verified for the example of a 4-quadrant slot antenna with integrated electronics. The design issues of the slot antenna are described in Chapter 5 employing the newly developed PML walls as well as internal ports in the F3D simulators.

(a) Top view

(b) : Z_1 - Z_2 cross-section

(c) : A, B, C (zoom) :

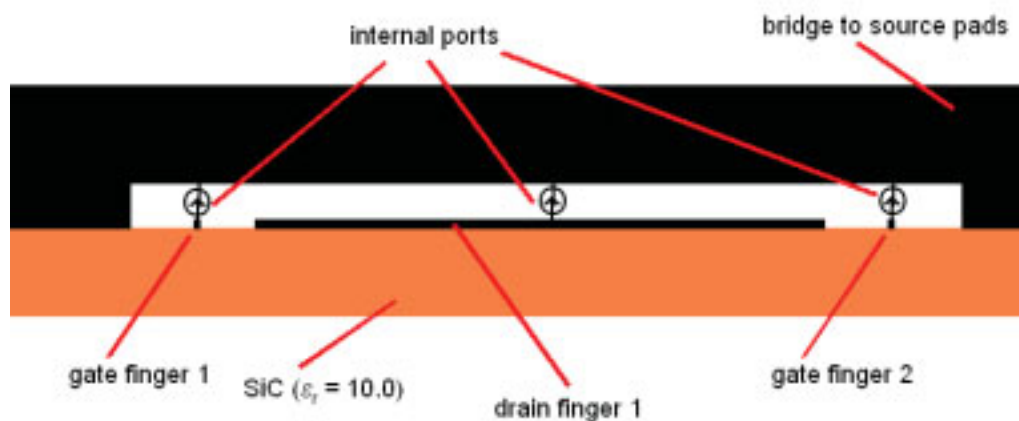


Fig. 1.2 Taper shaped transistor (HEMT) structure [52] (half above the symmetry plane):

- organisation of the gate, drain fingers and source pads together with the micro-strip lines connecting the gate and drain fingers through the tapers.
- cross-sectional view of the structure at Z_1 - Z_2 of (a). The source pads are connected with each other through a bridge and to the ground through a via. The substrate used is SiC ($\epsilon_r = 10.0$).
- the encircled regions of A, B and C are same. The zoomed region of encircled A (or B or C) shows the three internal ports between gate finger and source bridge, and drain finger and the source bridge, respectively.

1.2 Finite Difference Frequency Domain (FDFD) Method

The FDFD method [4, 5] is the frequency domain counterpart of the FDTD [30] method which is based on the discrete approximation of the Maxwell's equations. Unlike the FDTD which deals with an initial value problem, in the FDFD method time terms in the equations are eliminated leaving them complex in nature and a boundary value problem is treated. In its simplest form, the boundary region is a rectangular box as shown in Fig. 1.3. This large box is subdivided into a number of elementary cells by a three-dimensional non-equidistant Cartesian grid according to Yee [1]. Each elementary cell is filled with homogeneous material described by its permittivity and permeability. Hence a change in material properties can only be located on the surfaces of the elementary cells. The electric field components are defined at the centers of the cell edges whereas the magnetic field components are defined at the centers of the cell surfaces. Up to this point, the setting is identical to the common FDTD approach.

In order to describe the EM fields inside the enclosure of the rectangular box, in frequency domain, one has to solve a large system of linear equations instead of applying the leapfrog algorithm [8] in the FDTD method. The solution of the large linear equation system is carried out iteratively. A brief description of the FDFD formulations is given in Appendix 7.1.

The matrix equation is solved by means of an iterative numerical algorithm of Krylov-subspace type [11, 15] in the F3D simulator [10] which is used to carry out all these FDFD investigations in this thesis work. In this procedure the unknowns are updated as long as the values of the unknowns converge to a predefined tolerance. The number of iterations is a measure to the numerical efforts and directly proportional to the CPU time. So the fast convergence is the key issue of the iterative solution in FDFD method.

The FDFD method is particularly advantageous compared to FDTD method to simulate resonating structure like cavities where high possibilities of energy trapping exist.

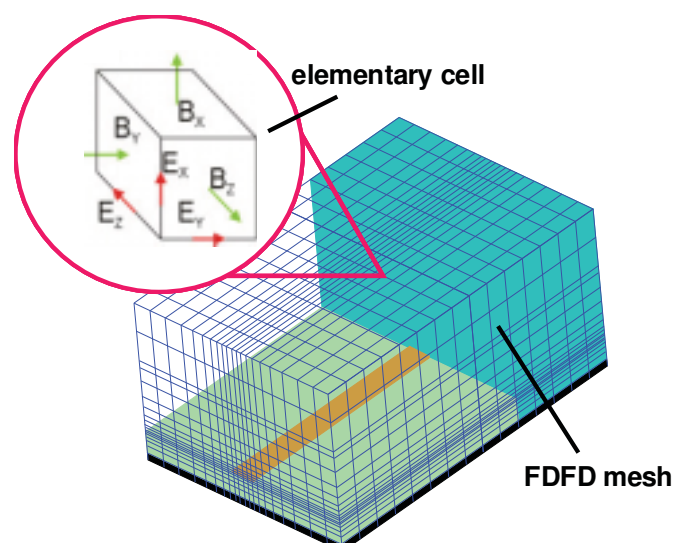


Fig. 1.3 Meshing of the FDFD boundary value problem and description of the elementary cells with the assignments of the field components.

1.3 Anisotropic PML Absorbing Boundary Condition

The PML absorbing boundary condition provides a means of simulating the open boundaries. It has the following tasks during the EM simulations:

1. reducing the size of the finite calculation domain.
2. suppressing the influence of the boundaries on the electrical behaviour of a structure.
3. absorbing radiation from an antenna or parasitic effects like leaky waves over the signal lines and radiation due to the discontinuities, thus allowing to operate structures virtually in open space.

In the F3D EM simulator [10, 12], based on FDFD method, the PML has been implemented according to the anisotropic material approach [18]. In this implementation the PML half space is simply an anisotropic absorbing medium defined by a complex diagonal tensor. The permittivity and permeability of the given arbitrary half space which has the interface with the PML half space are multiplied by the PML tensor to calculate the permittivity and permeability of the PML layers. Fig. 1.4 shows the interface of an arbitrary material and a PML half space.

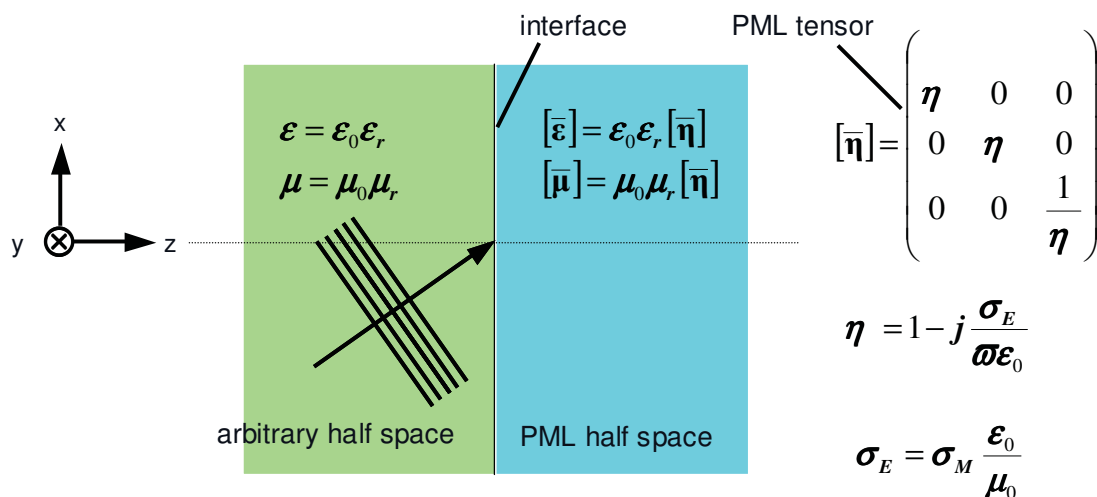


Fig. 1.4 Definition of the PML medium according to the anisotropic material approach. σ_E and σ_M are the artificial electric and magnetic conductivities, respectively, and normalized to ϵ_r . The PML tensor is so chosen thus the attenuation takes place in the z direction.

The PML tensor element of the direction of desired attenuation, in this case the z-direction, is made inverse to the other two elements. Under this arrangement, when waves travel from the simulation region of interest (arbitrary half space) to the anisotropic PML half space, there is no reflection at the interface of the two media while the attenuation takes place in the z-direction. As a consequence, the PML part can be terminated by any boundary wall at $z = \text{constant}$ without affecting the characteristics at $z = 0$.

In the finite difference (FD) mesh the PML half space is usually terminated by electric or magnetic walls and the tensor elements (η) are calculated from an artificial conductivity (σ_E) predefined for a particular PML wall, which is estimated by the residual reflections at the PML

interface. Due to the discretized description of the FD method, the interface of the PML / non PML regions results in spurious reflections [19]. This mismatch problem depends on the difference in conductivities of the neighboring regions and thus can be alleviated by subdividing the PML region into a number of sub layers with varying conductivities, starting with relatively low values at the interface and increasing towards the truncation of the mesh. The nominal reflection coefficient (r_{th}), i.e. the residual reflection at the PML / non PML interface is given by equation 1.1, where d is the thickness of the PML wall in z direction and p is the order of the polynomial variation for the varying conductivities at different PML sub layers. For constant, linear and parabolic variation of the PML conductivities the value of p is 0, 1, and 2, respectively.

$$r_{th} = e^{\frac{-2d\sigma_E\sqrt{\epsilon_r}}{(p+1)\epsilon_0c_0}} \quad (1.1)$$

1.4 Internal Ports

Internal ports are an important feature of any EM simulators. They allow to feed or excite structure from inside the structure as shown in Fig. 1.2 unlike its counterpart of the waveguide ports, which excite a structure with certain mode configuration or spectrum. In general, internal ports can be implemented in two ways: the first one uses a conduction current source and the second one uses relaxation current source. The wave equation of the electrical fields derived from the Maxwell's equations is given by 1.2. ϵ and μ are the permittivity and permeability of the medium. J_e is the conduction current density whereas q_v is the space-charge density. A non-zero value of J_e means the medium contains a conduction current source. On the other hand, a time varying non-zero value of q_v means the medium has a source of non-static surface charges.

$$\nabla E^2 + \omega^2 \epsilon \mu E = j \omega \mu J_e + \frac{1}{\epsilon} \nabla(q_v) \quad (1.2)$$

$$I_0 = \int J_e \cdot dA \quad (1.3)$$

$$Q = \int q_v \cdot dV = -\frac{I_q}{j\omega} \quad (1.4)$$

The conduction current internal port is defined in general as inserting an artificially current I_0 given by equation 1.3 between two certain points (nodes) within two conductors 1 and 2 as shown in Fig. 1.5. Due to the excitation by the current a magnetic field is excited and, depending on the structure, a voltage U is developed between the conductors. This port can be compared with a current source except that in a current source the current does not essentially need a direction while the internal port current must have a direction in order to connect the thin wire between the conductors. The line current comes up with an inductance due to the magnetic fields surrounding the wire and this is to be accounted for if the port influence needs to be eliminated.

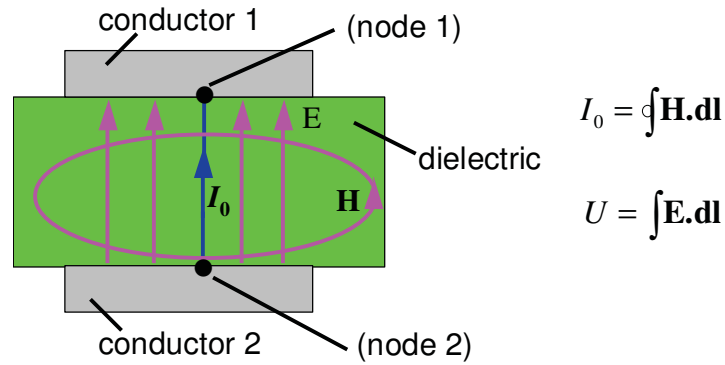


Fig. 1.5 Conduction current internal port : line current source. $q_v = 0$, $J_e \neq 0$.

It is also possible to insert two time varying charges ($-Q_1 = Q_2 = Q$ and Q defined by equation 1.4) of equal magnitudes but of opposite polarities at two nodes as shown in Fig. 1.6. I_q is the input current and related to the time varying charges Q_1 and Q_2 - I_q enters the structure at node 2 and comes out of the structure at node 1. Due to the presence of the charges electric fields develop between the conductors resulting in a potential difference of U . This port utilizes the relaxation current between the conductors and can be thought of a voltage source providing charges of equal but opposite sign at the two nodes. Another point is that this port does not need a direction which is different to the line current source.

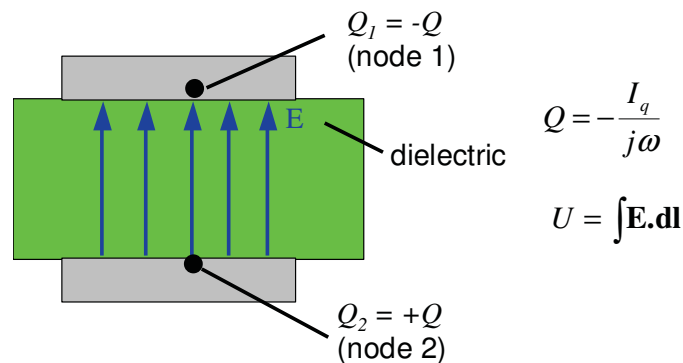


Fig. 1.6 Relaxation current internal port : voltage source. $q_v \neq 0$, $J_e = 0$.

The FDFD method solves the discretized version of the wave equation 1.2. The conduction current internal port is included in FDFD by defining a path between two conductors and then introducing a line current source (I_0) at the edges of the cells along the path. Within the FD approximation, it can be assumed that the line current I_0 is homogeneously distributed along the cross section (of the dual cells [8]) of the path – so it has a rectangular cross-sectional area. See Appendix 7.3 for the FDFD formulation of this procedure.

On the other hand, according to [8], the implementation of the relaxation current internal port in the FDFD scheme (see Appendix 7.2) by inserting the time varying charges at the centers of the dual cells (defining the nodes of Fig. 1.8 at the centers of the dual cells) is not feasible due to the evolving non physical solutions.

2 PML Parameters and Convergence

2.1 Motivation and General Considerations

According to the FDFD method the analytical wave equation of electromagnetic (EM) fields, given by 2.1, is transformed to a discretized form of wave equation following the incorporation of grad div term [6] and symmetrical formulation [7], given by 2.2, that describes the EM fields inside the enclosure of a rectangular box containing the structure under consideration and thereby defining a boundary value problem (see Appendix 7.1). In this matrix form of the discretized wave equation, \vec{e} is a vector that contains the electric field components for all mesh cells. The system matrix M contains all the information about the material properties, dimensions and frequency. \vec{b} represents in general the source for the excitation through waveguide ports or internal ports. In case of the waveguide ports, \vec{b} corresponds to the sum over all transversal electric fields of the available modes at the waveguide ports.

$$\nabla \times \nabla \times \vec{E} - k_0^2 \vec{E} = \mathbf{0} \quad (2.1)$$

$$M \vec{e} = \vec{b} \quad (2.2)$$

It is worth to look into the construction of the matrix wave equation closely. The F3D solver based on the FDFD method is developed according to a Cartesian coordinate system where all the information of the materials, dimensions etc. as well as fields and sources are assigned to the matrix and vector elements, respectively, cell by cell, first of all in the x direction, then in the y direction and lastly in the z direction as given by the equation of 2.3. M_{ij} 's ($i, j = x, y, z$) are the sub matrices with dimension of $n \times n$, where n is the size of the mesh, and \vec{e}_i 's as well as \vec{b}_i 's are the vectors with dimension n . A more comprehensive representation of 2.3 is given by 2.4 where $a_{i,j}$'s are the elements of matrix M consisting of material and dimensional information, e_i and b_i ($i = 1 \dots 3n$) represent the field and source components corresponding to the vectors \vec{e} and \vec{b} , respectively. It should be noted that M is symmetric but not positive definite and consists only of very few diagonals with nonzero elements.

$$\begin{bmatrix} M_{xx} & M_{xy} & M_{xz} \\ M_{yx} & M_{yy} & M_{yz} \\ M_{zx} & M_{zy} & M_{zz} \end{bmatrix} \cdot \begin{bmatrix} \vec{e}_x \\ \vec{e}_y \\ \vec{e}_z \end{bmatrix} = \begin{bmatrix} \vec{b}_x \\ \vec{b}_y \\ \vec{b}_z \end{bmatrix} \quad (2.3)$$

$$\begin{bmatrix} a_{1,1} & \dots & \dots & a_{1,3n} \\ \dots & \dots & a_{i,j} & \dots \\ \dots & \dots & \dots & \dots \\ a_{3n,1} & \dots & \dots & a_{3n,3n} \end{bmatrix} \cdot \begin{bmatrix} \dots \\ e_i \\ \dots \\ e_{3n} \end{bmatrix} = \begin{bmatrix} \dots \\ b_i \\ \dots \\ b_{3n} \end{bmatrix} \quad (2.4)$$

The matrix equation of 2.4 is solved for the unknowns of e_i with an iterative numerical algorithm, namely a Krylov-subspace method [10, 15] with the Independent Set Ordering and SSOR-preconditioning procedure (see the Appendix 7.7). In this procedure the values of the unknowns are updated as long as the unknowns converge to a predefined tolerance.

As the anisotropic PML satisfies Maxwell's equations, the PML cells become part of the bounded region automatically during the discretization. The influence of these anisotropic PML cells on the convergence of the iterative solution can be explained with the help of the Gerschgorin circles [45]. The union of the Gerschgorin circles of radius r_i contains all the eigenvalues of the system matrix M , where the radius r_i is calculated as the summation of the magnitudes of all the non-diagonal elements of the i^{th} row in M given by 2.5. A quantity ρ_i is defined as the ratio between the summation of the magnitudes of all the non-diagonal elements and the diagonal element at the i^{th} row in M according to equation 2.6. Again ρ_{\max} is the maximum value of ρ_i considering all the rows of the system matrix M given by the equation 2.7. Some examples of Gerschgorin circles are shown in Fig. 2.1.

$$r_i = \sum_{\substack{j=1 \\ j \neq i}}^{3n} |a_{i,j}| \quad (2.5)$$

$$\rho_i = \frac{r_i}{|a_{i,i}|} \quad (2.6)$$

$$\rho_{\max} = \max_{1 < i < 3n} \{ \rho_i \} \quad (2.7)$$

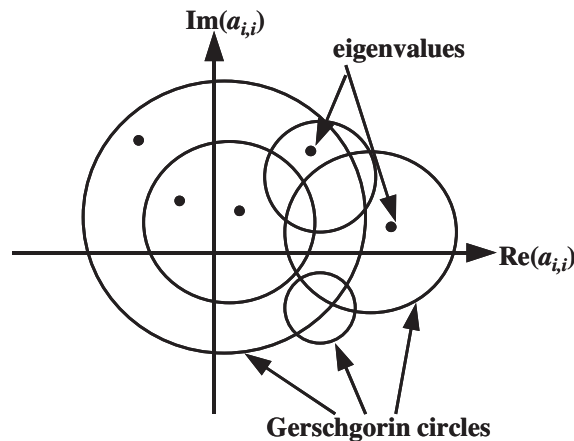


Fig. 2.1 Gerschgorin circles with centers at $(\text{Im}(a_{i,i}), \text{Re}(a_{i,i}))$.

For M to be a positive definite matrix, ρ_i must be smaller than one, all the eigenvalues must lie within the right hand side of the imaginary axis in order to make the iterative solution provide a stable convergence. But in the case of FDFD method, M is usually not a positive

definite matrix, i.e. the periphery of the circles with some of the eigenvalues extends to the left hand side of the imaginary axis which may lead to a bad convergence.

In order to describe the importance and consequences of the parameters of r_i , a_{ii} and ρ_i for the numerical convergence of the FDFD method with PML the patch antenna[19] in Fig. 2.6.a is examined. It is assumed that the antenna has only one PML (X-PML) boundary followed by a magnetic wall in the direction perpendicular to the patch. Other open boundaries are terminated by magnetic walls. Under these conditions the antenna is simulated at 16 GHz and the parameters r_i , a_{ii} and ρ_i are calculated out of the system matrix at each row. The same is done for the case with the PML medium replaced by air while keeping the discretization scheme the same, this is termed as the case without PML (no PML). The ratios between the cases of with PML and without PML for all these three parameters are calculated. In each case the ratios which are equal to one, corresponding to the inner mesh cells and rows of the system matrix not affected by the PML medium, are excluded. The remaining ratios are sampled linearly (counted in stepped ranges) and drawn in Fig. 2.2.

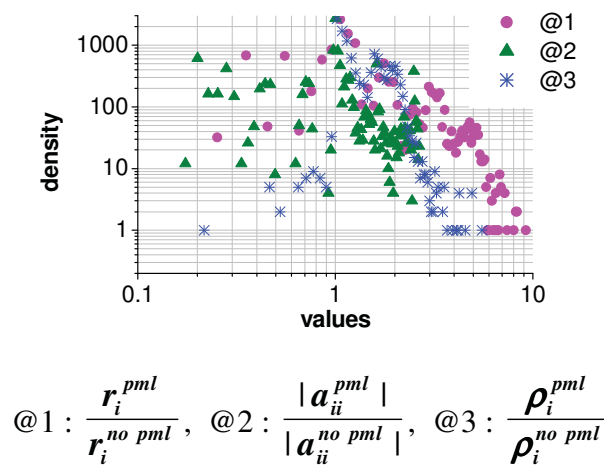


Fig. 2.2 Densities of the values given by the ratios of @1, @2 and @3. The total number of rows in M is 75816 ($=3 \times 27 \times 36 \times 26$) and the number of the PML affected rows where the ratios given by @1, @2 and @3 are not equal to one is 12273.

Looking at Fig. 2.2, it is evident that introducing the PML results in an increased number of rows in M where the values of the ratios defined by @1, @2 and @3 are larger than 1.0. In addition, the values of @1 are larger than those of @2. This helps to state that the addition of the PML wall increases the values of ρ_i and correspondingly ρ_{max} , which means that the radii of the Gerschgorin circles become larger and the possibility of the real parts of the eigenvalues to be more negative increases. The outcome is that the condition number grows larger and the convergence of the iterative process is more unstable when the PML wall is included. In this way the inclusion of the PML wall results in a change in the numerical properties of the system matrix and thereby affects the convergence of the solver, i.e., the number of iterations. The number of iterations is taken here as a measure for the numerical efforts and it is directly proportional to the CPU time needed to obtain the solution.

When discussing the numerical consequences of introducing the PML, it is important to have a close look on the resulting permittivity and permeability tensors, which are written here as the products of the isotropic physical material constants and a tensor $[\boldsymbol{\eta}]$ representing the PML properties according to [3, 4] (see equations (2.8) and (2.9)). $[\boldsymbol{\eta}]$ is a diagonal tensor with the complex parameter η_i , the imaginary part of which defines the attenuation and thus the residual reflections at the PML (see Fig. 2.3). The nominal reflection coefficient (r_{th}) of equation 1.1 can be written in terms of the imaginary part of η_i ($\text{Im}(\eta_i)$) as 2.10. As attenuation and reflection are inversely proportional, attenuation (α_{th}) can be written as 2.11. For low reflection, i.e., high attenuation in the PML, the product of $|\text{Im}(\eta_i)|$ and d must be large. On the other hand, $|\text{Im}(\eta_i)|$ should not be too large, as the matrix condition depends on $\text{Im}(\eta_i)$. So for higher attenuation as well as better matrix condition a relatively small $|\text{Im}(\eta_i)|$ and large d should be chosen. When using PML walls for several outer boundaries, these walls overlap at edges and corners as illustrated in Fig. 2.3. In case of the overlapping at the edges (e.g. overlapping 1 & 2) and corners (overlapping 1, 2 & 3) the resulting PML tensor is the product of the PML tensors of the individual PML walls that form the edges and corners, respectively.

$$[\boldsymbol{\varepsilon}] = \varepsilon_0 \varepsilon_r [\boldsymbol{\eta}] \quad (2.8)$$

$$[\boldsymbol{\mu}] = \mu_0 \mu_r [\boldsymbol{\eta}] \quad (2.9)$$

$$r_{th} = \exp\left(\frac{-2\sqrt{\varepsilon_r} \omega |\text{Im}(\eta_i)| d}{(p+1)c_0}\right) \quad (2.10)$$

$$\alpha_{th} \propto \omega \cdot |\text{Im}(\eta_i)| \cdot d \quad (2.11)$$

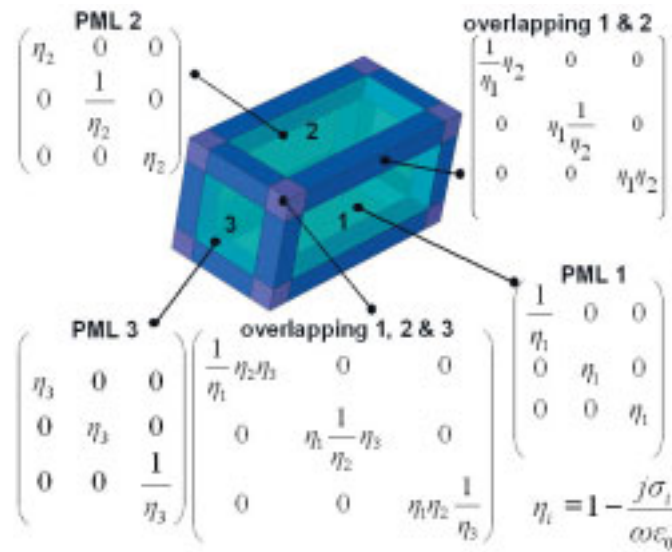


Fig. 2.3 PML Tensors $[\boldsymbol{\eta}]$ (see equations (2.8) and (2.9)) for PML walls in three directions detailing the overlapping regions. σ_i denotes the artificial conductivities (electrical) of the respective PML wall as derived from a given nominal reflection factor (equation 1.1).

The inspection of the tensors according to Fig. 2.3 reveals that, because always both η_i and its inverse appear, the PML increases the magnitude range of the material tensors and thus that of the resulting entries in the system matrix, which in turn increases the radii of the Gerschgorin circles as mentioned above. As these circles contain all the eigenvalues of the system matrix, larger radii of those circles means higher possibilities of the real parts of the eigenvalues to assume smaller values and thereby worse convergence. This situation becomes particularly critical for the overlapping regions since there several factors of the η_i are multiplied. In order to demonstrate this, Tab. 2.1 shows typical values for the PML tensor elements (based on an example at 1GHz with -60dB nominal reflection). This is the basic effect why PML causes the numerical properties to deteriorate but one needs an in-depth investigation to better understand the underlying effects and to find the solutions minimizing the odds. This is presented in the following sections.

$ \eta_1 $	$ 1/\eta_1 $	$ \eta_2 $	$ 1/\eta_2 $	$ (1/\eta_1)\eta_2 $	$ \eta_1\eta_2 $	$ (1/\eta_1)\eta_2\eta_3 $	$ \eta_1(1/\eta_2)\eta_3 $
83.0	0.012	75.0	0.013	0.9	6225	67.5	83

Tab. 2.1 Diagonal elements of PML tensors according to Fig. 2.3 (ϵ_r of PML wall 1 and 2 are 1.0 and 2.2 respectively; σ_i of PML wall 1 and 2 are 4.6 and 4.2 respectively; μ_r is 1.0 in all cases; for calculation of σ_i see [18, 19]).

Having known that PML in general worsens the convergence of the iterative solution it is investigated quantitatively which parameters of the PML wall affect the convergence mostly and how that can be tempered by modifying the PML regions and parameters. The most vital modifications and parameters will be discussed separately following some general considerations regarding convergence as given below:

1. As already mentioned in chapter 1, the interface of the PML/non PML regions in the discretized description of FDFD method results in spurious reflections. This mismatch problem can be alleviated by subdividing the PML region into a number of layers with varying conductivity [19]. In this point it is important to know the impact of the number of PML layers on the convergence. More layers improve of course the accuracy but increase the numerical expenses. It is found that a 5-layer configuration provides a good compromise and this number is used in all the following investigations.
2. The convergence of the iterative solver is influenced also by the choice of the PML backing. Commonly, PML walls are followed by electric or magnetic walls. We found that for the structures considered in this work, electric walls lead to a less number of iterations than magnetic walls.
3. Adjacent PML and non-PML cells should have sizes of comparable dimensions to have the results less erroneous and iterations reduced in number.
4. The number of iterations increases with the increase in $|\epsilon_{\max} - \epsilon_{\min}|$ and frequency, where ϵ_{\max} and ϵ_{\min} are largest and smallest relative dielectric constants within the structure. These are general characteristics of the FDFD simulation, independently whether PML is included or not.

2.2 Overlapping PML Walls

While for a single PML wall the tensor elements are in the range $1/\eta \dots \eta$, this becomes worse if overlapping regions of two PML walls are included. Assuming that both PML walls have the same properties, the tensor elements within the structure now cover the range $1/\eta \dots 1 \dots \eta^2$. Proceeding with 3 overlapping PML regions the overall situation does not change from this point of view because the additional elements are of same order (if one assumes identical PML properties). To give numbers, Tab. 2.1 shows that for a single PML wall (e.g. PML wall 1) the range of tensor elements is (0.012 - 83.0) and when the PML wall 2 is included the range of matrix elements extends to (0.012 .. 6225.0).

Going beyond these relatively simple arguments, extensive investigations were performed simulating typical microwave structures with different PML configurations. It is found that the PML disposition indeed has a drastic influence on the efforts required for solving the system of equations. Introducing a single PML wall already leads to a significant increase in the number of iterations of the solver (typically a factor of 2). Including overlapping regions with 2 PML results in further drastic deteriorations (an additional factor >15), which in many cases render this approach useless for practical design work. Adding more PML walls with overlapping regions, convergence deteriorates further.

It is found that this deterioration of convergence can be alleviated by modifying the PML definition in the edge and corner regions. Different ideas have been tested including an angle-dependent description and the insertion of additional physical conductivities in the PML formulation for numerical stabilization. All these approaches did not yield the desired improvements. The best solution turned out is to avoid any overlapping. Avoiding the overlapping PMLs is carried out by disjoint PMLs (called non-overlapping PML) where the edges and corners are replaced by the complete PML walls. Since the edges and corners form only a very small fraction of the overall PML surface, the reflections occurring there remain negligible in most cases and one can use a PML with attenuation in a single direction instead. Fig. 2.4 illustrates this idea of non-overlapping PML for the edge case. When PML 1 overrides PML wall 2, it is referred to as “12” orientation in the following and vice versa.

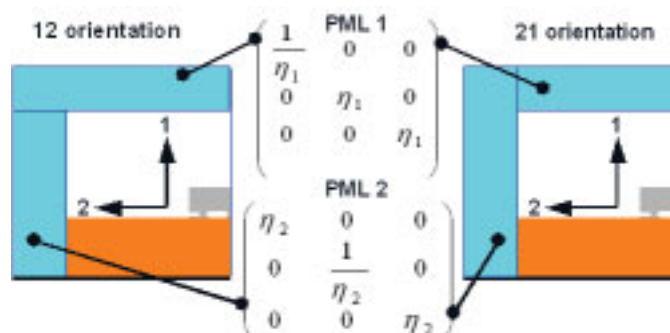


Fig. 2.4 Edge of the structure according to Fig. 2.3 with non-overlapping (disjoint) PML walls illustrating 2 possibilities of edge description.

This approach to circumvent the problem with overlapping PMLs proves its effectiveness for various structures like patch antenna, microstrip, flip-chip or LTCC structures. The

investigations of how the inclusion of PML (overlapping) and non-overlapping PML influences the matrix elements, and thereby the convergence of the iterative solution will be presented in the following dealing a micro-strip line and a patch antenna.

The micro-strip structure of Fig. 2.5.a is simulated at 20 GHz first of all without any PML wall. In order to keep the mesh the same for all the simulations, the PML walls are not just excluded from the structure, rather the tensor elements of the PML walls are made unity ($\eta = 1.0$) in order to represent the case without PML. In this case the PML cells are there but not filled with PML material. The density distribution of the non-zero matrix elements as a function of magnitudes is shown in Fig. 2.5.b.

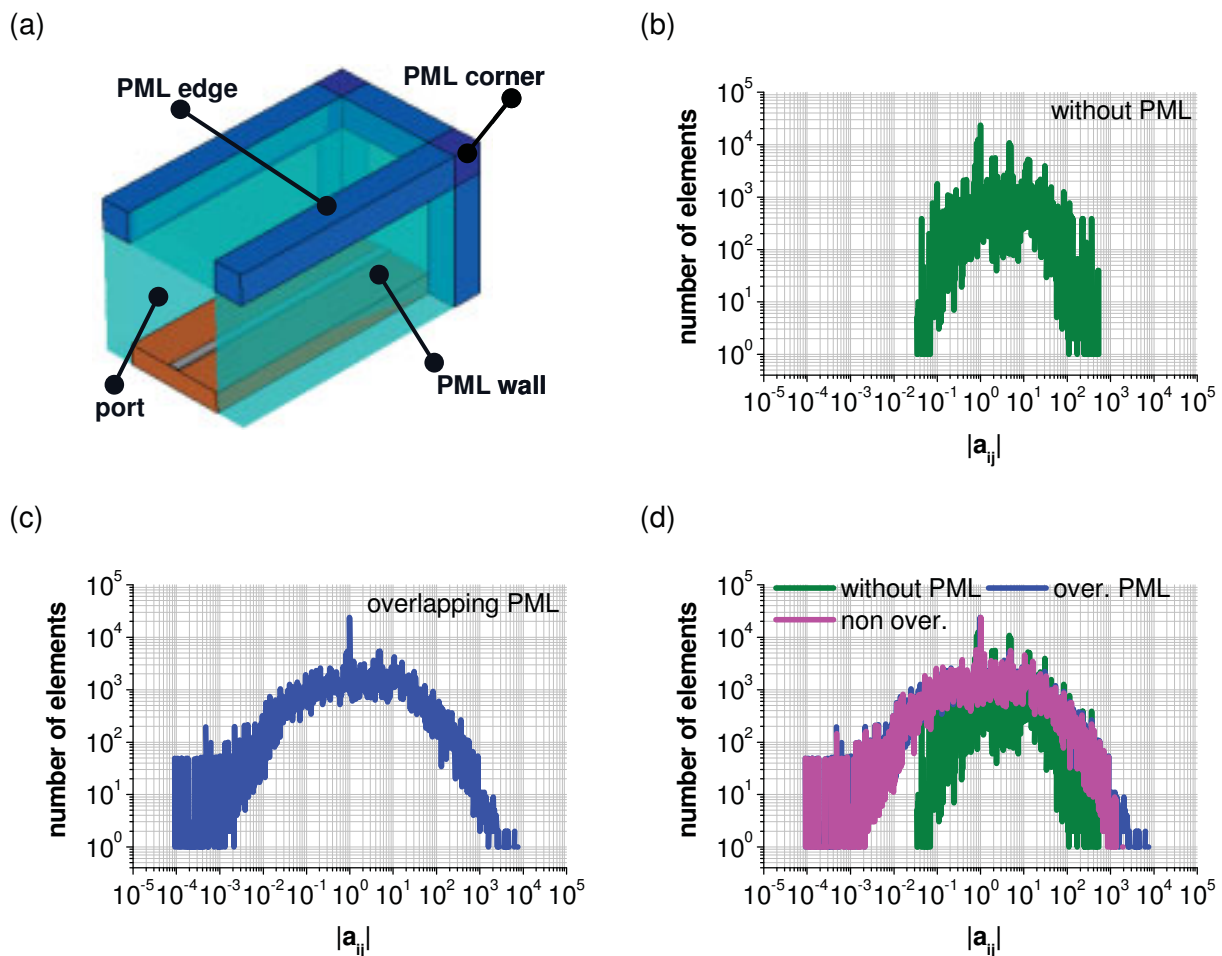


Fig. 2.5 a) The micro-strip (MS) surrounded by PML walls on all sides other than the port. The MS is $10 \mu\text{m}$ thick and $50 \mu\text{m}$ wide. The substrate ($\epsilon_r = 9.8$) is $100 \mu\text{m}$ thick. The PML walls consisting of 5 layers with variable thicknesses have an overall reflection error of -70dB and parabolic spatial variation of the conductivities.

The density of the matrix elements a_{ij} in relation to their magnitudes for the case without PML walls (b), with PML walls including the overlapping regions (c) and with non-overlapping PML walls (d). In (d) graphs in (b) and (c) are redrawn for comparison. The lowest and largest values of the magnitudes are in (b) $1.74\text{E}-02$ and 845.62 , in (c) $7.54\text{E}-05$ and 7584.38 , and, in (d) $7.4\text{E}-05$ and 1994.16 respectively.

In the same way, the MS structure is simulated with all the PML walls including the overlapping regions of the corners and edges at 20 GHz. The density of the magnitudes of the non-zero matrix elements is presented in Fig. 2.5.c. The structure is simulated also with non-overlapping PML walls and again the density of the magnitudes of the non-zero matrix elements are plotted together with those of the cases without PML and overlapping PML walls in Fig. 2.5.d.

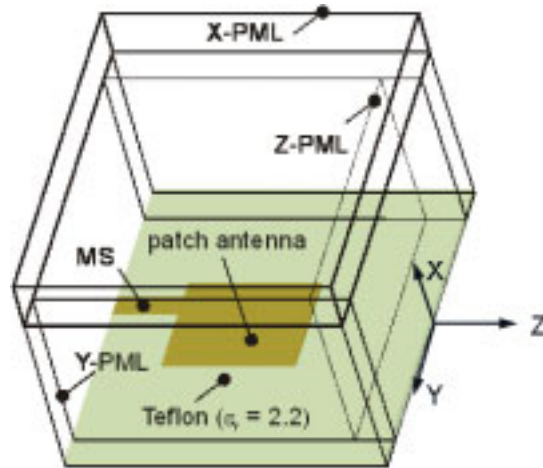
From Fig.s 2.5.b and 2.5.c it is clear that the PML in general widens the range of magnitudes of the matrix elements. The very small and large matrix elements, few in number but very diverse from each other, are due to the overlapping PML regions (recall the range: $1/\eta \dots 1 \dots \eta^2$) and result in a worse condition of the system matrix. In order to improve the condition of the matrix, we must check which of the largest and lowest values we can exclude that do not have significant influence on the reflection level. Fig. 2.5.d shows that the upper limit of the range of magnitudes arising due to the overlapping regions can be reduced by using the non-overlapping PML. That is why non-overlapping PML walls provide better condition of the system matrix and also lower number of iterations.

The above-mentioned results obtained in the case of the MS line are also true for the patch antenna structure of Fig. 2.6.a. We shall see further with this patch antenna example how overlapping and non-overlapping PML influence the Gerschgorin circles and eventually the number of iterations. In the picture we see the arrangement of the PML walls in non-overlapping case, which is formed by replacing the overlapping corners and edges. In the x direction the PML is completely x directed (X-PML). The yz columns below the x directed PML have been made y directed (Y-PML) and the z directed PML (Z-PML) is surrounded by the x and y directed PML walls. This is termed as xyz orientation of PML walls.

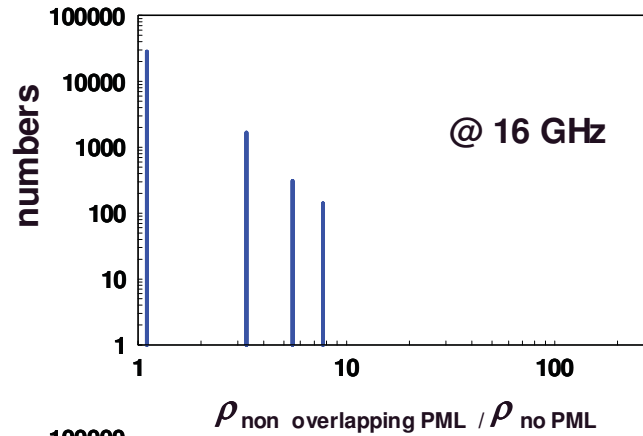
In order to compare the non-overlapping PML against the overlapping one, the antenna was simulated with all the PML walls including all the overlapping regions. The outcome was useless, as the PML fully including all the overlapping descriptions results in an iteration count above 300,000 already at 3 GHz and still without any convergence. So the overlapping regions were checked one by one. Since the outcome was the same in all these cases, only the overlapping region formed by the X-PML and Z-PML will be described in the following. Magnetic walls are used instead of PML walls in the y directions.

Now the antenna is simulated without any PML as well as with overlapping and non-overlapping PML walls in x and z directions. Then the ρ_i 's for each row of the system matrix M in all these three cases are calculated at 16 GHz. Clearly a significant number of ρ_i 's are same for all those three cases, namely for the cells corresponding to the non-PML regions. So these ρ_i 's are excluded. The rest of the ρ_i 's which are affected by PML walls are drawn as a ratio with respect to the no-PML case, separately for the non-overlapping and overlapping cases in Fig. 2.6.b and c, respectively. As one can see, for the non-overlapping case we have already a moderate number of rows in M , where the ρ_i 's are larger than in the no PML case. Now the inclusion of overlapping PML wall in the xz edge extends the number and values of the ρ_i 's extremely as evident in the lower chart. This means that for this high number of rows, the radii of Gerschgorin circles become larger extending the peripheries in the left side of the imaginary axis, which first results obviously in real part of eigenvalues to be more negative and thereby in bad convergence. The same is true also for other frequencies.

(a)



(b)



(c)

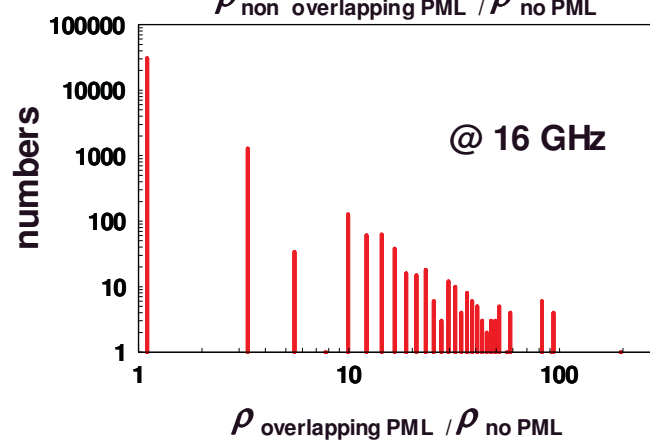


Fig. 2.6 (a) : The patch antenna[19] surrounded by PML walls on X and Z (Y-PML replaced by magnetic wall). The PML walls consist of 5 layers with variable thicknesses and have an overall reflection error of -70dB and a parabolic spatial variation of the conductivities. The density of PML affected ρ_i are shown for case of non-overlapping PML (b) and overlapping PML (c), respectively, in relation with the case without PML.

Since the overlapping regions of corners and edges form a very small fraction of the whole PML surface, the reflection occurring there if non-overlapping PML walls are used can be expected to be negligible. For example, we can see in Fig. 2.7.a that there is no significant change in the resulting S-parameters due to the simplifications. But we have very significant improvement in the convergence of the iterative solution when non-overlapping PML walls are used. For non-overlapping walls the number of iterations remains below 2000 up to 16 GHz whereas for overlapping PML case, the number rises from 7000 to above 220,000 (Fig. 2.7.b).

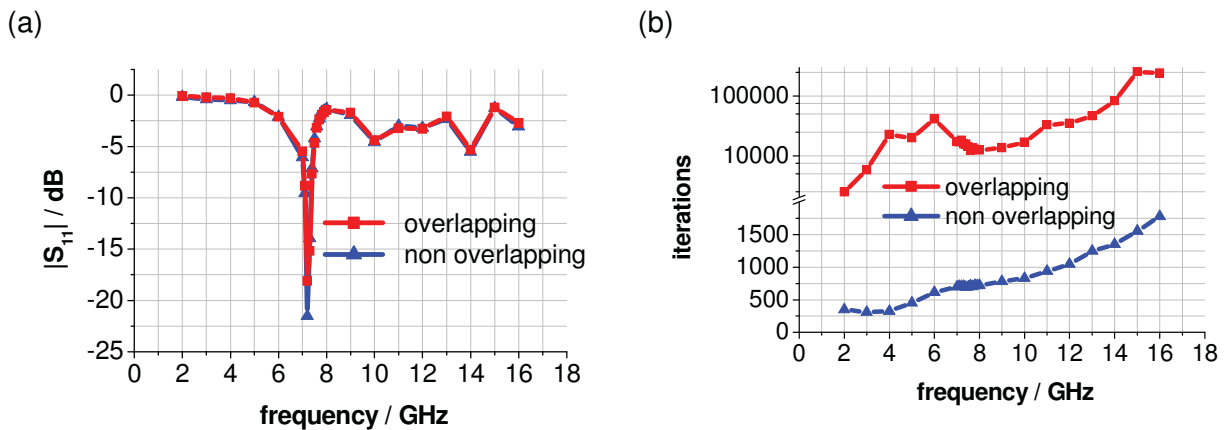


Fig. 2.7 (a) : Reflection coefficients of the antenna using overlapping and non-overlapping PML walls. (b) : The number of iteration for the simulation of the antenna using overlapping and non-overlapping PML walls. In both cases only X- and Z-PML walls are used.

One should note that the choice of PML direction in the edge and corner regions termed as orientation in Fig. 2.4 affects the convergence as well. One of the reasons is the construction of the system matrix where the order of elements influences the number of iterations – this is solely due to the characteristic of the solver, and has nothing to do with PML in general.

In order to see the influence of the orientation of the structure as well as the PML walls, we have to look into the construction of the matrix equations (2.3 and 2.4) closely. As mentioned above, our FDFD method is developed according to a Cartesian coordinate system where all the information of materials, dimensions etc as well as fields and sources are assigned cell by cell first of all in the x direction, then in the y direction and lastly in the z direction. So the construction of the matrix equation is totally different for different orientations of the structure and in the same way those of the PML walls.

Let us consider two examples of Fig. 2.8. In the first case, one half of a patch antenna (top) is calculated with the direction of radiation in the z direction. Two non-overlapping PML walls in the z and x directions are used. Here we see that there is a large difference in the number of iterations for different orientations of xz and zx non-overlapping PML walls. By choosing zx PML the number of iterations is reduced by 25%.

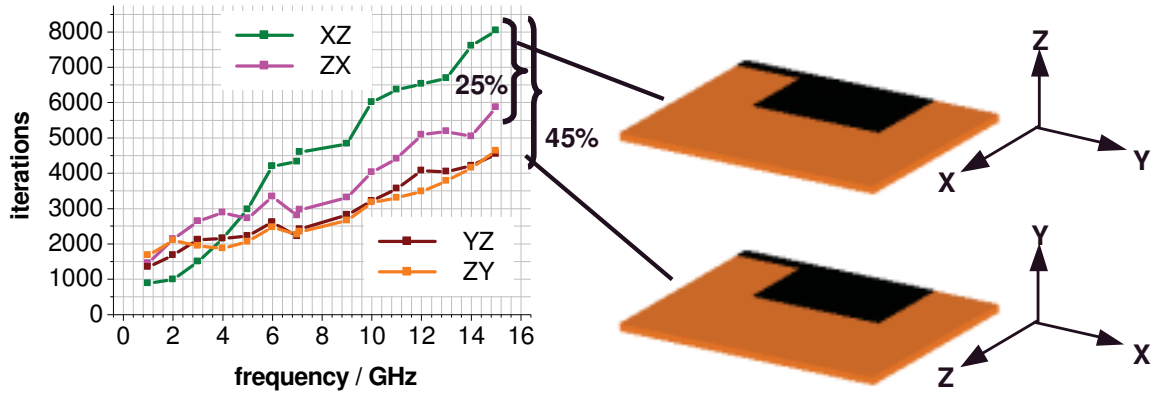


Fig. 2.8 Iterations for different orientation and rotation with respect to the Cartesian co-ordinate system of a half patch antenna. The substrate of the antenna is Teflon ($\epsilon_r = 2.2$). The dimension of the patch is $8000 \mu\text{m} \times 50 \mu\text{m} \times 16000 \mu\text{m}$ and that of the feeding microstrip is $1226 \mu\text{m} \times 50 \mu\text{m} \times 8000 \mu\text{m}$

Now the antenna is rotated as given by (bottom), where the radiation takes place in the y direction and two PML walls are used in the y and z directions. Here we can see that with this orientation the number of iteration is reduced by 45% even though there is no significant change in the number of iterations for yz and zy orientations. However the dependence of convergence on the orientation of a structure in the x, y or z directions can be tempered by improving the solver inputting procedure – rearranging the matrix elements.

2.3 PML Cell Size

The cell size within the PML layers turned out to be a vital quantity, which greatly affects the numerical convergence. From equation 2.11 it is clear that thickness of the PML wall (d) has a dominant rule over the attenuation. For a constant attenuation, an increase in d means a decrease in $\text{Im}(\eta_i)$ and thereby an improvement in numerical convergence. Extensive investigations were carried out in order to check the influence of PML cell size on both the accuracy and numerical convergence with the help of different structures with single PML walls (only one PML wall in one direction) and multiple PML walls (more than one PML wall in different directions and non-overlapping). The structures investigated include MS, CPW, flip-chip, spiral inductor, coupler, antenna etc. The most important results will be presented in the following sub-chapters.

A simple MS structure with a single PML at the end will be investigated in detail with different lateral and longitudinal discretization schemes to check the absorbing capability of the PML as well as the impact of its thickness (cell sizes) on convergence. In this case the PML wall works as a matched layer. The dependency of the convergence on ρ_{max} will be explained.

PML walls are used mostly to absorb radiation. Therefore, a radiating antenna structure will be studied to optimize the PML cell sizes. Multiple PML walls are used and they are assumed to be non-overlapping at the corners and edges. Eventually the slot antenna of Fig. 5.2 will be examined as an example of practical interest.

2.3.1 Single PML Wall : Micro-strip Structure

The micro-strip structure in Fig. 2.9 is investigated for different lateral and longitudinal discretization schemes in order to optimize the PML cell size with regard to convergence. Two different lateral discretization schemes are used as given in Fig. 2.10, where in the upper picture (a) the smallest and largest cell sizes in the x direction are of 3 and 184 μm respectively, in the y direction of 6 and 160 μm , respectively. On the other hand, in the lower picture (b) the smallest cell sizes are same as the upper ones but the largest cell sizes in the x and y directions are reduced to 40 μm . In both cases the dimension of the xy cross-section is identical, only the size and number of cells are varied.

Along with these two lateral discretization schemes, the cell sizes in the longitudinal z-direction both in the PML and non-PML regions are varied arbitrarily in order to find out the PML cell sizes in comparison to the non-PML cell sizes for which the number of iterations reduces to a minimum. In all cases, PML is chosen such that reflection at the end of the MS line must approach to the nominal reflection (r_{th}) of the PML wall. Three longitudinal discretization schemes are shown in Fig. 2.11, where the length and the number of cells are kept constant in each case. In version a1 the smallest cells are the PML cells, in a2 the structure is homogeneous and in a3 the largest cells are the PML cells. Simulations are carried out considering each combination of the lateral and longitudinal discretization schemes of Fig. 2.10 and 2.11 respectively. The resulting reflection coefficients and the number of iterations are plotted in Figs. 2.12 and 2.13 respectively.

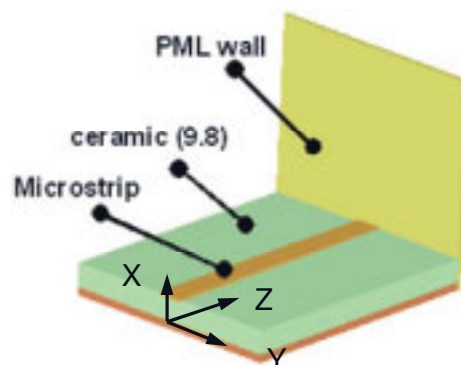


Fig. 2.9 The micro-strip structure with a PML wall at the end. The strip is 10 μm thick and 50 μm wide. The substrate is 100 μm thick and the dielectric constant of the substrate is 9.8. The PML wall consisting of 5 layers with variable thicknesses has an overall reflection error of -60 dB and parabolic spatial variation of the conductivities.

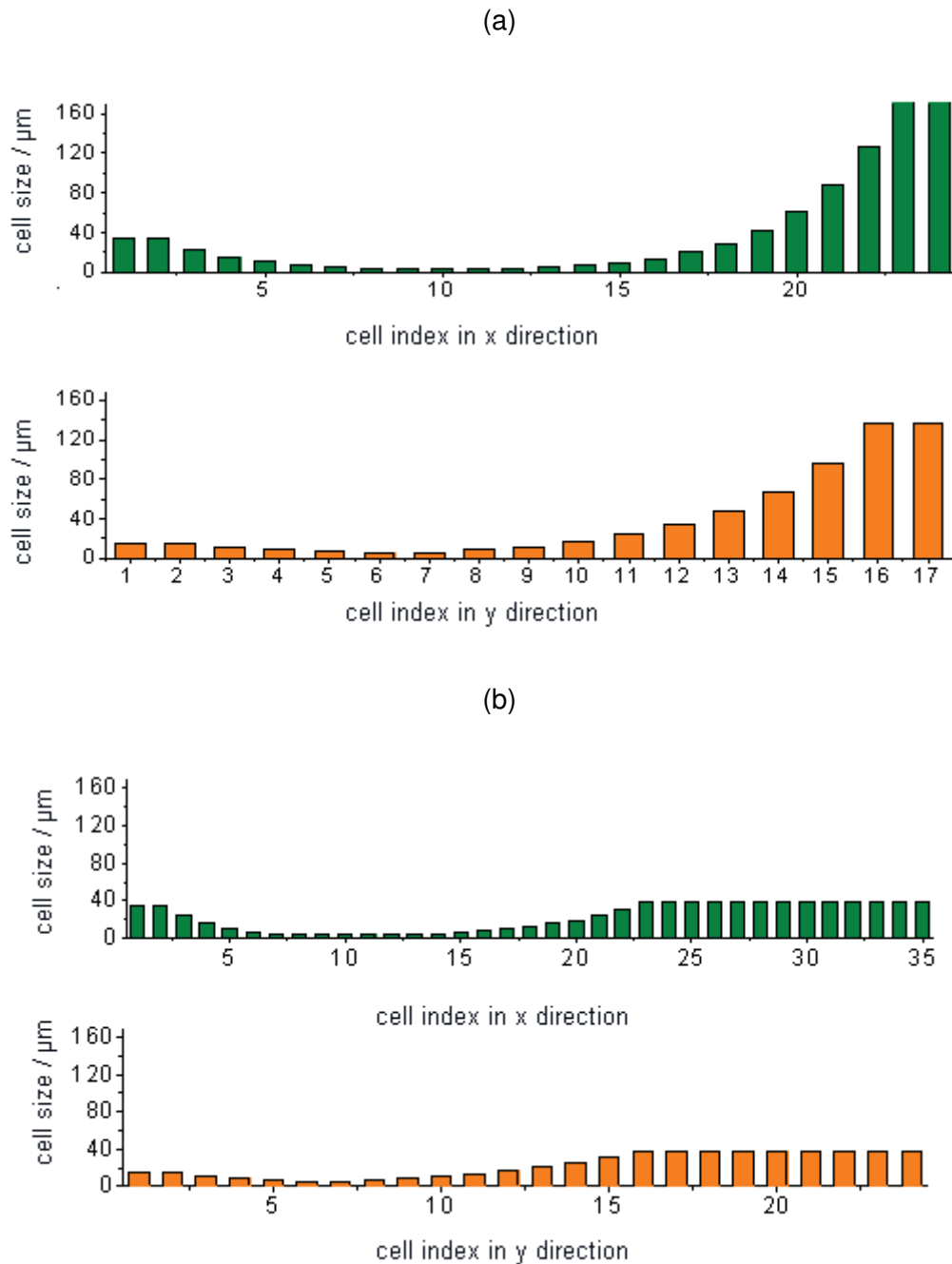


Fig. 2.10 Discretization schemes in the xy plane of the MS structure given in Fig. 2.9. The number of cells in the x and y directions are 24 and 17, respectively, in (a), and 35 and 24, respectively, in (b).

From Fig. 2.12 it is clear that the reflection coefficients in both the cases of different lateral discretizations remain the same, where the homogeneous discretization provides the lowest reflection error. As the nominal reflection is taken as -60dB , ideally the structure should provide a reflection of -60 dB , for the whole frequency range. We see that at the lower frequency range (up to 10 GHz) the reflection levels in all cases stay constant at -62 dB . The reflection coefficients are below -45 dB up to 200 GHz. The minima's in the $|S_{11}|$'s are due to the canceling of each other of the reflected waves at the PML layer interfaces. On the other hand, larger reflection ($> -60\text{ dB}$) in the higher frequency range is due to the non-quasy static behaviour of the fields.

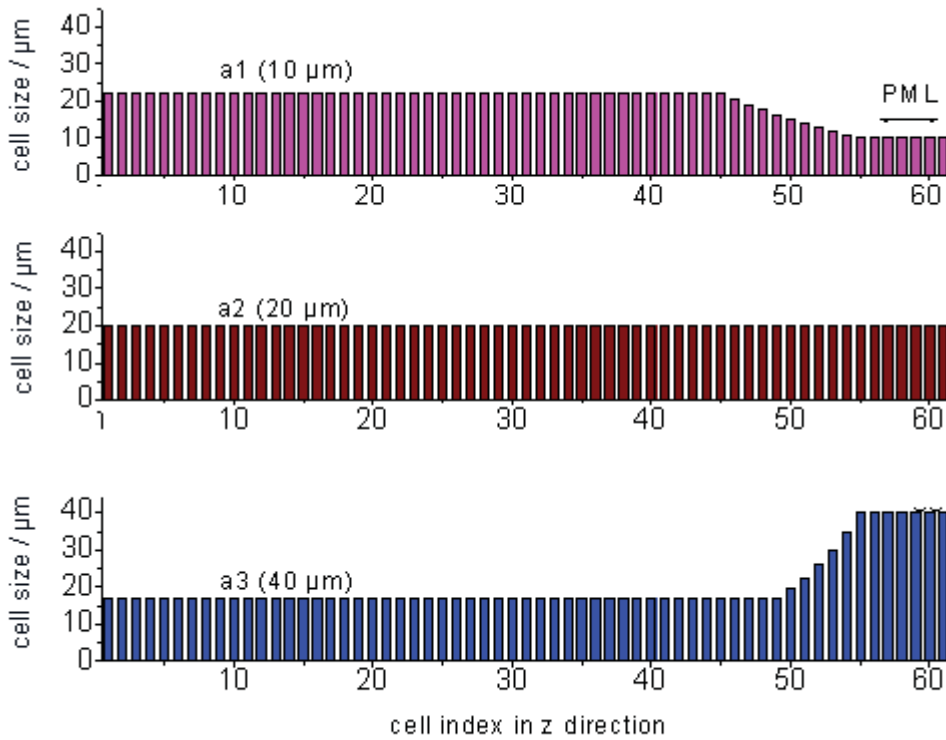


Fig. 2.11 Discretization schemes in the longitudinal z direction. The length of the structure is $1200 \mu\text{m}$. The last cell is an electrical wall and the PML wall consists of 5 cells adjacent to the electrical wall. PML cell sizes are varied from $10 \mu\text{m}$ to $40 \mu\text{m}$ and given in the brackets. The smallest and largest cells for $a1$ and $a3$ are 10 and $17 \mu\text{m}$, and 22.3 and $40 \mu\text{m}$, respectively.

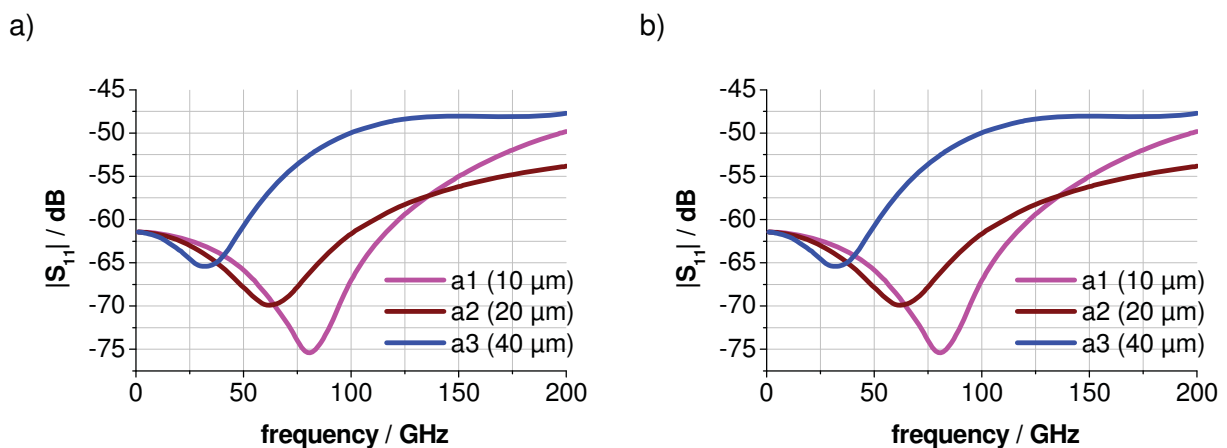


Fig. 2.12 Reflection coefficients for the different longitudinal discretizations according to Fig. 2.11. The graphs in (a) and (b) correspond to the lateral discretization schemes of Fig.2.10.a and b respectively. The PML cell sizes are given in bracket.

Regarding convergence, a3 with largest cells in the PML region shows the lowest number of iterations, which is below 500 up to 200 GHz, in both the cases of the lateral discretizations (Fig. 2.13). The number of iterations of the smallest PML cells in the case of lateral discretization of Fig. 2.10.a is below 3000 (Fig. 2.12.a) whereas in the case of lateral discretization of Fig. 2.10.b it is above 5000 (Fig. 2.13.b). The reason behind this increase in iterations is that in the case of Fig. 2.10.b we have higher number of cells (35, 24 and 61) than in the case of Fig. 2.10.a (24, 17 and 61).

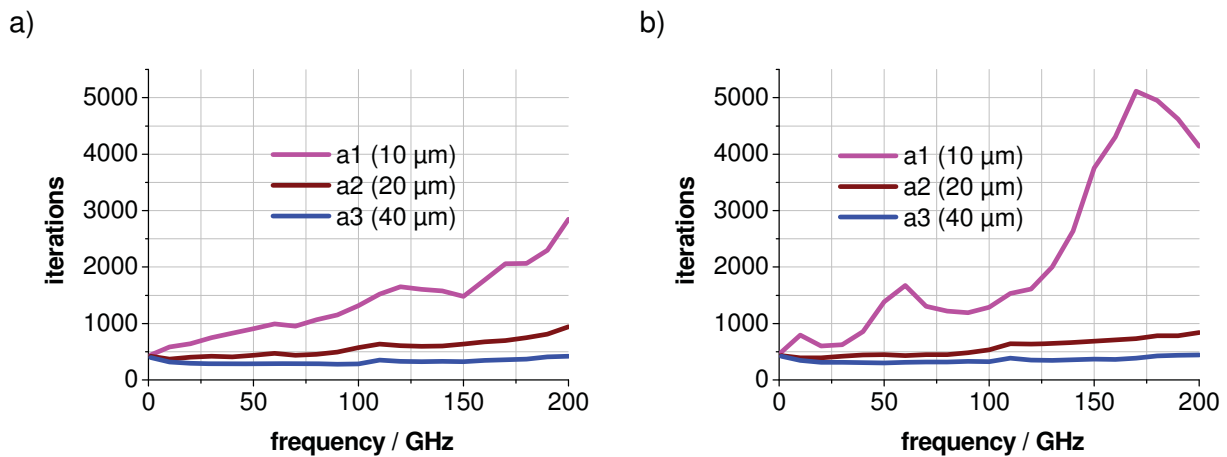


Fig. 2.13 Number of iterations for the different longitudinal discretizations according to Fig. 2.11. The graphs in (a) and (b) correspond to the lateral discretization of Fig. 2.10.a and b respectively. The PML cell sizes are given in bracket.

In order to better compare the number of iterations for the two cases of cross-sectional discretizations, the iterations per cell are plotted in Fig. 2.14. In this figure it is clear that in all cases (a1, a2 and a3) the number of iterations in (b) are lower than in (a). In both cases when the PML cells in the longitudinal direction are the largest ones we have the lowest number of iterations. Regarding the left pictures the largest PML cells (a3, 40 μm) are smaller than the largest cells in the x (167 μm) and in the y (136 μm) directions. Regarding the right picture the largest PML cells (a3, 40 μm) are larger than the cells in the x and y directions. We conclude that the PML cells must not only be the largest cells in the direction of PML but also the cell sizes in other directions (in this case x and y) must be smaller than the PML cells – more definitely, PML cells must be the largest ones overall in order to reduce the iterations to the minimum.

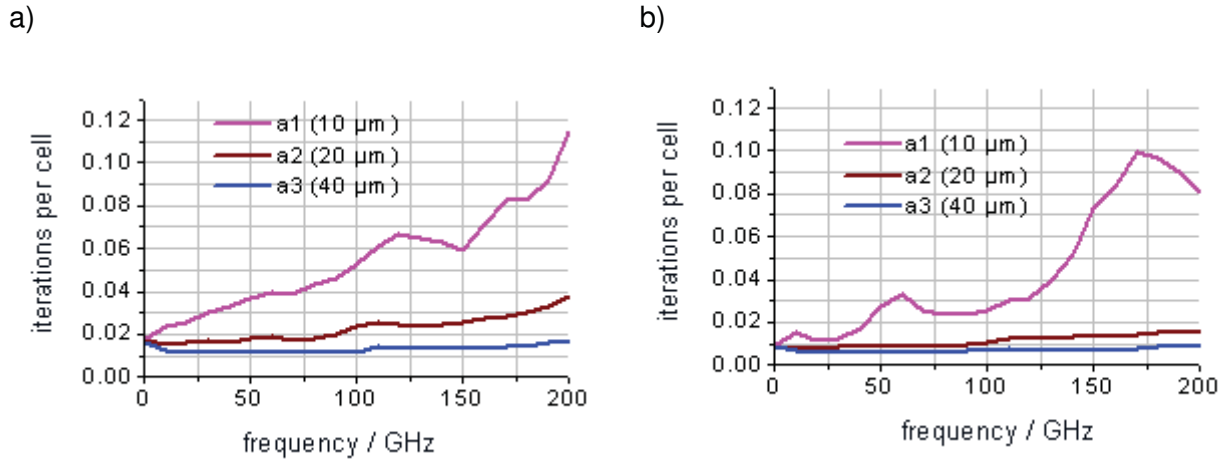


Fig. 2.14 The number of iterations per cell. The graphs in (a) and (b) correspond to the xy discretizations in Fig. 2.10.a and 2.10.b, respectively. PML cell sizes are in the brackets.

The parameter, ρ_{max} , as defined by equation 2.7, the maximum value of the ratios of the sum of the magnitudes of all the non-diagonal elements to the magnitude of the diagonal element of the system matrix, are drawn with respect to frequency in Fig. 2.15. We see here a correlation with the number of iterations, which, however, provides no point-to-point relation, rather an overall mapping is evident. The graphs in (a) and (b) correspond to the number of iterations given in left- and right-hand graphs in Fig. 2.14, respectively. In each case it is evident that ρ_{max} decreases with the decrease in the number of iterations. If we compare between the left and right pictures, we see that ρ_{max} 's of the right picture are lower than that of the left one. This gives the reasons why the number of iterations per cells given in Fig. 2.14.b are lower than those given in Fig. 2.14.a.

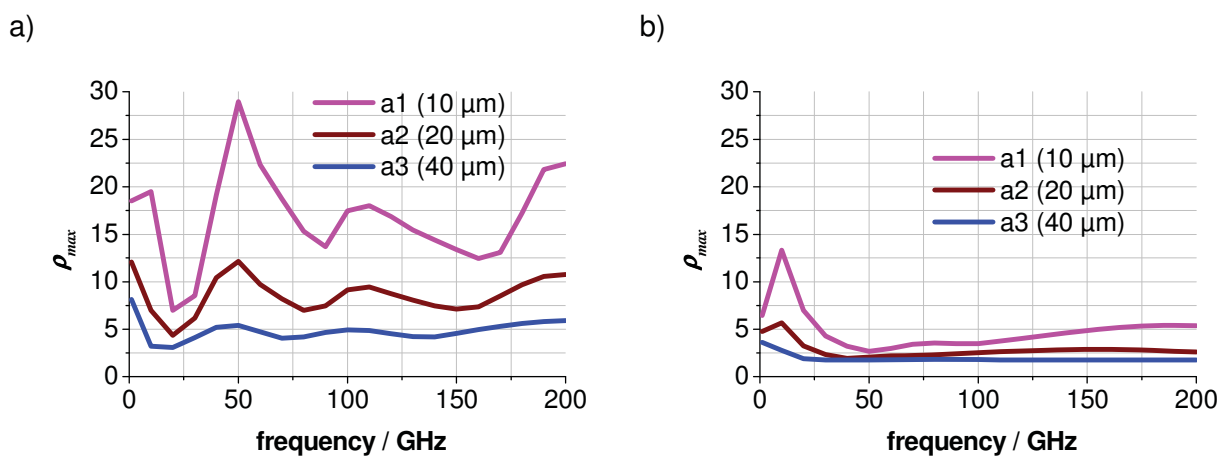


Fig. 2.15 Variation in ρ_{max} . The left and right pictures correspond to the xy discretizations in Fig. 2.10.a and 2.10.b respectively. PML cell sizes are in the brackets.

The general trend can be explained also in another way: in all the calculations presented above, a constant nominal reflection coefficient (r_{th}) is assumed, which refers to a constant attenuation in the PML region. According to equation 2.11, increasing the PML cell sizes (i.e. d) decreases in $|\text{Im}(\eta_i)|$ thus improving the numerical condition for a constant attenuation.

2.3.2 Multiple PML Walls : Patch Antenna

A single PML wall at the end of a MS as described in the previous section works as a matched termination of waveguide. Now we shall study a radiating structure, the patch antenna in Fig. 2.6.a. First, it is simulated with a single PML wall in x direction and then with multiple PML walls in all open directions (x, y and z directions) in order to estimate the optimum PML cell size regarding convergence. In each case PML walls consist of 5 layers followed by an electric wall. The PML walls are non-overlapping. In case of a single PML wall in the x direction, the other open boundaries in the y and z directions are terminated by magnetic walls. There are four, three and two different discretization schemes used in the x (Fig. 2.16), y (Fig. 2.17.a) and z (Fig. 2.17.b) directions, respectively.

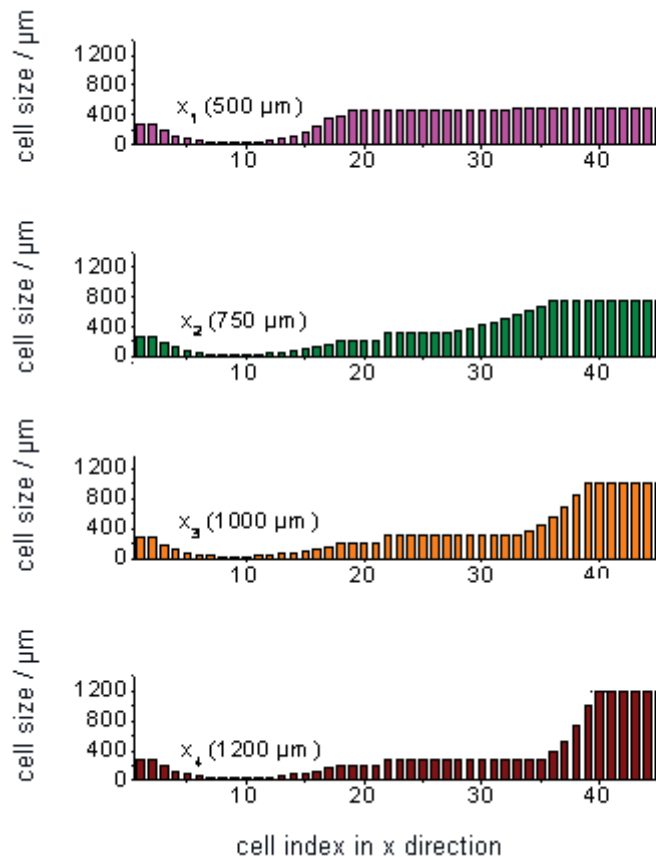


Fig. 2.16 The discretizations of the patch antenna in the x direction. The number of cells in the x direction is 45 in each case. The PML cell sizes are the largest cell sizes in each case and given in the brackets.

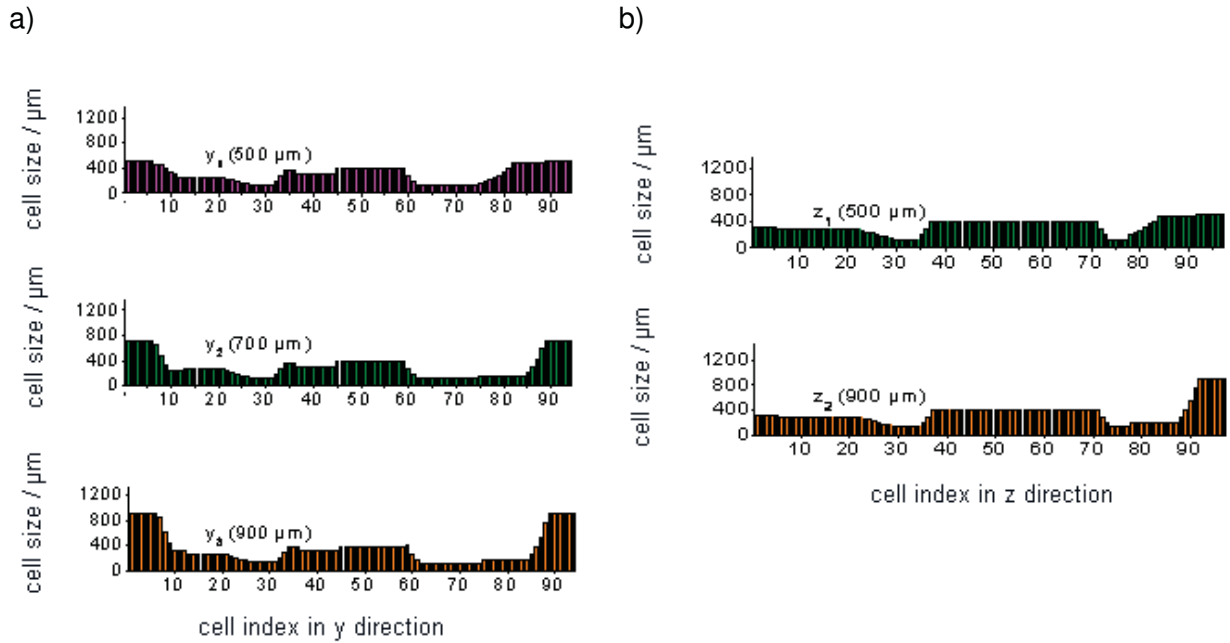


Fig. 2.17 The discretizations of the patch antenna in y (a) and z (b) directions. The numbers of cells in the y and z directions are 94 and 97, respectively. The largest cell sizes in each case are given in brackets.

First of all, a total of 24 simulations in combination of the discretization schemes in the x, y and z directions with each other are carried out with a single PML in the x direction where the cells with indices from 40 to 44 as depicted in Fig. 2.16 are defined as the PML cells. Considering all the simulation results with respect to the number of iterations, it is found that the number of iterations decreases as PML cell sizes in x direction increase. The most important simulation results are summarized in Fig. 2.18. In (a) the number of iterations goes down at 15 GHz from 5400 to 2500 when the PML cell sizes increase from $500\ \mu\text{m}$ to $1200\ \mu\text{m}$ where the largest cells in y and z directions are kept at $500\ \mu\text{m}$. In (b) the number of iterations decreases at 15 GHz from 7000 to 3750 as the PML cell sizes goes up from $500\ \mu\text{m}$ to $1200\ \mu\text{m}$ while keeping the largest cells in y and z directions at $900\ \mu\text{m}$. These two sets of results clearly suggest that the PML cells should be the largest ones in comparison to the non PML cells in all directions in order to obtain fast convergence. It should be noted that if the PML cell sizes are increased further, the decrease in number of iterations reaches saturation. It means further increase in the PML cell size will produce very little decrease in iterations. Again the PML cell sizes must not be larger than one tenth of the wave length in order to keep the dispersion error within an acceptable limit.

Now it must be checked what will happen regarding the number of iterations if PML walls are inserted in y and z directions as well. Again the 24 simulations as already used for the single x PML were carried out and the most important results are listed in Fig. 2.19. The cells with indices from 2 to 6 and from 88 to 92 in y direction (Fig. 2.17.a), and the cells with indices from 92 to 96 in z direction (Fig. 2.17.b) are defined as PML cells along with x PML cells defined as before. Comparing Fig. 2.18 and 2.19 it is noticeable that the inclusion of y and z PML walls raises the number of iterations in the lower frequency ranges making the iterations level almost constant from 3 to 15GHz. This is because the y and z PML cell sizes of $500\ \mu\text{m}$ (discretization. schemes: y_1 and z_1) are already in the saturation, i.e., the y and z PML cells

are already large enough and if they are increased to 900 μm (discretization schemes: y_3 and z_2) the iteration levels do not go down significantly. This can be seen by comparing left and right-hand graphs of Fig. 2.19. From this observation it can be stated that the PML cell sizes must be larger than the non-PML cell sizes in all directions, irrespective of PML directions. So optimizing the PML cell sizes (x_4 : 1200 μm , y_3 : 900 μm , z_2 : 900 μm) the number of iterations goes down below 2800. Comparing the reflection coefficients of this set of discretizations with that of the same structure simulated with CST Microwave Studio provides a very good matching as given in Fig. 2.20.

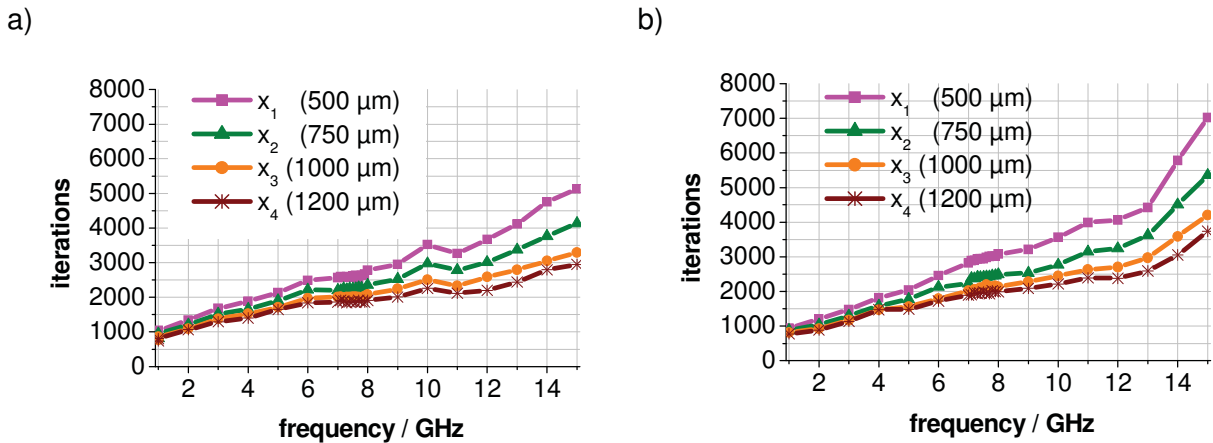


Fig. 2.18 : The number of iterations for a single PML in the x direction for different PML cell sizes with the discretization schemes according to Fig. 2.16. The graph in (a) corresponds to the discretizations in the y and z directions labelled by y_1 and z_1 in Fig. 2.17 respectively. The graph in (b) correspond to the discretizations in the y and z directions labelled by y_3 and z_2 in Fig. 2.17 respectively

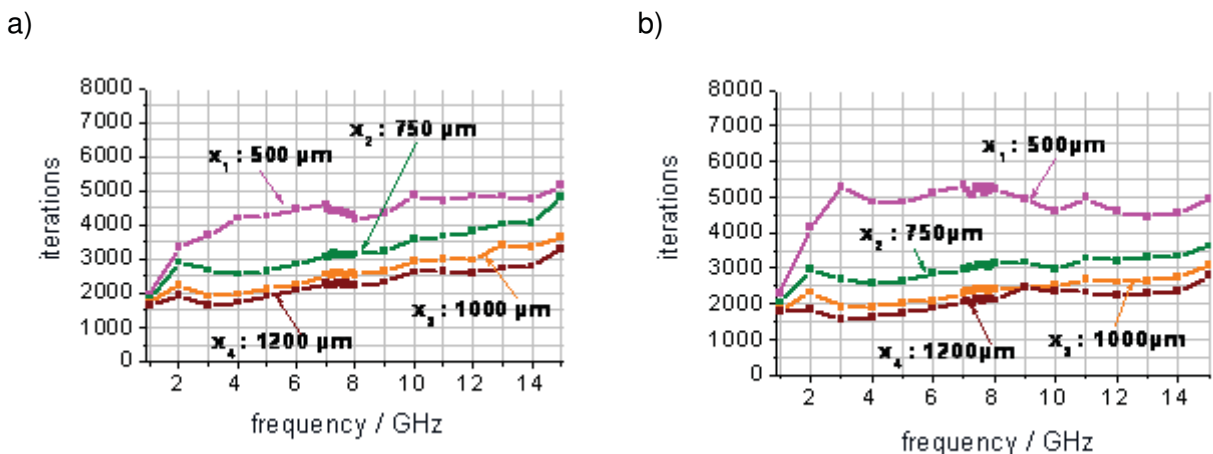


Fig. 2.19 : The number of iterations for multiple PML walls in the x, y and z directions for different PML cell sizes in the x direction with different x discretizations according to Fig 2.16. The graph in (a) corresponds to the discretizations in the y and z directions labelled by y_1 and z_1 in Fig. 2.17, respectively. The graph in (b) corresponds to the discretizations in the y and z directions labelled by y_3 and z_2 in Fig. 2.17, respectively.

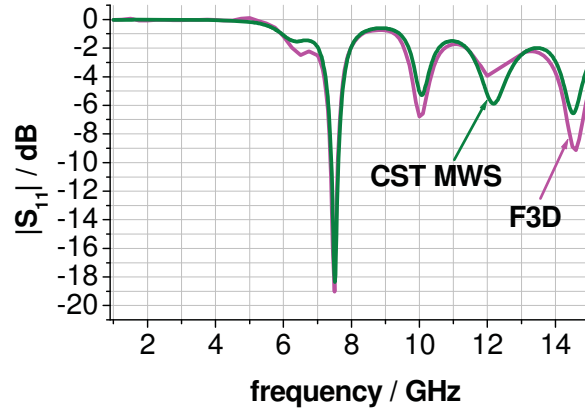


Fig. 2.20: The reflection coefficients of the patch antenna calculated using F3D and CST Microwave Studio (MWS). In F3D, calculation the discretizations used are x_4 , y_3 , z_2 of Fig. 2.16 and 2.17, respectively.

In the above investigations of the patch antenna, the PML cell sizes in all x , y and z directions were already larger than the non-PML cells and then their values were increased. We shall check the number of iterations when some of the PML cells are smaller than non-PML cells for this structure with multiple non overlapping PML walls. The mesh size of the patch antenna (Fig. 2.16 and 2.17) was 410310 ($45 \times 94 \times 97$) which was necessary to keep the mesh size same for all the discretization schemes while varying the PML cell sizes in x , y and z directions.

In reality we do not need such a high resolution for this simple patch antenna. After knowing that we need PML cell sizes larger than non PML cell sizes in all direction to make the iteration level low, we can now discretize the structure in a more convenient way to keep the PML cells the largest ones. The new mesh of the same antenna structure is now 25272 ($26 \times 36 \times 27$). The aim of the following investigations with smaller mesh size is to show that mesh optimization by using larger PML cell sizes is true not only for a particular mesh size with different cell sizes, but also for different mesh sizes of a particular structure.

First of all, the structure of the new mesh is simulated with different PML cell sizes in the x direction, varying from $400 \mu\text{m}$ to $1500 \mu\text{m}$ according to Fig. 2.21 while the PML cell sizes in both the y and z directions are kept constant at $1500 \mu\text{m}$ and $2200 \mu\text{m}$ respectively. The non PML cells in the y and z directions are smaller than the PML cells. Fig. 2.22.a shows the comparison in the number of iterations for these three types of discretization schemes with different PML cell sizes in x direction. The number of iterations can be reduced by 86% at 7 GHz by increasing the PML cell sizes from $400 \mu\text{m}$ to $1500 \mu\text{m}$. Fig. 2.22.b shows that the resulting S-parameters do not vary due to the change in PML cell sizes. It should be noted here that in the previous investigations of the patch antenna the criterion to terminate the iterative solver was $1.0\text{e-}08$ and in the investigations of Fig. 2.22 the value is taken $1.0\text{e-}02$. However in both the cases holds the argument that if the PML cells larger than the non-PML ones, this results in a significantly lower number of iterations.

The same calculations were performed for PML cell sizes in the y and z directions while keeping the PML cell sizes in other directions larger than the non-PML cell sizes. The results supported the previous findings.

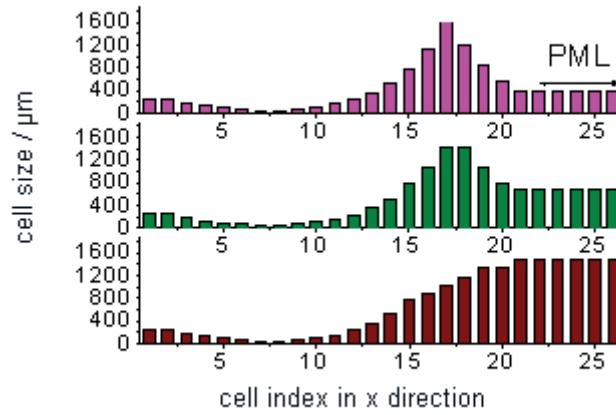
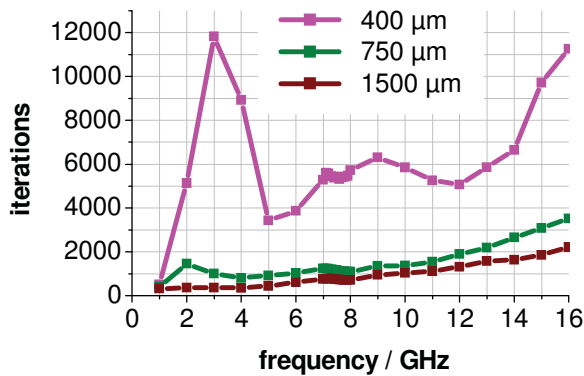


Fig. 2.21: The discretization schemes in x direction of the patch antenna given in Fig. 2.6.a. The PML cells are with indices from 22 to 26. The PML cells sizes are 400 μm (top), 700 μm (middle) and 1500 μm (bottom). The size of the largest non-PML cells in x direction are 1623 μm (top), 1430 μm (middle) and 1343 μm (bottom).

(a)



(b)

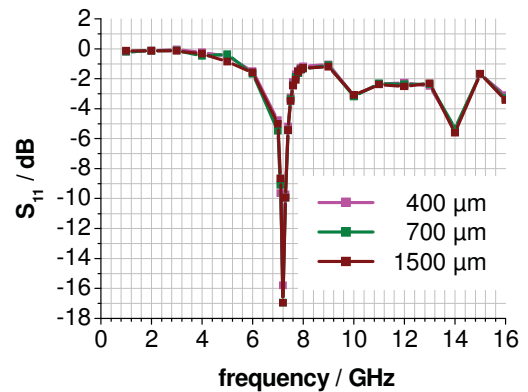


Fig. 2.22 : The number of iterations (1a) and reflection coefficients (b) for the different PML cell sizes in the x direction according to Fig. 2.21.

2.3.3 Slot Antenna

The 4-quadrant slot antenna [36, 37] as shown in Fig. 5.2 was developed for near-range sensor communications. The antenna provides lateral radiation and matches with the common flip-chip type of integration. The resonant properties of the antenna enable it to be used as an input / output filter. An active chip can be inserted inside the slot and can make the antenna self-dependent. The challenges of designing the slot antenna and simulation (in FDFD with the F3D simulator) as well as measurement results will be demonstrated in Chapter 5. The antenna is excited with an internal port. The properties of the internal ports in FDFD method will be discussed in Chapter 4.

Here the antenna will be used as an example to check the PML cell size and its influence on the convergence. All the open boundaries are terminated by PML boundary conditions. Three simulations are carried out with half of the structure (see Fig. 5.4). In the first one, the PML cell sizes are so chosen that the ratio between the PML cell sizes and the largest non-PML cell sizes in each direction varies between 0.8 and 0.9. The ratios vary between 2.3 and 2.4 in the second simulation and between 3.4 and 4.4 in the third simulation. The non PML cell sizes (the inner mesh) remains same for all the three cases. So, in the first case the PML cell sizes are smaller than the non-PML cell sizes and for the other two cases it is vice versa.

The simulation results are plotted in Fig. 2.23. When the PML cells are smaller than the non-PML cells, iteration count exceeds 6500 up to 47000, where as when PML cells are larger than the non-PML cells, the iteration count is lower than 2200. The resulting S-parameters are compared with each other of the three simulations, together with a comparison with CST MWS in time domain. There exists a very good fitting in the reflection coefficient curves.

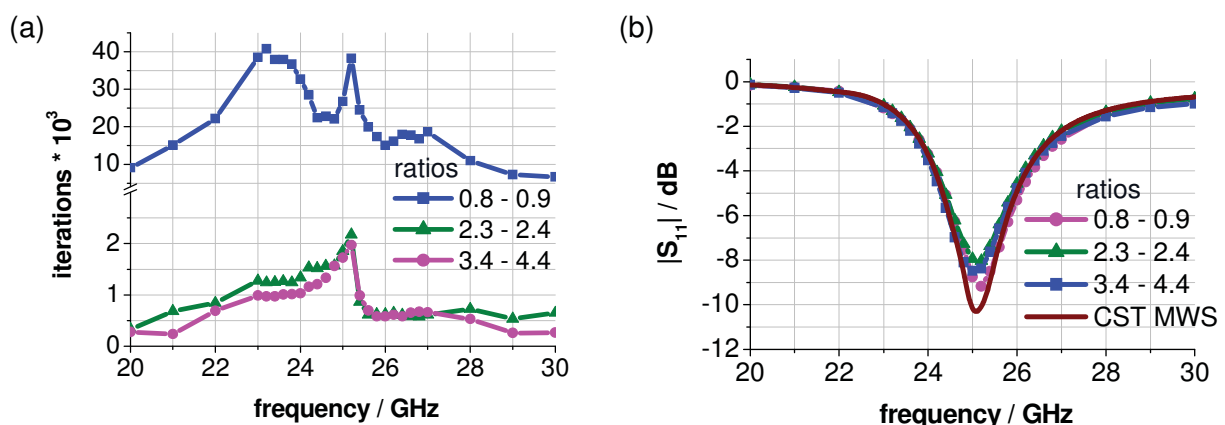


Fig. 2.23: The number of iterations (a) required to simulate the slot antenna of Fig. 5.4 for different ratios between PML cell size and the largest non PML cell size. The number of mesh cells is 290244 in all cases.

The reflection coefficients (b) for different ratios between PML cell size and the largest non-PML cell size. The comparison with CST MWS (FDTD method) for the same structure is also included.

2.4 PML in Layered Media

In this sub-section, the question of how to estimate the artificial electric and magnetic conductivities of the PML medium in the presence of layered media is addressed. In order to calculate these conductivities for a given nominal reflection (r_{th}) error a thumb rule is developed to estimate the dielectric constant of the PML region. These investigations are important, because on one hand, the given nominal reflection error (which depends on the dielectric constant of the PML region) and the calculated absorption level of the PML after the FDFD simulation must be same, on the other hand, the given nominal reflection error has significant influence on convergence.

The PML medium is defined by the artificial electric and magnetic conductivities. In order to show how they must be chosen in the FDFD method, the PML tensor is presented here again by 2.12. σ_E and σ_M are the electric and magnetic PML conductivities. In [25] it is shown that if σ_E and σ_M are assigned at cell edges and cell centers, respectively, better absorption by the PML wall is achieved than if both σ_E and σ_M are considered to be located at the cell centers. From the resulting S-parameters of that work it is evident that the reflection coefficient at the lowest frequency does not approach the nominal reflection coefficient (r_{th}). This is due to the missing term of the relative effective dielectric constant for the PML medium (ϵ_{rpm1}) in the calculation of σ_E from given a r_{th} . Now after including ϵ_{rpm1} [19] the equation of calculating σ_E becomes as given by 2.13. Here p denotes the order of polynomial variation and d the thickness of the PML wall. The term ϵ_{rpm1} should not be confused with the effective dielectric constant (ϵ_{reff}) of a certain mode; ϵ_{reff} varies with the frequency between the lowest and highest dielectric constants of the available media in the waveguide cross section. ϵ_{rpm1} is an approximate value selected from the range of ϵ_{reff} for the whole frequency range and has a significant influence on the absorption level.

$$[\bar{\eta}] = \begin{pmatrix} \eta & \mathbf{0} & \mathbf{0} \\ \mathbf{0} & \eta & \mathbf{0} \\ \mathbf{0} & \mathbf{0} & \frac{1}{\eta} \end{pmatrix}; \quad \eta = \mathbf{1} - \frac{j\sigma_E}{\omega\epsilon_0}; \quad \sigma_E = \sigma_M \frac{\epsilon_0}{\mu_0} \quad (2.12)$$

$$\sigma_E = \frac{\epsilon_0 c_0 (p+1) \ln(r_{th})}{-2d \sqrt{\epsilon_{rpm1}}} \quad (2.13)$$

According to the new formulation, the MS structure of Fig. 2.9 with lateral and longitudinal discretization schemes given by Fig. 2.10.b and 2.11 (a3) respectively is simulated again with an r_{th} of -60dB for different assignments of σ_E and σ_M . The resulting S-parameters and the number of iterations are drawn in Fig. 2.24. It is clear from Fig. 2.31.1 that locating σ_E and σ_M at the cell edge and cell center, respectively, results in a better absorption. Furthermore, the reflection coefficient at the lowest frequency approaches the r_{th} value of -60dB . It should be noted that the resulting reflection coefficient ($|S_{11}|$) should approach r_{th} , at least at the lowest frequency, because the PML serves here as (matched) absorbing layer. On the other hand, there is not any change in the iteration level for the different assignment of σ_E and σ_M .

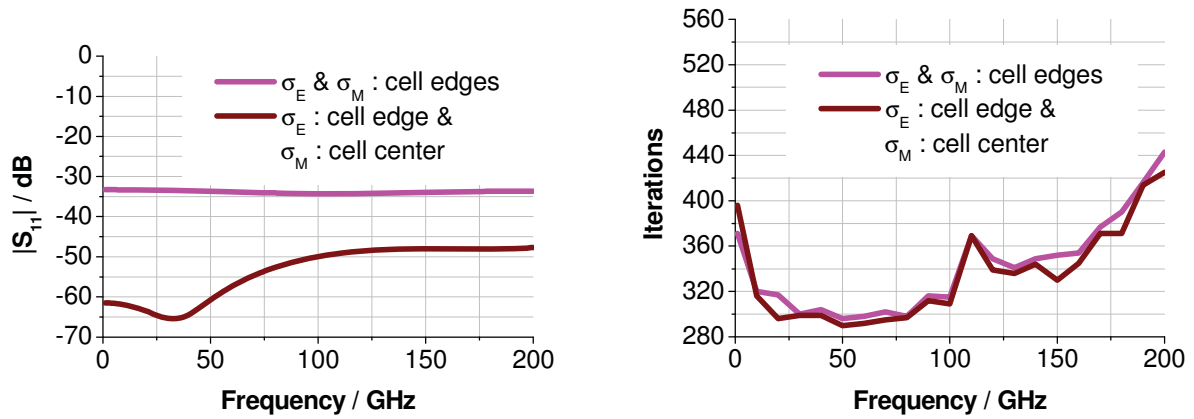


Fig. 2.24 Reflection coefficients (left) and the number of iterations (right) of the MS structure of Fig. 2.9 for the different definitions of electric and magnetic PML conductivities.

It will be shown in the following how to estimate the value of ϵ_{rpml} for a layered medium with the help of the MS structures of Fig. 2.25. All the dimensional information of the structures are given in Tab. 2.2. In all cases a PML wall at the end of the structure is added and the absorption by the PML wall is verified while varying the parameters of substrate thickness and ϵ_{rpml} .

We shall start our investigation with the structure of Fig. 2.25.a. In the PML we have three different media other than the PML medium for this structure: air (1.0), PEC (strip) and ceramic (9.8). ϵ_{rpml} is varied from 1.0 to 9.8 for the calculation of σ_E yielding r_{th} from -20 dB to -60 dB. The resulting S-parameters are drawn in Fig. 2.26. We see in both that the reflection coefficients approach the nominal value r_{th} if ϵ_{rpml} is equal to 9.8. The explanation is that most of the fields are concentrated in the ceramic substrate and its periphery to air around the strip.

Starting with this simple layered structure, we intentionally add another thin-film layer of LiTaO_3 ($\epsilon_r = 40.0$, Fig. 2.25.b). For this structure ϵ_{rpml} is varied from 1.0 to 40.0 with an r_{th} value of -20 dB. The resulting S-parameters for two different thicknesses of the thin film are plotted in Fig. 2.27. An average value of ϵ_{rpml} is calculated according to equation of 2.14, where t_i 's are the thicknesses of the different layers (except strip) and ϵ_i 's are the relative dielectric constants of the layers.

$$\epsilon_{rpml}^{average} = \frac{\sum t_i \cdot \epsilon_i}{\sum t_i} \quad (2.14)$$

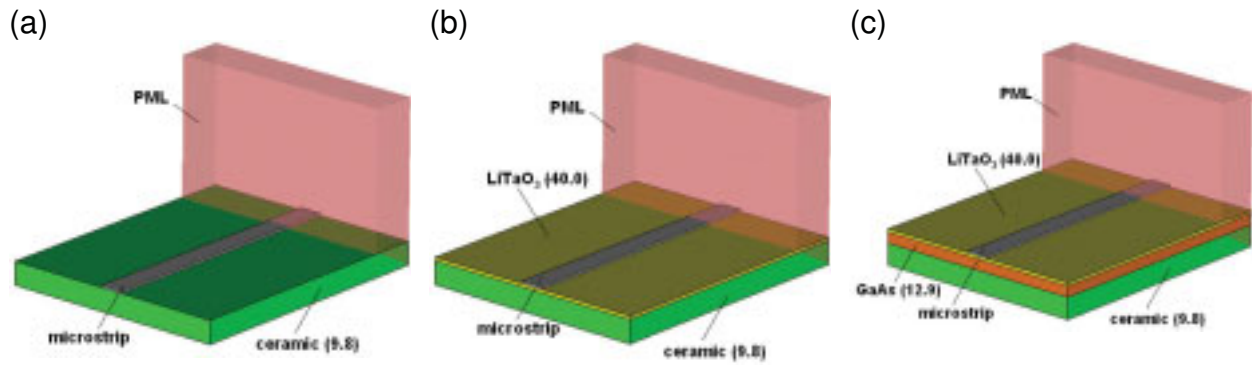


Fig. 2.25 a) MS line on ceramic substrate. b) Microstrip line on thin-film of LiTaO₃ and ceramic substrate. Thickness of thin film, t_{TF} , is varied from 1 to 50 μm . c) Microstrip line on a sandwich structure of GaAs, thin-film of LiTaO₃ and ceramic. All the details of the structures are listed in Tab. 2.2. The dielectric constants of ceramic, GaAs and LiTaO₃ are 9.8, 12.9 and 40.0, respectively.

	thickness (μm)			direction	discretization		
	a	b	c		a	b	c
t_{ms}	10	10	10		dim. (μm), num. of cells	dim. (μm), num. of cells	dim. (μm), num. of cells
$t_{ceramic}$	100	100	100	X	700, 35	700 & 754, 41 & 43	710, 43
t_{TF}	-	1 & 50	10	Y	500, 24	500, 24	500, 24
t_{GaAs}	-	-	50	Z	1200, 61	1200, 61	1200, 61

Tab. 2.2 Thicknesses and dimensions of the structures given in Fig. 2.25. The width of the microstrip is 50 μm . x, y and z refer to the directions of thickness, width and length of the structures. Total number of cells in x, y and z directions is also attached in each case.

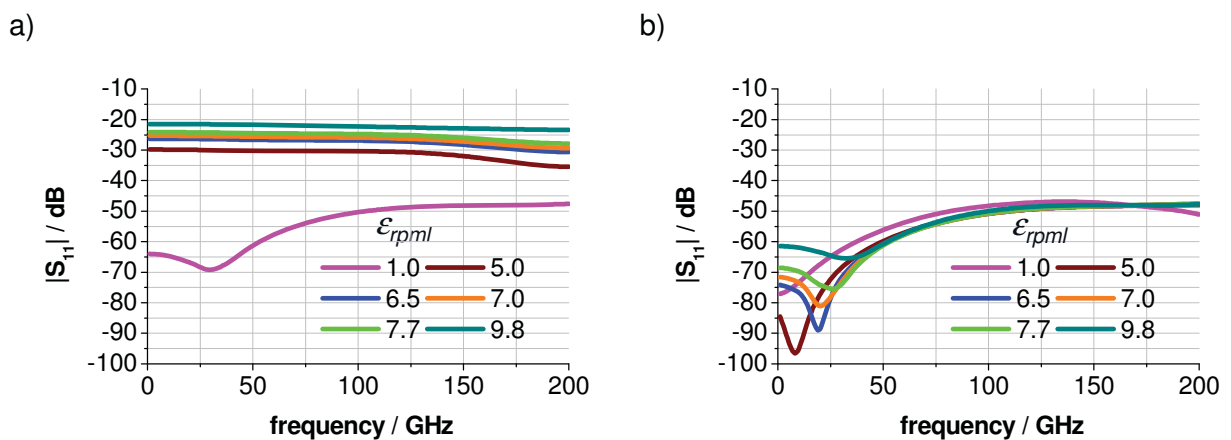


Fig. 2.26 The Reflection coefficients of the structure in Fig. 2.25.a for varying $\epsilon_{r_{pml}}$. (a) : $r_{th} = -20$ dB and (b) : $r_{th} = -60$ dB

Fig. 2.27 shows that none of the values of ϵ_{rpm1} results in a reflection coefficient equal to the nominal reflection coefficient (r_{th}) of -20 dB at the lowest frequencies. The reason for such deviation is again as stated before that most of the fields are concentrated in the ceramic, TF and near the substrate-air boundary. The same calculations are carried out except excluding the air space above the substrates in the calculation of average ϵ_{rpm1} . The Fig. 2.28 shows the resulting S-parameters with different r_{th} of -20 dB and -60 dB. The average values of ϵ_{rpm1} (10.1, 12.5 and 20.0) are calculated considering different thicknesses of thin film (t_{TF} : 1, 10 and 50 μm respectively). We see that in each case the reflection coefficients approach the value of r_{th} .

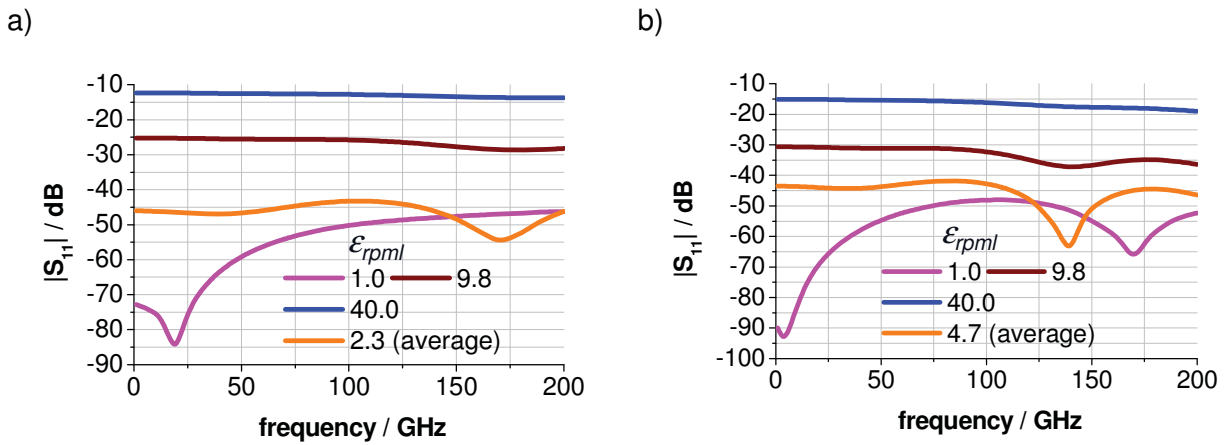


Fig. 2.27 Reflection coefficients for the structure in Fig. 2.26.b for varying ϵ_{rpm1} . $r_{th} = -20$ dB. (a) : $t_{TF} = 1 \mu\text{m}$ and (b) : $r_{th} = t_{TF} = 50 \mu\text{m}$.

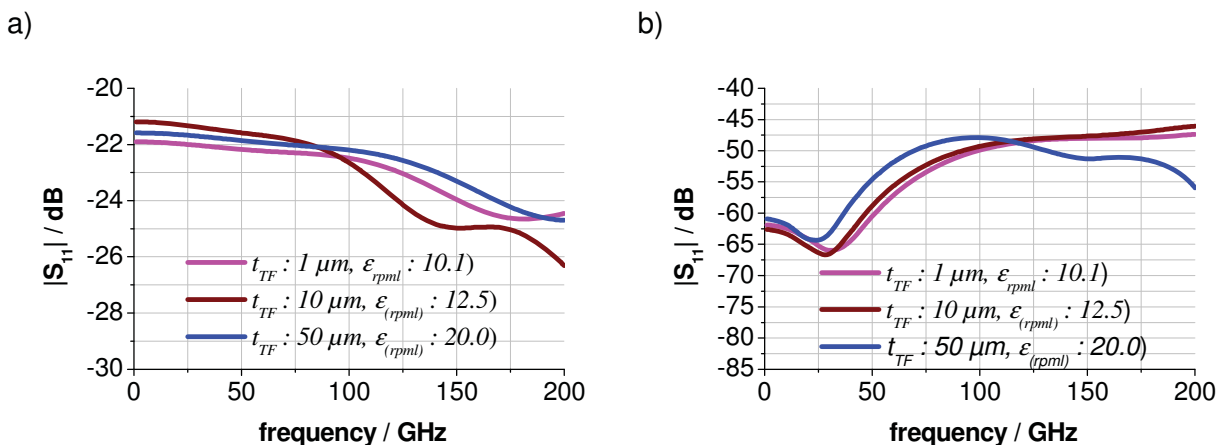


Fig. 2.28 Reflection coefficients for the structure in Fig. 2.26.b varying t_{TF} . The average ϵ_{rpm1} is calculated using 2.14. (a) : $r_{th} = -20$ dB and (b) : $r_{th} = -60$ dB

Finally the above mentioned experience is checked with the structure of Fig. 2.25.c. Here another layer of GaAs ($\epsilon_r = 12.9$) is added. Now $\epsilon_{r_{pml}}$ approximates 12.65 according to equation 2.14 without taking air into account and the resulting S-parameters are shown in Fig. 2.29.a. We see a very good matching with the r_{th} value at the lowest frequency (left picture). One observes that a thumb rule for $\epsilon_{r_{pml}}$ would be the average of the relative dielectric constants of different substrates according to 2.14, excluding the regions (i.e. air in Fig. 2.25) from the calculation where the field concentration is negligible compared to the other regions (i.e. substrates in Fig. 2.25). As becomes clear from Fig. 2.29.b, r_{th} has an influence on the number of iterations, interestingly lower r_{th} gives lower number of iterations at the higher frequencies.

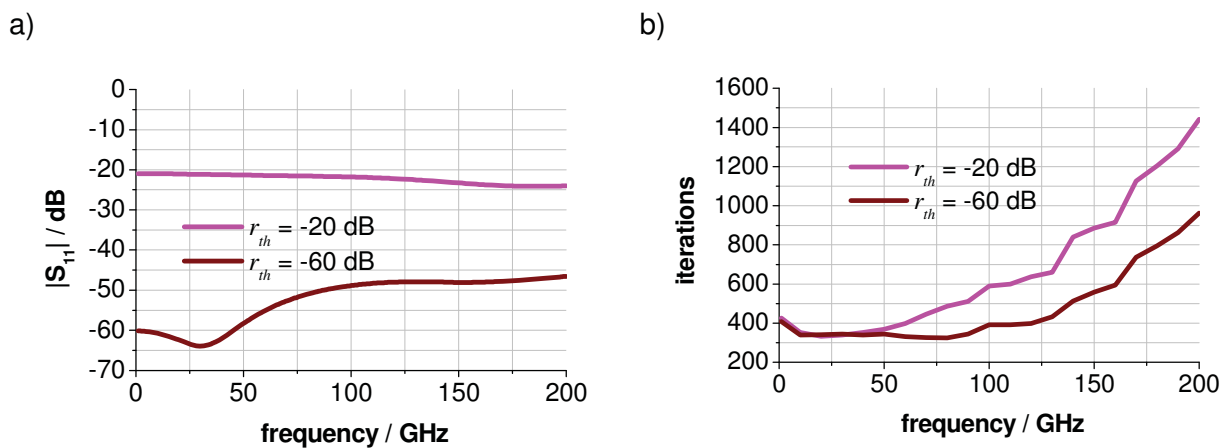


Fig. 2.29 Reflection coefficients (a) and the number of iterations (b) of the structure in Fig. 2.25.c for different r_{th} .

2.5 Improved Numerical Solver

In the course of this work, the Weierstrass-Institute (WIAS), Berlin optimized the F3D solver [10-13] in order to tackle the convergence by the PML walls. In the improved version, the solver is modified by rearranging the system matrix M given by equation 2.2. In the old version (unmodified version, called the old solver), the system matrix is preconditioned directly by the SSOR procedure followed by the iterative solution using the Krylov-Subspace method [14, 15]. As already mentioned (see the results of Fig. 2.8), the position of the rows (as well as matrix elements) in M has a great influence on the convergence and the reshuffling of the matrix elements can result in an improved convergence. Taking that in mind the solver was modified by using different sorting rules for “Independent Set Ordering” to accomplish the rearrangement of the system matrix. In this way the system matrix is reduced to a smaller dimension (Schur-complement, S) which can be solved faster after the usual SSOR preconditioning. This modified version will be called here new solver. The details of the modifications and procedure of the F3D solver are given in the Appendix 7.7.

In order to check the benefits of the new solver version over the old one the comparatively simple patch antenna structure of Fig. 2.30 will be demonstrated first. Both the old and new solvers are used to simulate the antenna separately with x and y PML as well as x and z PML walls including the overlapping regions. In both the cases the iterative procedure for a certain frequency is terminated either if convergence is reached or if the number of iterations exceeds 300,000 without convergence. The resulting numbers of iterations are given in Fig. 2.31. For the overlapping PML walls in x and y directions, the old solver does not converge already at 2 GHz whereas the new solver reaches the termination without convergence only at 16.5 GHz (Fig. 2.31.a). For the overlapping PML walls in x and z directions, again the old solver does not converge already at 2 GHz where as the new solver converges in the whole frequency range with an iteration count of 36,000 at 18GHz (Fig. 2.31.b). So the new solver works much better than the old one regarding the number of iterations when applied to the PML walls with overlapping regions. However, even though the new solver reduces the number of iterations significantly in the cases of overlapping PML walls, the number of iterations is still too high to be used in most practical cases. So we need non-overlapping PML and the other concepts described in the previous sub-sections.

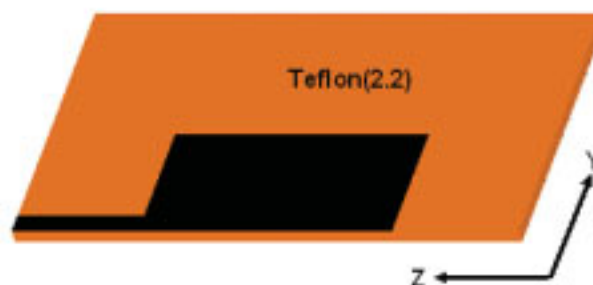


Fig. 2.30 Half of a rectangular patch antenna. The dimensions of the half patch, feeding microstrip line and computational domain are $(50\mu\text{m} \times 16000\mu\text{m} \times 16000\mu\text{m})$, $(50\mu\text{m} \times 1230\mu\text{m} \times 8000\mu\text{m})$ and $(14844\mu\text{m} \times 18000\mu\text{m} \times 32000\mu\text{m})$ in x, y and z directions respectively. The PML cell size and number of cells in x, y and z directions are $(1280\mu\text{m}, 1010\mu\text{m}, 1000\mu\text{m})$ and $(30, 25, 41)$, respectively.

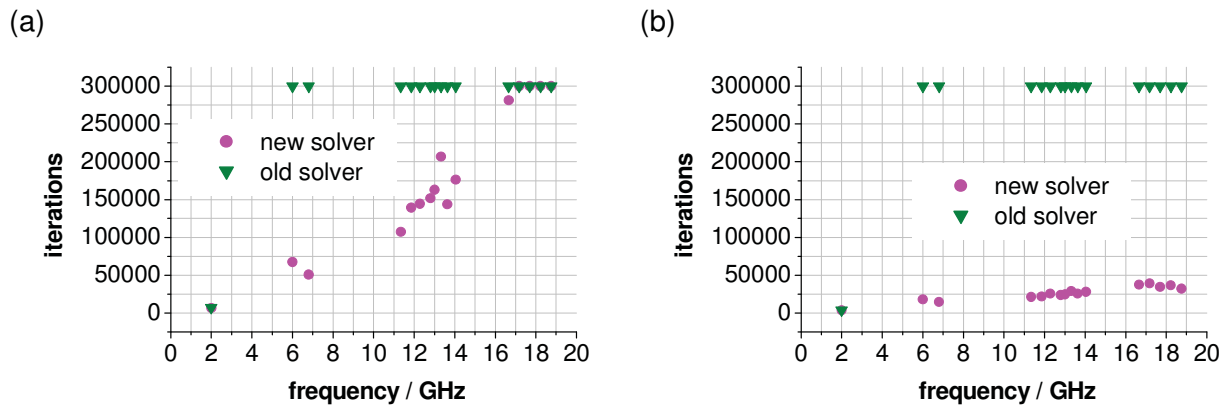


Fig. 2.31 Iterations of the patch antenna in Fig. 2.30 with overlapping PML walls in x and y directions (a), and, in x and z directions (b).

The new solver allows different sorting of the system matrix and thereby the rearrangement of the elements of the system matrix. The number of iterations depends significantly on the different sorting rules. The simulations corresponding to the results in Fig. 2.32 were carried out with the optimized sorting of the system matrix. The optimization of the sorting will be analyzed in the following with help of the patch antenna in Fig. 2.6.a (discretization schemes : x_4, y_3, z_4 ; Fig. 2.10 and 2.11). Fig. 2.32.a shows the comparison in the iteration count with the non overlapping PML walls in x, y and z directions for three different sorting rules of alternate ordering, reverse ordering and ISODEG ordering [14]. Depending on the sorting, the number of iterations can be reduced by 27% at 16 GHz. Also, the convergence is greatly dependent on another parameter called the relaxation factor, ω [15]. The value of ω lies between 1.0 and 2.0. Fig. 2.32.b shows the dependency of the number of iterations on ω at different frequencies. For all frequencies, the number of iterations increases abruptly for values of ω above 1.6...1.8. It has been found that 1.5 is a good choice for ω for the structures studied here, including patch antenna, MS line, CPW line, LTCC, Flip-chip etc.

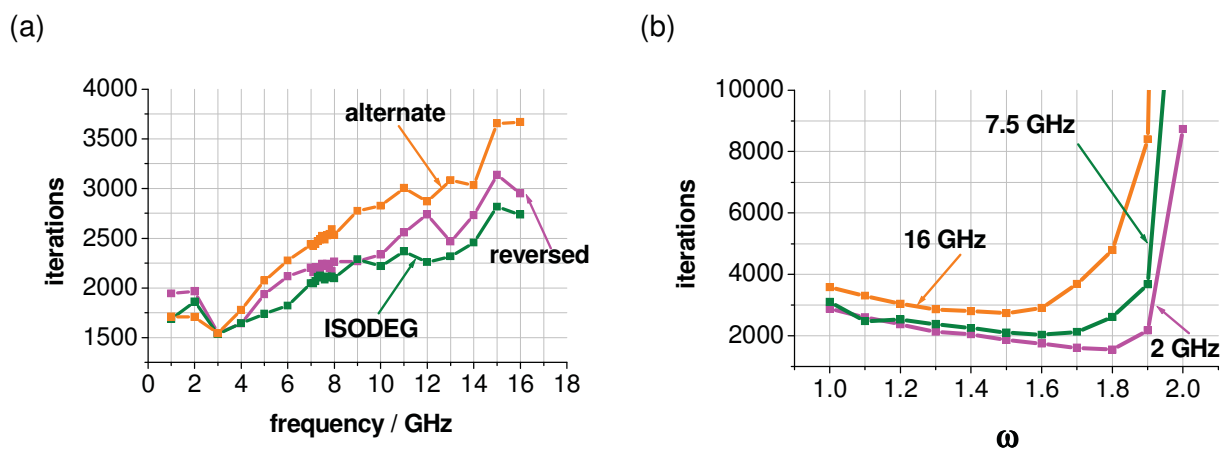


Fig. 2.32 The number of iterations for the different sorting of system matrix in using the new solver (a) and for different values of ω (b) applied to the patch antenna in Fig. 2.6.a with discretization schemes of x_4, y_3 and z_2 (Fig. 2.16 and 2.17)

Fig. 2.33 shows the influence of the new solver in comparison to the old solver for the case without PML and the case with non-overlapping PML. Now the same antenna in Fig. 2.6.a with discretization schemes of x_4 , y_3 and z_2 (Fig. 2.16 and 2.17) is simulated in order to check the influence of the new solver in comparison to the old solver for the cases without PML and non-overlapping PML. We see that there is a slight improvement in the higher frequency ranges in the case without PML when using the new solver. On the other hand, we see a 6 to 10% decrease in the number of iterations in the lower frequency ranges with the new solver in the non-overlapping PML case. As the matrix elements are frequency dependent, the sorting rules work better for different frequency ranges regarding the improvement in convergence. The ISODEG sorting is used for rearranging the system matrix in the new solver case whereas in the old solver case no sorting is used – no rearrangement of the system matrix. We see that ISODEG sorting in this case decreases the number of iterations in the higher frequency ranges for the non-PML case (slightly), and in the lower frequency ranges for the non-overlapping case.

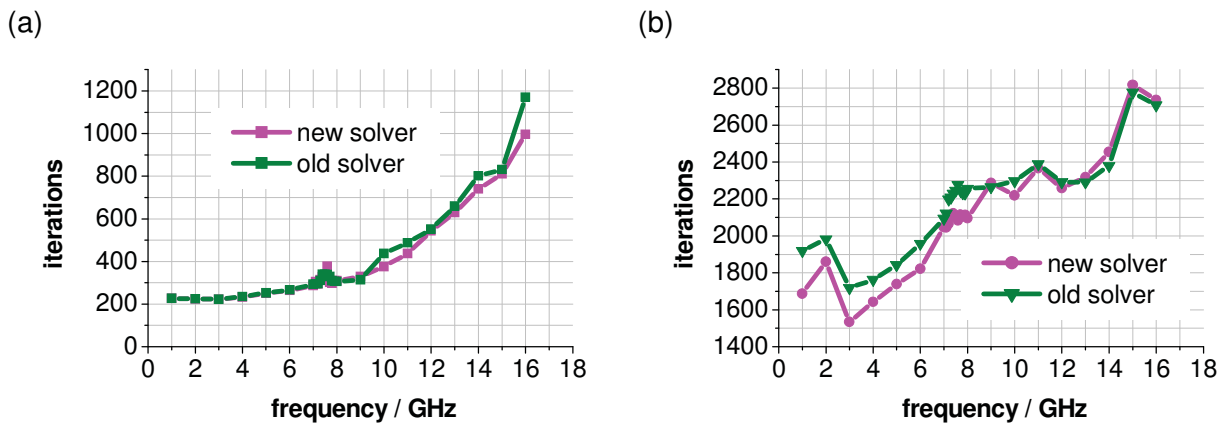


Fig. 2.33 The number of iterations of the patch antenna in Fig. 2.6.a with discretization schemes of x_4 , y_3 and z_2 (Fig. 2.16 and 2.17) for the case without PML (a) and for the case non overlapping PML walls in x , y and z directions (b) in relation with the old and new solvers.

The patch antenna structures studied before are relatively simple and might not provide the full picture with regard to the solver's potentiality. Therefore, the comparatively complex flip-chip structure with non overlapping PML walls in Fig. 2.34 is analyzed in the following. Non-overlapping PML walls are used in the lateral direction to replace the open boundaries. The resulting iteration numbers are plotted in Fig. 2.35. We see that the ISODEG sorting of the new solver provides an overall improvement in convergence in comparison to the old solver in the whole frequency range with a decrease in the number of iterations by 10 %. By choosing the reverse sorting, the number of iterations can be reduced by 20%, but only in the lower frequency ranges.

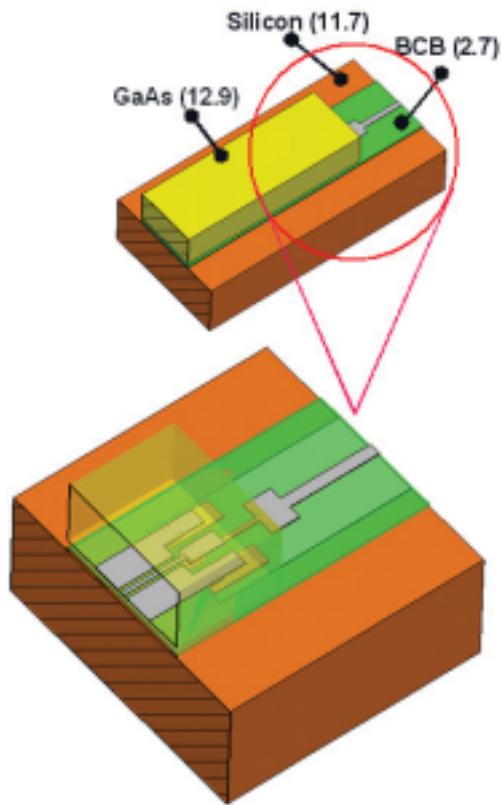


Fig. 2.34 MS to CPW flip-chip interconnect.

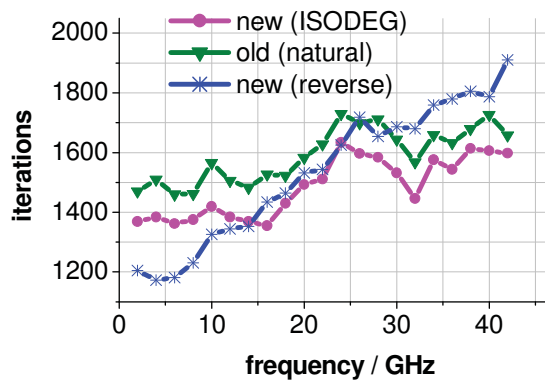


Fig. 2.35 Comparison of the new and old solver: number of iterations against frequency for the flip-chip structure of Fig. 2.34.

2.6 Conclusion

The influence of the PML boundaries on the convergence of the iterative solution can be summarized as follows: PML enlarges the range of the magnitudes of the elements of the system matrix. It is shown that due to the PML, several rows of the system matrix are affected where the non-diagonal elements become significantly larger in magnitude than the main diagonal ones. The outcome is that the condition number of the system matrix grows and, consequently, the number of iterations (thereby the CPU time) when solving the system of equations increases drastically.

This effect can be mitigated, of course, by improving the mathematical solver applied, as it is described in Sec. 2.5. However, the resulting improvements are not significant enough to solve the problem. Two main issues have been found:

- 1) Overlapping PML regions at edges and corners make the usage of the PML boundary condition almost impossible for practical microwave structures. It comes out that by avoiding any overlapping, the high count of the number of iterations can be lowered very significantly without sacrificing accuracy too much.
- 2) PML cell size is the most important parameter regarding the convergence of the iterative solution. The investigations on several structures like micro-strip, patch antenna, flip-chip interconnect, spiral inductor, coupler, reveal that by making the PML cell sizes the largest ones in the whole mesh, the iteration level can be lowered drastically.

Finally, a thumb rule is developed for estimating the relative dielectric constant in the PML region, if the PML wall is inserted in a layered media, thus ensuring that the absorption level of the PML approaches the given nominal reflection error.

3 Waveguide Port Simulation with PML

Mostly, three-dimensional (3D) simulations of passive structures are carried out through waveguide port excitations. Even though only the desired physical modes are to be excited at the wave guide port, parasitic artificial modes are also excited due to the finite boundary of the calculation domain. Inclusion of PML as open boundary makes the situation even worse, e.g. because it excites modes at the waveguide port with complex propagation constants (γ) even if the investigated structure is loss free.

The goal of this chapter is to investigate the changes in mode spectrum of a longitudinally homogeneous structure due to PML. A simple MS structure is used to describe the effects of PML on mode spectrum at the waveguide ports.

3.1 Physical and artificial modes

As the FDFD method deals with a boundary value problem, the waveguide ports support two types of modes. The first ones are the physical modes that are related to the physical waveguide (MS, CPW lines for example). The second ones are artificial modes, also called box modes, which exist due to the boundary which is introduced only for the simulation purposes and is not present in reality. Correspondingly, these modes depend on the size and type of the boundaries, electric or magnetic walls, for example. The box modes have usually nonzero cutoff frequencies whereas the physical modes may have zero cutoff frequencies (e.g. MS, CPW modes) and nonzero cutoff frequencies (e.g. higher order substrate modes). The box modes like the physical modes are able to propagate along the waveguide and thereby may interfere with each other whenever there is a discontinuity along the waveguide. If there are n_p numbers of conducting lines at the wave guide port, the number of physical modes with zero cutoff frequency is equal to $(n_p - 1)$ assuming that the dimensions of the lines are sufficiently small compared with the wavelength.

One should note that this distinction between physical and artificial modes does not apply strictly over the entire spectrum. This is because of the FD discretization. For the discretized structure, one has a fixed number of modes, which solely depend on the number of mesh cells of the waveguide. More precisely, the number of eigenvalues which is equal to twice the number of mesh cells (N) at the port. Therefore, in the range for high $|\gamma| = |\alpha + j\beta|$, there are a lot of modes which are more or less determined by the discretization only and thus neither physical nor box modes.

PML boundary conditions are used in order to simulate open space. So the box modes existing due to the artificial boundaries should not appear when PML walls are used. Since the total number of modes is fixed (see above), these modes can not be eliminated but only shifted in the spectrum, desirably to a range far away from the physical modes. However PML is designed to absorb waves impinging onto the PML. It is not equally suitable as a lateral boundary of a waveguide. Therefore, not all the box modes are shifted properly and they may appear between the physical ones.

One has to find out how to distinguish among physical, box and rest of the artificial modes in using PML. One possibility is the criterion PPP (Power Part in PML) which is defined in [25] as the ratio between the power of a particular mode in the PML region and the total power of that mode calculated at certain waveguide port. Accordingly, the modes which have comparatively large PPP values will be defined here as PML modes. Obviously the PML modes belong to the group of artificial modes. The PPP values of the physical and box modes depend on the amount of fields in the PML region. However, it turns out that only based on the PPP values the PML modes can not be separated from the desired physical modes. The PML modes and their effect on physical and box modes will be described in the next sub-chapter.

A MS structure (Fig. 3.1.a) is used to show the appearance of all these physical and artificial modes. A discontinuity of two MS lines with different widths is used devotedly to check the coupling of MS mode to other modes. Except for strip width, the waveguide ports (port 1 and 2) are the same at both ends of the structure. The cross section of port 1 is depicted in Fig. 3.1.b. The structure is simulated with and without PML. When simulated with PML, two PML walls (designated by X- and Y-PML) are used and when simulated without PML, the PML regions are just replaced by the corresponding neighbouring materials (e.g. air and ceramic). So in both cases the outer dimensions of the structure remain the same. The PML walls are followed by magnetic walls (MW), whereas another magnetic wall (symmetry plane) is used to simulate only half of the structure and the ceramic substrate is grounded by electric wall (PEC). PML walls are used in such a way that PML cells are the largest ones. An overlapping PML wall is used at the crossing of X- and Y- PMLs in the investigations of this sub-chapter in order to stick to the basic PML definition [18], however, it is found that XY non overlapping PML walls show the same effects as the overlapping PML does.

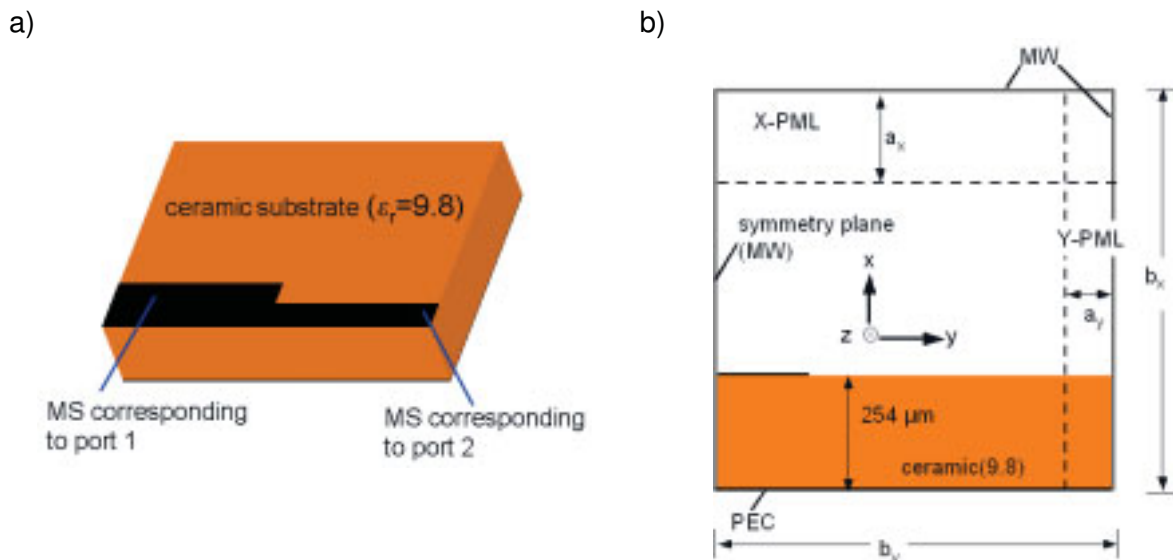


Fig. 3.1 (a): Discontinuity of two MS lines on ceramic substrate. The widths of the MS lines at port 1 and 2 are $210 \mu\text{m}$ and $110 \mu\text{m}$ respectively. The thickness of the metallization is $5 \mu\text{m}$. (b): Cross-sectional view at port 1. The thicknesses of the X-PML (a_x) and Y-PML (a_y) walls as well as the height (b_x) and width of the structure (b_y) are varied. The cross-section at port 2 is same as at port 1 except for the different width of the strip. The structure is terminated by an electric wall (PEC) at the bottom and otherwise by magnetic walls (MW).

In the waveguide simulation, referred to as 2D in the following, all the modes are sorted first by the ascending order of $|\alpha|$ (α being the imaginary part of the propagation constant) and then by the descending order of $|\beta|$ if $|\alpha|$'s of the two modes are same [11]. So the modes with smaller $|\alpha|$'s appear first. In this way the evanescent modes, which are not of interest in most cases, are shifted at the end of the mode list. On the other hand, the PPP criterion can be used to filter out the modes. The value of PPP varies between 0.0 and 1.0. So if PPP equal 1.0 is used all the modes are included and if PPP is 0.3, for example, only the modes whose power portion in the PML region is less than 30% are considered.

The MS structure of Fig. 3.1 is simulated without PML (non-PML) and with PML considering the first 10 modes in each port in both cases. PPP equal to 1.0 is used with PML case. The attenuation constants (α) and effective dielectric constants ($\epsilon_{r_effective} = (\beta/\beta_0)^2$) of these modes at port 1 in the cases of non-PML and with PML are shown in Fig. 3.2.a and 3.2.b respectively. Out of these 10 modes, mode 1 (m1) is the MS mode [42]. Mode 2 (m2) is the TM_0 mode and mode 6 (m6) is the TE_1 mode, both of these are surface wave modes, transversal magnetic and electric, respectively, to the perpendicular direction to the substrate (x direction). The rest of the modes are box modes. The field patterns of TM_0 and TE_1 modes are shown in Fig. 3.3.

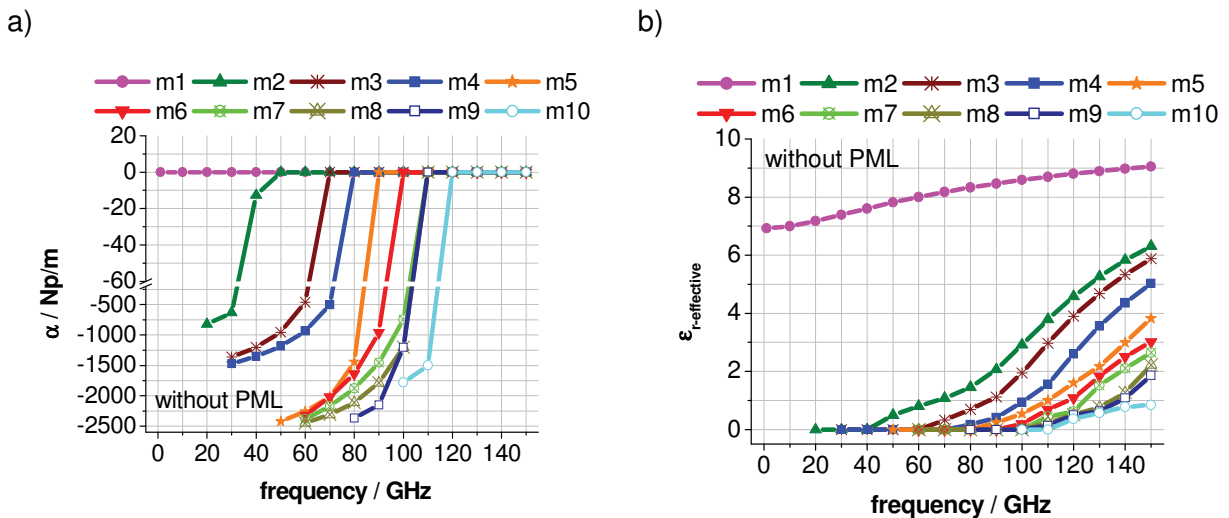


Fig. 3.2. Without PML: attenuation (a) and effective dielectric constants (b) at port 1 of Fig. 3.1 against frequency for different modes. $b_x = 1900 \mu\text{m}$ and $b_y = 2400 \mu\text{m}$.

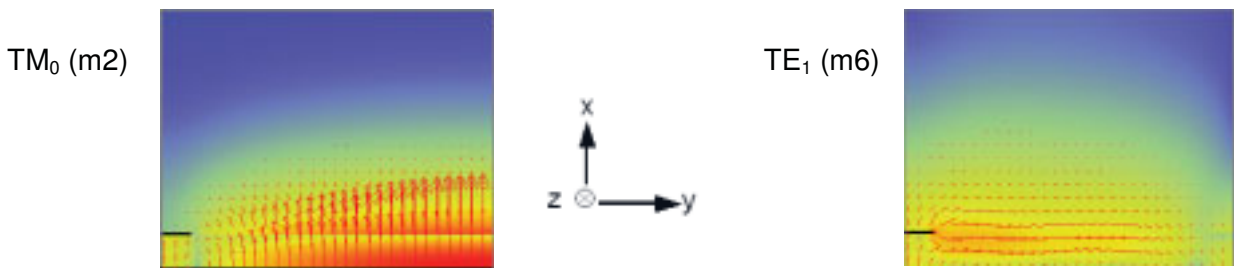


Fig. 3.3 Without PML: The electric fields of TM_0 and TE_1 modes appearing at port 1 of Fig. 3.1. TM_0 has the field components of E_x , E_z and H_y . TE_1 has the field components of E_y , H_x and H_z . [42,46]

It is worthwhile to discuss these surface wave modes in more detail. Not only a grounded dielectric waveguide but also other interesting waveguides like ungrounded dielectric slab, dielectric rod, corrugated conductor etc. support surface waves [42-44, 46]. Surface waves can also be excited on some types of planar transmission lines, such as MS line (e.g. Fig. 3.1), CPW line (e.g. Fig. 2.35) and slot line.

Surface waves have fields which decay away from the dielectric substrate while most of the fields remain in or near the air/dielectric interface. The higher the frequencies, the more tightly bound are the surface wave fields in the dielectric, so the surface waves guiding waveguides are mostly of practical interest at higher frequencies. Another interesting characteristic of surface waves is that their phase velocity is less than the velocity of light in vacuum due to the presence of the dielectric. The principal types of surface wave modes supported by a grounded dielectric are the transversal magnetic (TM_n) and transversal electric (TE_n) modes. The cutoff frequencies of these modes are given by 3.1 and 3.2, respectively, assuming that the grounded dielectric is infinitely extended in the y and z direction while the vacuum above the substrate is also unbounded (in x direction). Fig. 3.1 would be the case when MS is not present and all the lateral boundaries are shifted to infinity. h is the height of the dielectric and c is the velocity of light in vacuum.

$$f_n^{TM} = \frac{n \cdot c}{2h\sqrt{\epsilon_r - 1}} \quad n = 0, 1, 2, \dots \quad (3.1)$$

$$f_n^{TE} = \frac{(2n-1) \cdot c}{4h\sqrt{\epsilon_r - 1}} \quad n = 1, 2, 3, \dots \quad (3.2)$$

Any nonzero thickness ($h > 0$) dielectric slab with relative dielectric constant (ϵ_r) larger than unity must support at least one propagating TM mode, the TM_0 mode, which is the dominant mode of the dielectric slab waveguide with zero cutoff frequency. The guidance equation of the TM modes is given by 3.3, where k_d and k_{air} are the cutoff wave numbers in the two region of dielectric and air, respectively. The phase velocity of TM modes (β) is related to k_d and k_{air} by 3.4 and 3.5, respectively. Through some mathematical manipulations among 3.3, 3.4 and 3.5, k_d , k_{air} and β can be determined. The TM modes allow only E_z , E_x and H_y field components which can be calculated readily once the values of β are known.

$$k_d \tan k_d h = \epsilon_r k_{air} \quad (3.3)$$

$$k_d = \sqrt{\epsilon_r k_0^2 - \beta^2} \quad (3.4)$$

$$k_{air} = \sqrt{\beta^2 - k_0^2} \quad (3.5)$$

TE modes unlike TM modes support only nonzero cutoff frequencies. The guidance equation for TE modes is given by 3.6. The TE modes allow only H_z , H_x and E_y field components which can be calculated readily once the values of k_d and k_{air} are known. According to 3.1 and 3.2 the order of the propagation of the TM_n and TE_n surface wave modes are TM_0 , TE_1 , TM_1 , TE_2 , etc.

$$-k_d \cot k_d h = k_{air} \quad (3.6)$$

Now the structure of Fig. 3.1 is compared with the ideal case. This structure supports only two propagating surface wave modes, TM_0 and TE_1 ($f_1^{TE} = 100$ GHz) up to the frequency of 150 GHz. According to [42] the effective permittivity of the TM_0 mode starts to deviate from the value of 1.0 at the frequency (f_0) of 60 GHz, calculated by 3.7.

$$f_0 = \frac{c}{20h} \quad (3.7)$$

In addition to the presence of the MS line, the structure is bounded by magnetic walls in y and positive x directions. This introduces a nonzero cutoff for all modes except the MS one. TM_0 (m2, Fig. 3.2.b) rather starts at 20 GHz with $\epsilon_{r_effective}$ equal to 0.0. This dependency of cutoff frequency of TM_0 on the presence of the magnetic boundary in x direction is checked by varying the length of b_x (Fig. 3.4). It is obvious that shifting the magnetic wall far away from the dielectric can shift the cutoff frequency of the TM_0 mode at lower frequencies and support the dispersion frequency (f_0) given by 3.7.

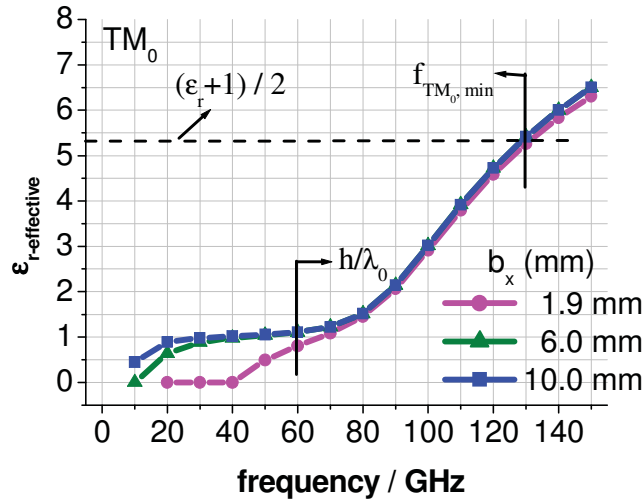


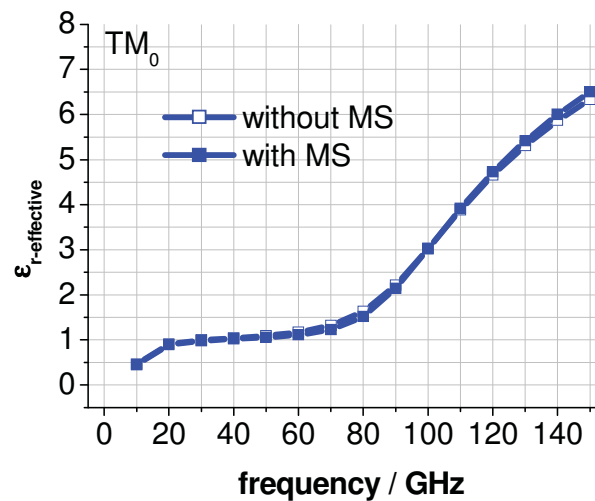
Fig. 3.4 Without PML : Dependence of the cutoff frequency of TM_0 mode on the distance of the magnetic boundary in x direction of Fig. 3.1 (i.e. b_x is varied). f_0 is 60 GHz and $f_{TM_0,min}$ is 130 GHz.

Again one has to consider that the guidance equation given by 3.3 for TM_0 mode is true only for unperturbed slab, e.g. if compared with Fig. 3.1, the MS line is not present and b_x extends to infinity. For the sake of clarity the structure of Fig. 3.1 is calculated and the effective dielectric constants for both the cases of with and without MS are listed in Fig. 3.5.a. The electric fields of TM_0 mode for the cases of with and without MS line are given in Fig. 3.5.b and 3.5.c, respectively, clearly showing that the E_x fields of the TM_0 mode are perturbed by the MS line. It is checked that the guidance equation of 3.3 is valid only for the without MS case if $\epsilon_{r_effective} \geq 1.0$. The difference in $\epsilon_{r_effective}$ values for both the cases varies between 1% and 8% with respect to the case with MS.

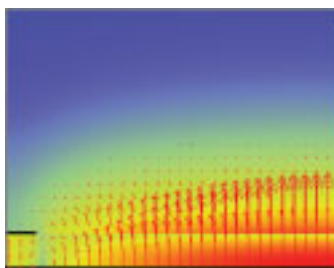
The TE_1 mode is supported by the structure of Fig. 3.1 as well. This mode is affected in two ways in this structure – presence of the MS line and the magnetic wall in the y direction. Due to the magnetic wall, the E_y component of the mode must vanish at the boundary. That's why the TE_1 (m6, Fig. 3.2.b) starts with $\epsilon_{r_effective}$ equal to 0.0 rather than 1.0 at 100 GHz. The guidance equation of 3.6 is fulfilled in the frequency range of 120 to 150 GHz where the values of $\epsilon_{r_effective}$ start to be larger than 1.0.

[41] suggests that in order to avoid any coupling between the surface wave modes and the MS mode, the upper frequency level should be kept below the frequency ($f_{TM_0,min}$ given by 3.8) where the $(\epsilon_r+1)/2$ line meets the TM_0 dispersion curve, as shown in Fig. 3.4.

a)



b) : TM_0 mode with MS



c) : TM_0 mode without MS

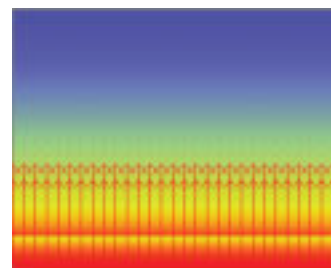


Fig. 3.5 Without PML: Influence of MS line on TM_0 mode. b_x of Fig. 3.1 is chosen to 10mm.

$$f_{TM_0,min} = \frac{c \cdot \tan^{-1}(\epsilon_r)}{\pi h \sqrt{2(\epsilon_r - 1)}} \quad (3.8)$$

Apart from the physical modes of MS, TM_0 and TE_1 , the other modes in Fig. 3.2 are due to the artificial magnetic boundaries and, therefore, are not of interest.

3.2 PML modes and their coupling to other modes

After knowing what type of physical modes and box modes can be supported by the structure of Fig. 3.1 it will be easier to detect the PML modes. Since we know now that same PML modes may be close to physical ones in the spectrum and not always easy to separate, one has to clarify whether and how they affect the behaviour of the physical modes in a 3D structure, i.e., the S-matrix of the physical modes. This is done in the following.

PML walls are used in such a way that PML cells are the largest ones. An overlapping PML wall is used at the crossing of X- and Y- PMLs in the investigations of this sub-chapter in order to stick to the basic PML definition [18], however it is found that XY non-overlapping PML walls show the same effects as the overlapping PML does. The nominal reflection coefficients used for the PML walls is -80dB .

PML modes are typified in general by their higher PPP values together with nonzero values of α and β . Again α values of PML modes are also large compared to the physical and box modes. How PML modes can be separated from the physical ones based on PPP criterion and α values are shown in [25]. However problems arise when sufficient amount of fields of physical modes are in the PML region. In this case, the PPP values are also very high for the physical modes and comparable to the PPP values of PML modes.

The MS structure (Fig. 3.1) is simulated with PML as mentioned above and the PML modes are filtered out according to their PPP and α values. The PPP, α and $\epsilon_{r_effective}$ values of the physical MS, TM_0 , TE_1 and box modes (m3 and m7) excited at port 1 are plotted in Fig. 3.6. The PPP of MS mode is nearly zero as most of the fields concentrate near the MS and almost no fields in the PML region. TM_0 mode has very high values of PPP at the lower frequencies and PPP decreases at higher frequencies. This is because, at lower frequencies the fields (E_x component) exist along the whole Y-PML region and at higher frequencies the fields concentrate near the dielectric. Nevertheless, a large portion of the fields are still in the Y PML region and that's why this mode is highly affected by PML. Even at 150 GHz this mode has a PPP value of above 0.4. If a PPP value of 0.4 is assumed to filter out the PML modes, the TM_0 mode will be filtered out as well. This means the effect of this physical mode on MS mode is neglected in the 3D calculation. It is also true for TE_1 mode and all box modes. For TE_1 mode the PPP varies from 0.9 to 0.03. Near the cutoff frequencies of these modes PPP values are the largest ones. Only modes of m3 and m7 are shown here because of their low PPP values and lower attenuation constants.

The physical as well as the box modes are also attenuated or amplified due to the PML, even though the structure is loss free. While α of the MS mode remains near to zero, α of TM_0 mode fluctuate between -25.0 to 50.0 . This mode is attenuated between 60 and 90 GHz and at other frequencies is amplified. TE_1 mode is also attenuated and the attenuation starts to decrease at 110 GHz from -160 to -36 at 150 GHz. Interestingly both TM_0 and TE_1 have a maximum attenuation constant at 80 and 110 GHz, respectively. The box modes of m3 and m7 are also highly attenuated.

The dispersion characteristics of the MS mode do not change when compared with the non-PML case. However the TM_0 mode now starts to propagate at lower frequencies with $\epsilon_{r_effective}$ values of 1.0 and remains at this value up to 60 GHz. Like TM_0 TE_1 mode also starts to

propagate with $\epsilon_{r_effective}$ values of 1.0 at 100 GHz. Because of very high α and low β values in comparison to some PML modes at cutoff frequencies the box modes remain at the lower end of the mode spectrum and do not appear if a definite number of modes (e.g. 10) are excited at the port. m3 and m7 are shown in Fig. 3.7.

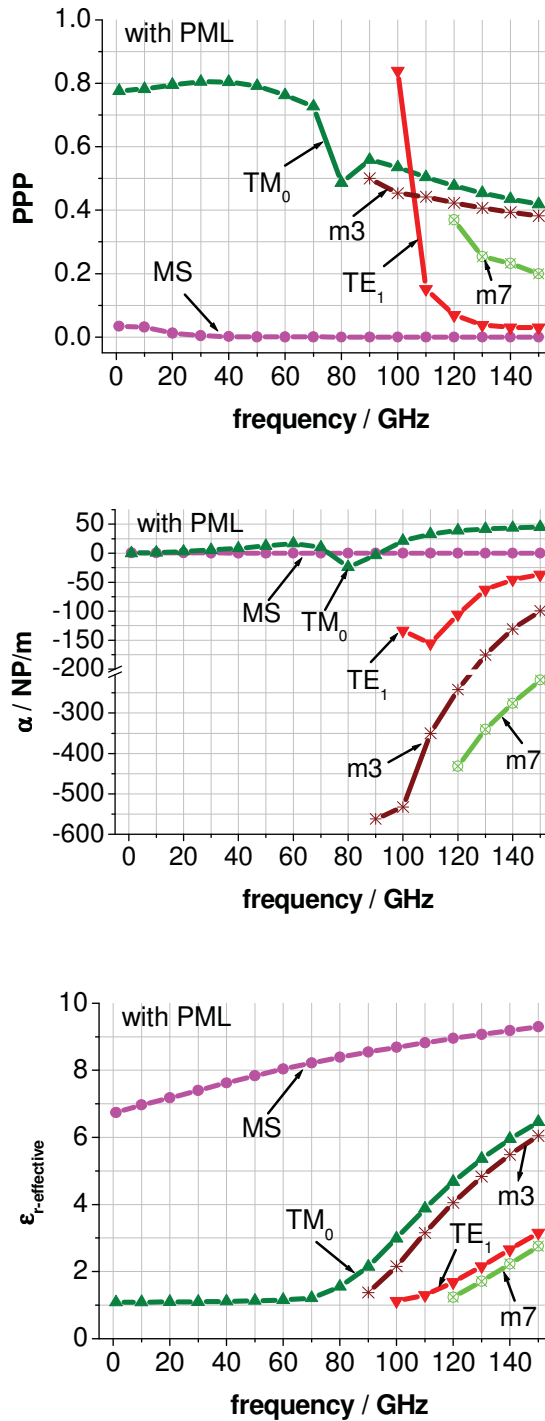
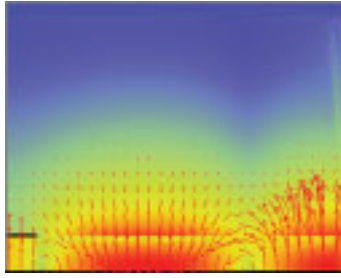


Fig. 3.6 With PML : PPP (top), attenuation constants (center) and effective relative dielectric constants (bottom) of the MS, TM_0 , TE_1 and box modes (m3 and m7 Fig. 3.2) at port 1 of Fig. 3.1 as a function of frequency. a_x , a_y , b_x and b_y are 950, 400, 1900 and 2400 μm , respectively.

m3 (box mode)



m7 (box mode)

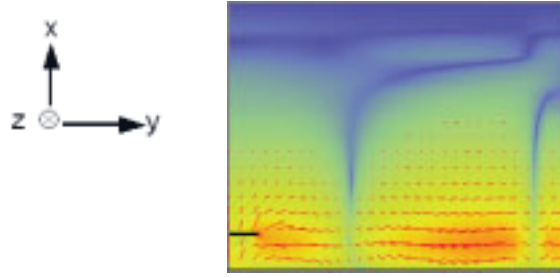


Fig. 3.7 With overlapping PML : mode spectrums of box modes (m3 and m7, Fig. 3.2) of particular interest in port 1 of Fig. 3.1 at 150 GHz. a_x , a_y , b_x and b_y are 950, 400, 1900 and 2400 μm , respectively.

Up to this point, all the results and discussion have been done for the port 1 of Fig. 3.1. The same is also true for the port 2 of Fig. 3.1. Now a 3D simulation is carried out while allowing 10 modes at each port and the coupling of MS mode to all other modes will be checked. In Tab. 3.1 these couplings between the MS mode and other modes at port 1 of Fig. 3.1 are listed together with α , β and PPP values at 50 and 150 GHz for example.

modes	type	$\epsilon_{r\text{-eff}}$	50 GHz			coupling to MS (dB)	type	$\epsilon_{r\text{-eff}}$	150 GHz		
			α (Np/m)	PPP					α (Np/m)	PPP	coupling to MS (dB)
1	MS	7.83	0.06	0.0	-17	MS	9.29	0.0	0.0	-21	
2	TM_0	1.12	12.41	0.79	-38	TE_1	3.15	-36.87	0.03	-26	
3	PML	1.46	-52.00	0.86	-41	TM_0	6.45	45.25	0.41	-47	
4	PML	1.78	-177.99	0.81	-40	m3	6.04	-99.46	0.38	-42	
5	PML	1.34	-522.74	0.91	-46	PML	1.01	-179.77	0.79	-48	
6	PML	0.98	-524.11	0.80	-42	PML	0.84	-198.05	0.71	-54	
7	PML	5.83	-554.26	0.76	-64	m7	0.75	-218.14	0.20	-28	
8	PML	1.30	-564.36	0.68	-53	PML	0.87	-309.31	0.78	-46	
9	PML	6.09	-574.61	0.61	-78	PML	1.43	-452.45	0.96	-60	
10	PML	6.17	-576.65	0.75	-69	m4	4.94	-489.07	0.40	-45	

Tab. 3.1 Coupling between the MS mode (numbered 1) and all other modes (numbered 2 to 10) for 50 and 150 GHz at port 1 of Fig. 3.1 are listed. Type, effective dielectric constant ($\epsilon_{r\text{-eff}}$), attenuation (α), PPP values of each mode are also given for completeness.

At 50 GHz the reflection of MS is -17 dB as the characteristic impedances of the two lines are 50 and 70 Ω respectively. At this frequency, except for the MS and TM_0 mode, all are PML modes and these PML modes are clarified by their high PPP and α values. The couplings between MS and PML modes are very low (< -41 dB). Obviously the coupling between the MS and TM_0 mode is also very low (-38 dB). At 150 GHz, on the other hand, TE_1 and box modes are also present. The couplings between the PML modes and MS mode are again very low (< 42 dB). The TM_0 mode shows also very low coupling (-47 dB) at 150 GHz. TE_1 and m7 show relatively high coupling of -26 dB and -28 dB, respectively. This is because the fields of these two modes look very identical and concentrate with a large

amount near the MS (see Fig. 3.3 and 3.7). The reflection coefficient of the MS line at this frequency is -21dB .

The coupling of the MS mode at port 2 to other modes at port 2 shows similar behaviour as summarised in Tab. 3.1, not only for 50 and 150 GHz – coupling of PML modes to MS mode remains very low ($< -40\text{dB}$) at all frequencies. As TE_1 and $m7$ shows relatively stronger coupling (above 130 GHz) to the MS mode, one must carefully decide whether to neglect or not neglect these modes by removing them through the PPP criterion.

Up to 130 GHz PPP turns out to be a very good criterion to remove PML modes and TM_0 mode which have very low coupling to the MS mode for this structure. As the appearance of surface modes and box modes depends on the structure itself and its boundary, one needs a training of 2D (with the help of PPP) and 3D simulation (with the help of coupling) in order to remove unnecessary modes from the calculation domain.

As in the case of TM_0 mode where most of the fields are in the PML region and thereby strongly affected by the PML (attenuated or amplified), the fields of MS strip mode should be concentrated in the non-PML region. Fig. 3.8 shows that if the PML walls are placed very near to the MS structure, the MS fields exist in the PML region and the MS mode is highly attenuated or amplified. This raises the question of how far the PML walls should be placed, particularly for planar structures like MS and CPW line. It is found that a distance of 5 times the maximum between substrate thickness and MS width from the MS as well CPW lines is a good thumb rule to place the PML walls and thereby to minimize the effect of PML.

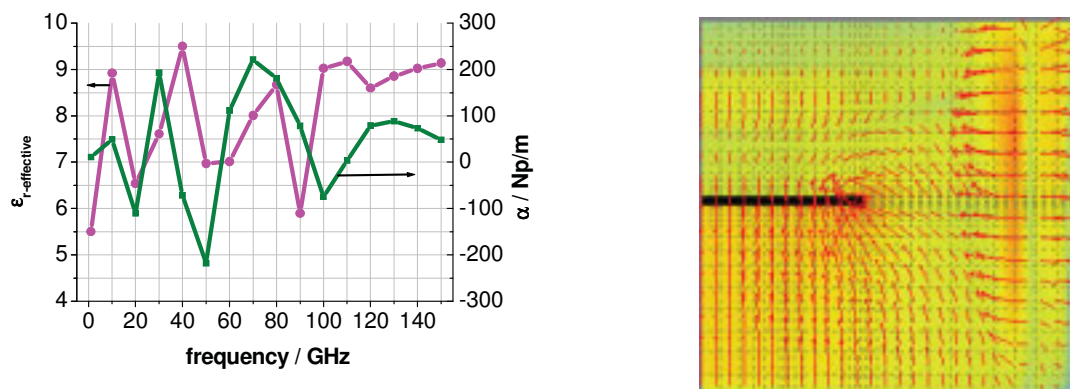


Fig. 3.8 With PML: effective dielectric constants and attenuations of MS mode (a) at port 1 of Fig. 3.1 as a function of frequency. a_x , a_y , b_x and b_y are 150, 150, 500 and 500 μm , respectively. The corresponding MS mode spectrum (b) at 50 GHz.

3.3 Conclusion

It was shown that the FDFD simulation with PML in general gives rise to artificial PML modes at the waveguide ports. These PML modes may appear close to the physical modes in the spectrum but were found to show very low coupling to the physical modes of interest (e.g. MS, CPW, PPL etc.).

The MS or CPW modes, whose most fields particularly concentrate in the non-PML region, are not affected by the PML, if PML walls are sufficiently far away (five times the maximum between substrate height and strip width). The surface wave modes as well as box modes may be highly affected by the PML.

The so-called PPP criterion defined as the power part of a particular mode in the PML region is useful to filter out PML modes but its intent parameters may differ from structure to structure. A careful observation following the 2D (using PPP criterion) and 3D simulations (checking the coupling of unwanted PML, box and physical modes for couple of first simulation run) is needed in order to remove unnecessary modes from the calculation domain. In case of doubt, a mode should be included in order to maintain best accuracy. Since the influence of PML modes on physical ones is found to be low, the resulting possible errors are small.

4 Internal Ports

The objective of this chapter is to describe how internal ports can be implemented in the FDFD method. In chapter 1, it was shown that the internal ports can be realized in general in terms of a relaxation current source or a conduction current source. It will be shown here that the relaxation current excitation in FDFD method does not provide physical solution. As is known, the conduction current internal ports possess parasitic inductances. It will be shown how the values of the parasitic inductances can be estimated for deembedding.

Internal ports make the way of exciting any structure from any position inside the structure. It becomes very much inefficient for an EM simulator if an MMIC together with its housing (mother board/package) is tried to be simulated. As the dimensions of the lumped and active devices in MMICs are very much small compared to the passive elements, the EM simulators need a very large mesh size to put all the circuit elements together. Internal ports provide one solution for this problem. The tiny circuit components (lumped elements, active elements) can be replaced by internal ports and the resulting current/voltage relationship (e.g. S- or Z-parameters) found at the internal ports through the EM simulations can be used in network simulators in order to interface with the replaced components. This way with the help of internal ports the complex MMIC structures along with their housing can be simulated easily part by part, e.g. passive package and the active components separately, and then the parts can be interfaced in the network simulators.

As an example, Fig. 4.1.a shows the array of a 2 GHz power transistor. The transistor fingers are fed by the MS waveguide feeding lines (not shown here) through bond wires. During the design of the device, it is interesting for the circuit simulators to know the S-parameters at the points where the bond wires are connected with the transistor fingers. This is not possible without local excitations at those points. Again the simulation of the structure as a whole is cumbersome and inefficient for EM simulators. As a remedy the transistor array is taken out of the structure by inserting internal ports at the transistor fingers. The structure without the transistor array can be simulated with waveguide ports at the feeding lines and internal ports at the transistor fingers. The resulting S-parameters can be used to interface with the transistor array in network simulators. As shown in Fig. 4.1.b, the internal ports are placed at the feeding lines for the bond wires and the resulting voltage and currents are calculated to obtain the resulting S-parameters.

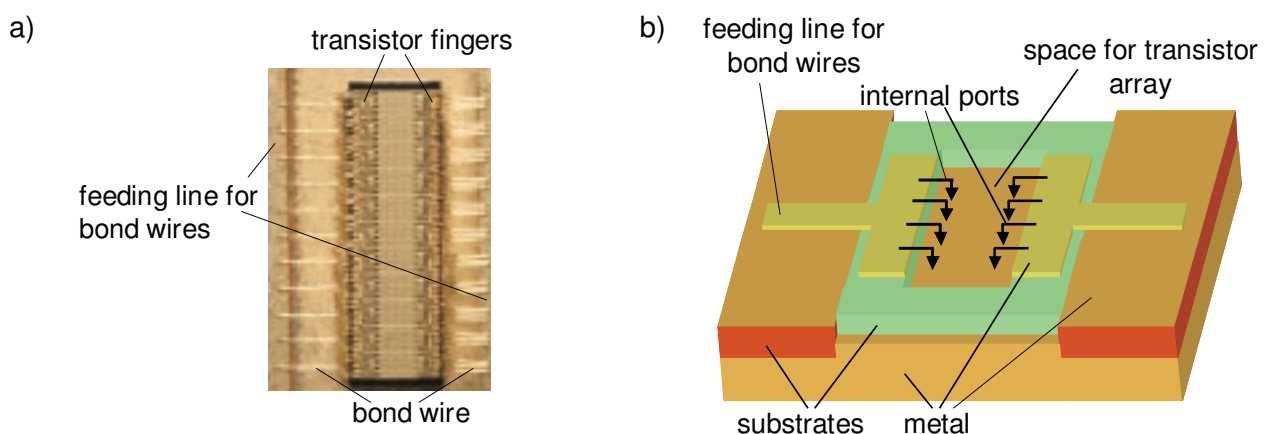


Fig. 4.1 Power transistor array (a). Simulation structure for the power transistor's housing (b).

4.1 Relaxation Current Internal Port

The relaxation current internal port is realized by inserting two time varying charges of equal magnitudes but opposite polarities at two nodes of two conductors which are part of a certain circuitry. In this way a time varying current is defined to enter and come out of the circuitry at those two nodes. The basic definition of this type of internal port excitation shown in Fig. 1.6 is repeated here (Fig. 4.2)

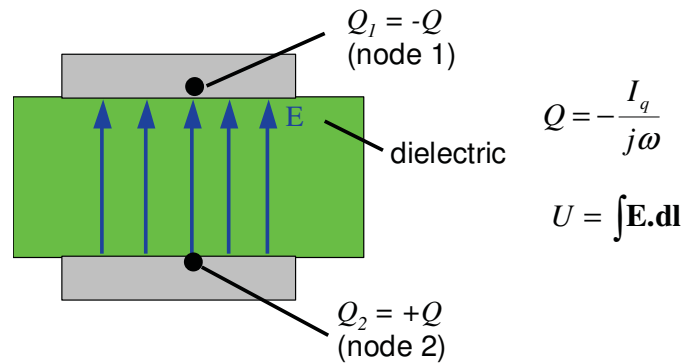


Fig. 4.2 Relaxation current internal port : voltage source. $q_v \neq 0$, $J_e = 0$.

The implementation of the relaxation current internal port procedure in FDFD method is given in Appendix 7.2. The FDFD method deals with a discretized wave equation given by 4.1. Equation 4.1 is solved for the vector \vec{e} which contains all the electric field components of each cell of the FDFD mesh. M_1 , M_2 and M_3 are the matrices that contain the information on material properties and dimensions of the structure under consideration. M_1 matrix is defined to correspond to the $\nabla \times \nabla \times$ operator, on the other hand M_3 is defined to correspond the $(\nabla \nabla \cdot)$ operator. Vector \vec{r}_r refers to the relaxation current internal port source (in terms of time varying charges) and is related to matrix M_3 by 4.2. M_3 is brought to the equation 4.1 in order to eliminate static charges inside the computational domain and thereby to improve convergence [6, 7].

$$M \vec{e} = (M_1 + M_2 + M_3) \vec{e} = \vec{r}_r \quad (4.1)$$

where,

$$M_1 \equiv M_1(\epsilon, \mu, \kappa, d) \equiv \nabla \times \nabla \times,$$

$$M_2 \equiv M_2(\epsilon, \kappa, d, \omega) \text{ and}$$

$$M_3 \equiv M_3(\epsilon, \mu, \kappa, d) \equiv \nabla \nabla \cdot$$

$$M_3 \vec{e} = \vec{r}_r \quad (4.2)$$

In a homogeneous material, 4.1 is the discretized representation of the Helmholtz's equation as given below by 4.3.

$$\Delta \vec{E} + k^2 \vec{E} = \vec{r} \quad (4.3)$$

Because the FD formulation allows for a one-to-one correlation with the vector differential equation, the following considerations will be based on the latter one (see also [8]).

4.2 can be written as

$$\nabla \times \nabla \times \vec{E} - \nabla \nabla \cdot \vec{E} - k^2 \vec{E} = \vec{r} \quad (4.4)$$

Thus, the homogeneous equation (with $\vec{r} = 0$) has two types of solutions, one with $\nabla \times \vec{E} \neq 0$ and $\nabla \cdot \vec{E} = 0$, the other with $\nabla \times \vec{E} = 0$ and $\nabla \cdot \vec{E} \neq 0$. The first refers to the electrodynamic but divergence-free (and thus charge-free) E-field. The other refers to a non-physical field, which involves $\nabla \cdot \vec{E} \neq 0$ and thus space charges.

If the excitation fields, i.e., \vec{r} in 4.3 and 4.4, are divergence-free, the non-physical fields are not excited and thus zero. Using a time-varying charge, however, as done in the excitation current version, $\nabla \cdot \vec{E} \neq 0$ holds and thus the resulting solution for \vec{E} is a mixture of physical and non-physical fields and thus useless for the intended EM simulation purpose.

In the FD formulation, $\nabla \cdot (\epsilon \vec{E})$ refers to $M_3 \vec{e}$ and one has in analogy to 4.4 two types of solutions for 4.1. The physical one with $M_3 \vec{e} = 0$ and $M_1 \vec{e} \neq 0$, and the non-physical one with $M_3 \vec{e} \neq 0$ and $M_1 \vec{e} = 0$.

Thus, introducing a relaxation current source, i.e. time varying input charges, the resulting solution of equation 4.1 will comprise solutions with $M_1 \vec{e} = 0$ and $M_3 \vec{e} \neq 0$ and thereby lead to non-physical solutions. This non-physical solution makes the excitation of a structure by relaxation current sources non-feasible.

The non-feasibility of the relaxation current internal port source is explained using an example of the structure given in Fig. 4.3. In a cube of magnetic walls filled with air two identical copper lines are defined. At the points of A_3 and B_3 the two nodes of a relaxation current internal port are defined, where a time varying positive charge Q and a negative charge $-Q$ are applied at node A_3 and B_3 respectively. The magnitudes of the charges are calculated by means of equation 7.9 for 1 Amp current at 1GHz.

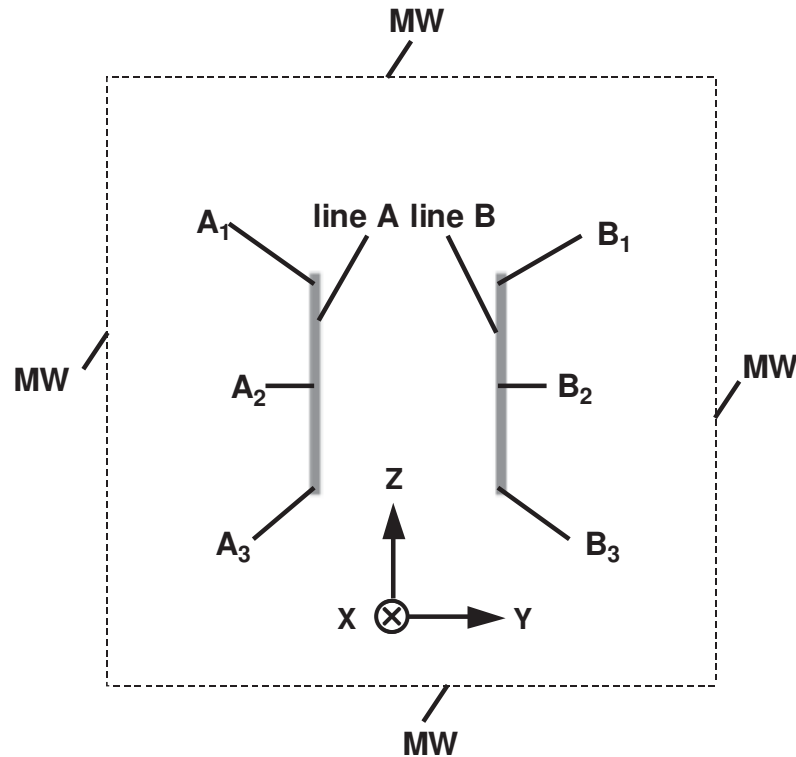


Fig. 4.3 Two identical copper ($\sigma = 5.6e7$) lines (line A and B) are contained in a cube of magnetic walls (MW). The sides of the MW cube are $150 \mu\text{m}$. The length (l), width and thickness of each line are 50 , 4 and $2 \mu\text{m}$. The lines are $40 \mu\text{m}$ apart from each other. A_1 , A_2 , A_3 and B_1 , B_2 , B_3 are some points of interest inside the line A and B respectively. The cell sizes inside the lines are less than one fourth of skin depth. At point A_3 a positive time varying charge $+Q$ ($1.59169E-10$ C) and at point B_3 a negative time varying charge $-Q$ ($-1.59169E-10$ C) are applied. The wave length (λ) at 1 GHz for this line system is 0.28m .

After the 3D solution of equation 4.1, the charges at each cell are calculated. The charge distribution at each cell normalized by the maximum charge amplitude on the $x = 70 \mu\text{m}$ plane is shown in Fig. 4.4. It is found that the total amount of charge inside the cube is zero. The dual cells which contain the points A_3 and B_3 possess the same amount of charges with the same polarities of the input charges. In line A, the same amount of input charges (Q) but negative in polarity is inserted by the solution, decreasing from the surrounding cells of A_3 towards the end of the line. In the same way, in line B, a positive charge of Q is distributed by the system decreasing from the surrounding cells of B_3 towards the end of the line. This suggests that the solution tries to oppose the insertion of time varying charges by distributing the same amount of charges with opposite polarities. If one end of a two conductors line system is connected to current source of 1 Amp and the other end is open, the current decreases linearly along the line (assuming $l \ll \lambda$) and ends with zero at the open end of the line system. In case of the example of Fig. 4.3, the charges and currents along the line A (or B) are shown in Fig. 4.5. Obviously this does not show a physical behaviour of current for such a transmission line system. Even though the input current is 1 Amp, along the line the current is almost negligible. This implies that the solution provides non-physical charge as well as field distribution.

The 2D and 3D electric field distribution on the plane of $x = 70 \mu\text{m}$, are given in Fig. 4.6 and 4.7 respectively. Because of positive and negative input charges, we see at point A_3 and B_3 the electric fields coming out off and going into the charges respectively. We also see the presence of negative charges along the line (e.g. points A_2 , A_1 etc.) where the fields go into the charges. Same way along the line B there are positive charges, so that electric fields are coming out off these charges. The strength of the fields is also decreasing along the line. All of these provide non-physical behaviour of the solution of equation 4.1 which suggests that such a relaxation current internal port excitation is not feasible.

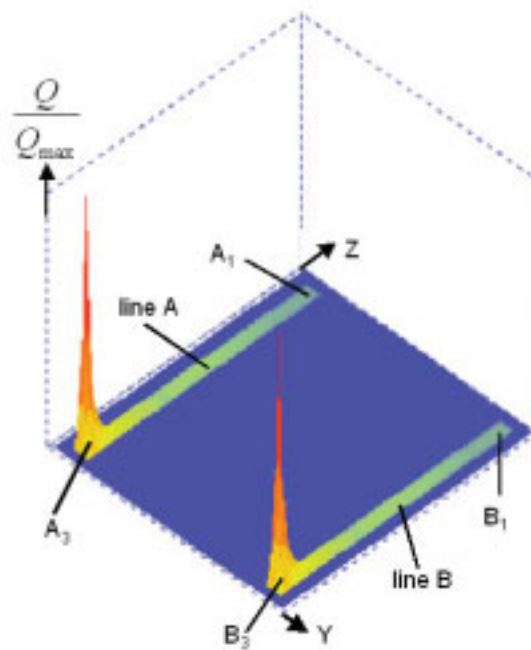


Fig. 4.4 3D view of charge distribution on the center plane in x direction ($x=70 \mu\text{m}$).

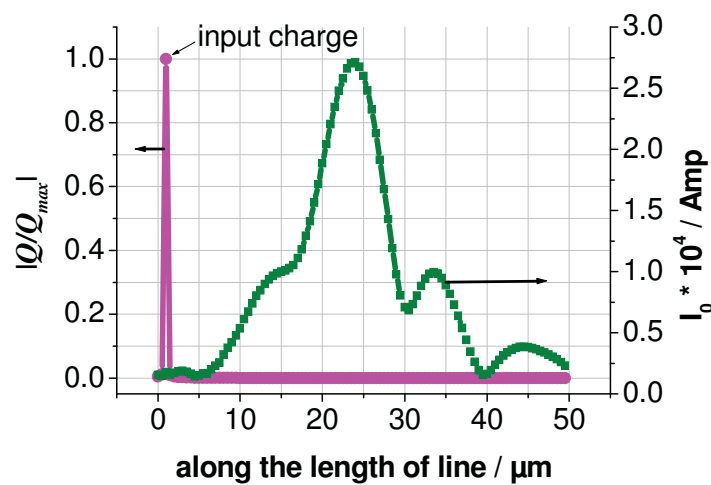


Fig. 4.5 Current (I_0) and charge distribution (Q) along the line A. The same is true for line B as well. $Q_{max} = 1.59169\text{E-}10 \text{ C}$.

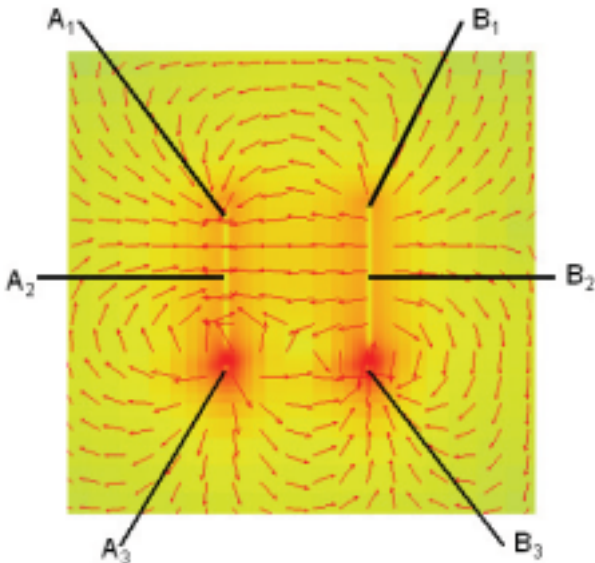


Fig. 4.6 2D electric field distribution on the center plane in x direction ($x=70 \mu\text{m}$).

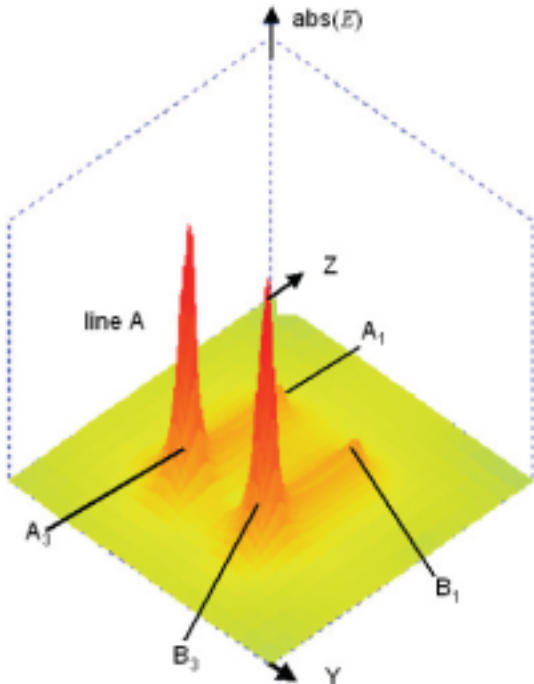


Fig. 4.7 3D electric field distribution on the center plane in x direction ($x=70 \mu\text{m}$).

4.2 Conduction Current Internal Port (Line Current)

The conduction current internal port is realized in FDFD method by defining a path along the edges of cells between two conductive structures. The path can be chosen arbitrarily. However, in order to obtain useful results the path length should be small compared to the wavelength in order to have a well-defined voltage port. Along this path, a finite line current (I_0) is defined. The basic definition of this type of excitation shown in Fig. 1.5 is repeated here (Fig. 4.8) and the implementation in FDFD method is given in Appendix 7.3. Assuming no sources other than a conduction current source inside the structure, equation 4.1 looks like as given below by 4.5. Here vector \vec{r}_c stands for the conduction current source. The M_1 , M_2 and M_3 matrices are defined to contain information on material properties and dimensions as stated in the previous chapter. The relation between \vec{r}_c and the matrices are given by 4.6 and 4.7. Unlike the relaxation current source, here the excited field is divergence free (i.e. $\nabla(\epsilon E) = 0$). So when 4.5 is solved for \vec{e} , the vector that contains the electric field components at each cell, it does not result in any non-physical solution.

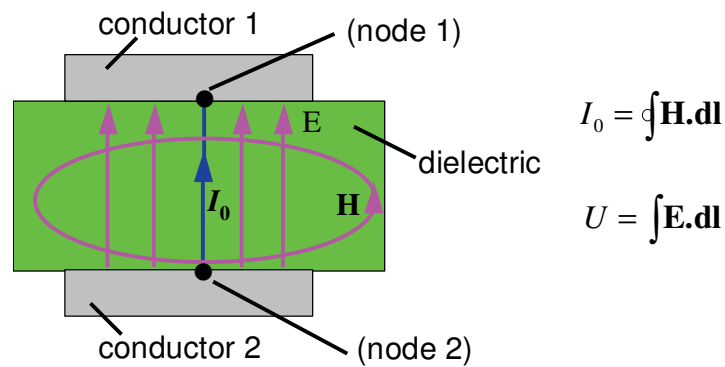


Fig. 4.8 Conduction current internal port : line current source. $q_v = 0$, $J_e \neq 0$.

$$M \vec{e} = (M_1 + M_2 + M_3) \vec{e} = \vec{r}_c \quad (4.5)$$

where,

$$M_1 \equiv M_1(\epsilon, \mu, \kappa, d) \equiv \nabla \times \nabla \times,$$

$$M_2 \equiv M_2(\epsilon, \kappa, d, \omega) \text{ and}$$

$$M_3 \equiv M_3(\epsilon, \mu, \kappa, d) \equiv \nabla \nabla \cdot$$

$$(M_1 + M_2) \vec{e} = \vec{r}_c \quad (4.6)$$

$$M_3 \vec{e} = 0 \quad (4.7)$$

The simple MS structure of Fig. 4.9 is used here to check the feasibility of this excitation procedure. Two internal ports with currents I_{01} and I_{02} are used to feed the structure. As two internal ports are used, the structure must be excited twice in order to get the complete voltage/current relationship at the nodes of the ports. Tab. 4.1 shows the values of I_{01} and I_{02} as an example for the excitations.

Excitation	I_{01} / Amp	I_{02} / Amp
1	1	1
2	1	-1
3	1	0

Tab. 4.1 Values of I_{01} and I_{02} to feed the structure of Fig. 4.9.

For all of these excitations the currents along the MS line (I_{MS}) are calculated at 1GHz and shown in Fig. 4.10. For the first excitation, both I_{01} and I_{02} are assigned with 1 Amp and both of them flow in the same direction (i.e. toward the strip). In this case $|I_{MS}|$ must be equal to 1 Amp at the two ends of the line and linearly decrease to zero at the middle of the line. For the second excitation I_{01} and I_{02} are assigned with 1 Amp and -1 Amp. In this case both the currents are in opposite direction - a steady 1 Amp current must flow along the line. For the third excitation, the MS is fed by 1 Amp at one end and open at the other end. So the current must decrease linearly from 1 Amp to zero along the line. All these behaviours are physical for any line system which is fed by current sources at the two end of the line. Here it should be noted that, the linear behaviours of the currents in Fig. 4.10 are due to the very small line length compared to wavelength ($l \ll \lambda$), otherwise they are not linear along the line, rather sinusoidal because of standing wave pattern.

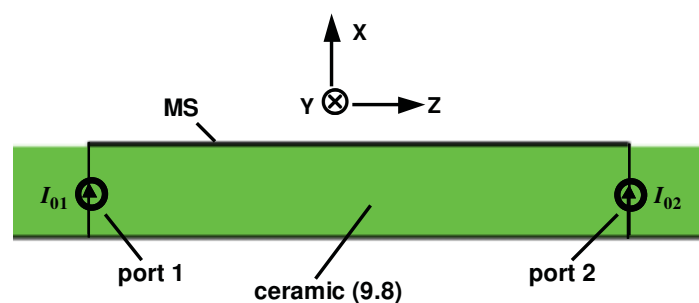


Fig. 4.9 PEC MS on ceramic ($\epsilon_r = 9.8$) substrate. The length (l), width and height of the strip are $1600\mu\text{m}$, $30\mu\text{m}$ and $5\mu\text{m}$ respectively. The substrate is $100\mu\text{m}$ thick. At the two ends of the MS, two conduction current internal ports are inserted. Port 1 and 2 feed the line with currents I_{01} and I_{02} respectively. The wavelength (λ) at 1 GHz for this line system is 0.12 m .

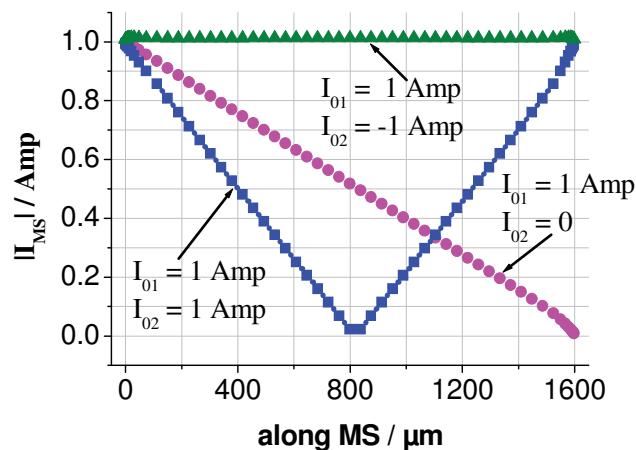


Fig. 4.10 Currents along the MS line in Fig. 4.9 for the three different excitations according to Tab 4.1.

With any two of the excitations of Tab. 4.1, for example, the Z-matrix at the two ports of the MS line can be calculated. The formulas to calculate Z-matrix for this conduction current source procedure is given in Appendix 7.4. If the reference impedances of the internal ports are specified, then the S-parameters of the line can be calculated. In order to provide a matched condition at the ports, the characteristic impedance of the MS line at each frequency is taken as the reference impedances of the ports. In this case there should not be any reflection at the internal ports. Accordingly, one expects high return loss at the two ports. As can be seen from Fig. 4.11, however, considerable reflection occurs. This can be partly explained by the fringing fields at the ends of the line, which cause an extra capacitance. Since also an inductance is found at the end, this must be due to the source. This parasitic inductance will be addressed in the next section.

Deembedding the L and C, one has the line characteristics only. Since the structure is symmetric at the middle of the line, the Z- and S-parameters are also symmetric at the two ports. The reflection coefficients at port 1 are shown in Fig. 4.11 for both the cases of with and without deembedding of parasitic effects. Without deembedding, the reflection is very large: > -25 dB above 25 GHz up to -15 dB at 40 GHz. This high reflection is solely due to the parasitics as mentioned above. As the port impedances are assumed to be matched with the MS line impedance, the very small parasitics become dominant enough to influence the MS line characteristic. It is clear that with an LC deembedding the reflection goes below -50 dB and the minima at half wave length (i.e. 37 GHz) become prominent. We see that there is a significant phase shift at higher frequencies between the cases of with and without deembedding (e.g. 22° at 50 GHz).

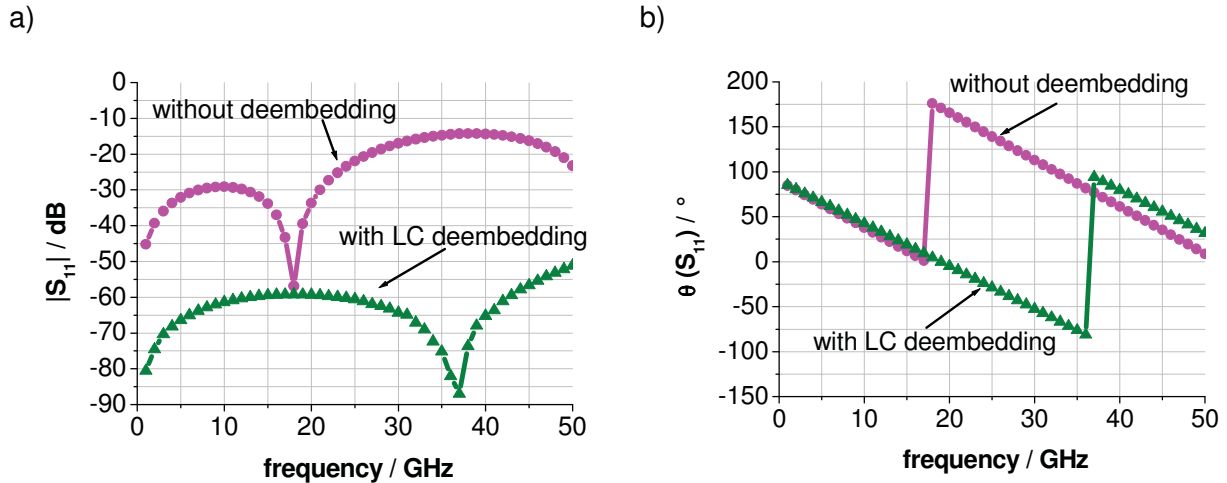


Fig. 4.11 Reflection coefficient (a) and the corresponding phase (b) at port 1 of MS line in Fig. 4.9. The line impedance at each frequency is taken as the port reference impedance. LC deembedding with $L = 82$ pH and $C = 3$ fF.

4.3 Parasitic Effects of Conduction Current Internal Ports

As mentioned before, the conduction current internal port possesses parasitic inductance. The fringing fields at the ends/edges of the transmission line/metal plate, on the other hand, result in a parasitic capacitance. Whenever these parasitic inductance and capacitance are known they can be deembedded. The deembedding formulas are given in Appendix 7.5. A numerical procedure is developed to extract the parasitic inductance and capacitance and a look-up table is made for the inductance as a function of internal port length and internal port cell sizes.

The extraction of internal port parasitic inductance (L_{ex}) and the end capacitance (C_{end}) is described with the help of the circuit model given in Fig. 4.12. Any transmission line, e.g. MS of Fig. 4.9, fed by two identical internal ports at the end of the line can be defined according to this model. L_{ex} can be extracted from Z_{ex} by 4.8 and 4.9, where Z_{FDFD} is the Z-matrix of the EM-simulated structure including the parasitics, Z_{line} is the Z-matrix of the line without parasitics and Y_c is the admittance matrix describing the end effect.

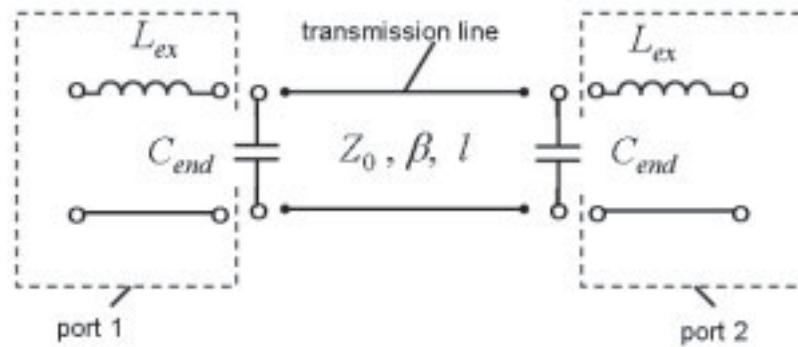


Fig. 4.12 Two identical internal ports are connected at the ends of the transmission line. The transmission line is defined by characteristic impedance Z_0 , phase constant β and length l . L_{ex} stands for the parasitic inductance of the ports, where as C_{end} represents the end effects of the line.

$$Z_{ex} = Z_{FDFD} - (Y_{line} + Y_C)^{-1} \quad (4.8)$$

where,

$$Y_{line} = Z_{line}^{-1} = \begin{pmatrix} -jZ_0 \cot \beta l & -jZ_0 \operatorname{cosec} \beta l \\ -jZ_0 \sec \beta l & -jZ_0 \cot \beta l \end{pmatrix}^{-1} \quad \text{and} \quad Y_C = \begin{pmatrix} j\omega C_{end} & 0 \\ 0 & j\omega C_{end} \end{pmatrix}$$

$$Z_{ex} = \begin{pmatrix} j\omega L_{ex} & 0 \\ 0 & j\omega L_{ex} \end{pmatrix} \quad (4.9)$$

In [41] it is shown how the end capacitance can be calculated graphically. C_{end} is in the fF range and graphical extraction of C_{end} may lead to an inaccuracy in L_{ex} extraction. Here C_{end} is extracted in an alternative way. A waveguide port is inserted at the center of the line in the longitudinal direction and the reflection coefficient (S_{11}) at the waveguide port is calculated through the FDFD EM simulation. C_{end} is then calculated from S_{11} by 4.10. The extraction of C_{end} of the MS line in Fig. 4.9 is explained in Fig. 4.13 as an example, where it is assumed that in both cases the discretizations are the same.

$$C_{end} = -\frac{r-1}{j\omega Z_0} \frac{r+1}{r+1} \quad (4.10)$$

where,

$$r = e^{j\phi_{open}} \quad \text{and} \quad \phi_{open} = \arccos |S_{11}| + 2\beta l$$

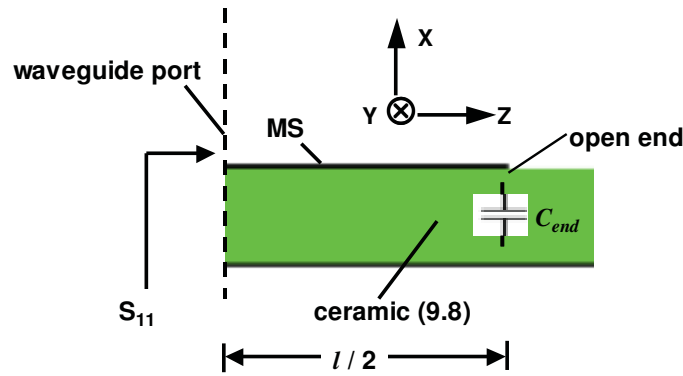


Fig. 4.13 Extraction of C_{end} by inserting an waveguide port at the center of the MS line of Fig. 4.9. The discretization schemes of both the (half and full) structures are kept the same.

The values of C_{end} for the half MS structure of Fig. 4.13 and thereby the values of L_{ex} for the full structure of Fig. 4.9 are listed in Fig. 4.14 for different substrate thicknesses (h). As the internal ports are connected between the ground and MS, the lengths of the internal ports are same as the substrate thicknesses. An increase in substrate thickness means an increase in fringing fields and thereby an increase in end capacitance. For increasing substrate thickness the non-quasi-static effects start earlier in terms of frequency. For 30 μm substrate thickness, C_{end} is almost constant up to 50 GHz, whether for 200 μm substrate thickness, C_{end} starts to deviate from the constant value already at 10 GHz.

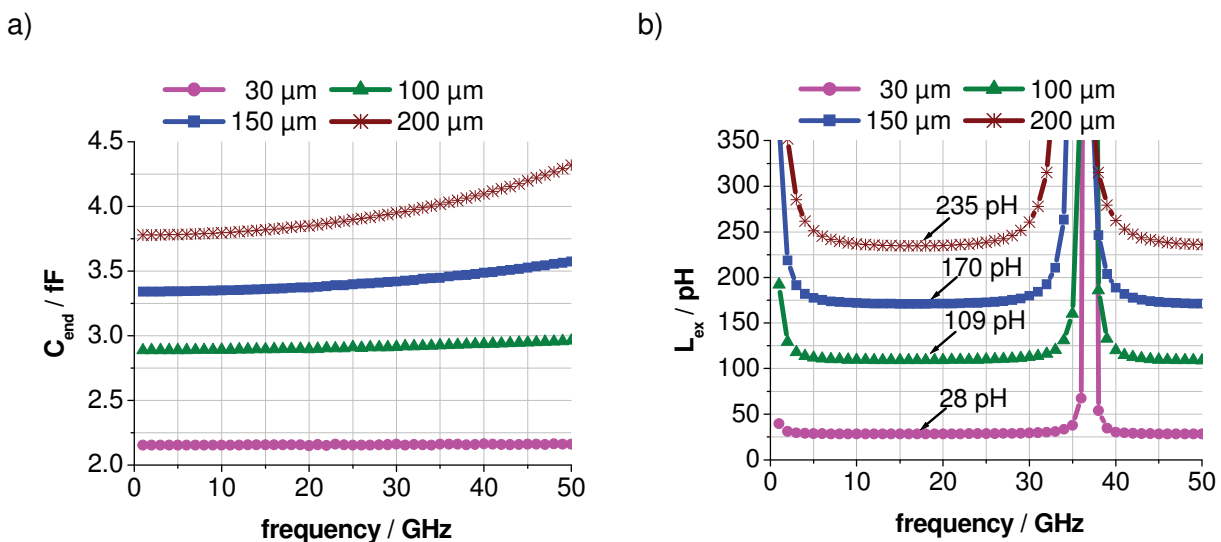


Fig. 4.14 C_{end} (a) and L_{ex} (b) for different substrate thicknesses (i.e. length of the internal port) according to Fig. 4.9 and 4.13, respectively. The internal port cell sizes in y direction (ΔY) and z direction (ΔZ) along the path of the internal port are kept 1 μm .

At the frequencies corresponding to multiples of half wave length, the difference in the sampled values of the standing wave pattern in the neighbouring cells becomes smaller than the numerical errors, which results in very large non-physical values. In case of L_{ex} we see that near zero and 37 GHz such very large inductance values. Considering the values where L_{ex} remains constant with frequency, we see that L_{ex} increases linearly with the length of the internal port (i.e. thickness of the substrate) – ranging from 28 pH for 30 μm length to 235 pH for 200 μm length. The values of L_{ex} suggest that by reducing the substrate thickness and thus the length of the internal port, one can reduce the parasitic effects already significantly.

It is found that L_{ex} is very much sensitive to the cross section of the internal port cells in the perpendicular direction to the path of the internal port. For the MS example of Fig. 4.9, the internal port path is directed in x direction, the internal port cell sizes in y direction (ΔY) and in z direction (ΔZ) comprise the cross section. For the results shown in Fig. 4.11, the values of ΔY and ΔZ were 3.75 μm whereas for the results in Fig. 4.14 the values of ΔY and ΔZ were 1 μm . The extraction of L_{ex} has been carried out while varying ΔY , ΔZ and substrate thickness for the above mentioned MS structure.

4.4 Analytical Formulation for the Parasitic Inductance

Since one can not perform the various simulations in order to extract the parasitic inductance L_{ex} for each structure under consideration, it would be desirable to have an analytical approximation. This is presented in the following, starting from the work in [26, 27].

According to [26-29], the inductance of a wire (L_{hm}) with rectangular cross section $A (= a \times b)$ results in an inductance given by 4.11, assuming that the wire possesses homogeneous current density over the cross section. In the FDFD procedure, the assignment of an input current of internal port is equivalent to a current density, distributed evenly over the dual cell surface as shown in Fig. 4.15. So the internal port can be thought of as a rectangular wire with a homogeneous current density over the cross section which is same as the cross section of the dual cell. Of course, in contrast to a conductive wire, we do not have a condition on the tangential E-field.

$$L_{hm} = \frac{\mu_0}{2\pi} l \left(\ln \frac{4l}{a+b} - \frac{1}{3} \ln 2 - \frac{\pi}{3} + \frac{13}{12} \right) \quad (4.11)$$

Thus, replacing a and b in 4.11 by the respective cell sizes ($a = \frac{\Delta X}{2} + \frac{\Delta X}{2}$; $b = \frac{\Delta Y}{2} + \frac{\Delta Y}{2}$ for equidistant mesh) one obtains an analytical approximation for L_{ex} given by 4.12. For the example in Fig. 4.9: $\Delta X \rightarrow \Delta Y$ and $\Delta Y \rightarrow \Delta Z$, respectively.

$$L_{hm} = \frac{\mu_0}{2\pi} l \left(\ln \frac{4l}{\Delta X + \Delta Y} - \frac{1}{3} \ln 2 - \frac{\pi}{3} + \frac{13}{12} \right) \quad (4.12)$$

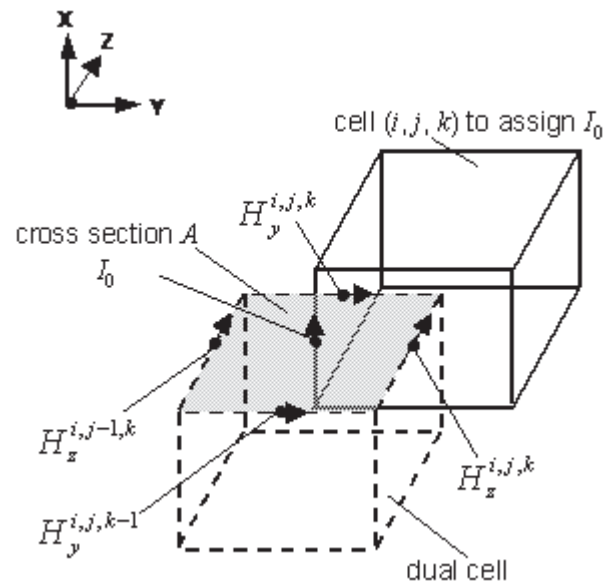


Fig. 4.15 Formally, the current I_0 is assigned at the center of an edge along the current path. In the FDFD formulation this current can be described to be distributed with a homogeneous current density over the cross section A . In this example, the current path is assumed to be in the x direction. The magnetic fields are defined at the center of the edges of A . See Appendix for 7.1 for FDFD discretization.

The values of L_{hm} (calculated according to 4.12) are compared with L_{ex} (extracted from the simulations) in Fig. 4.16 corresponding to the internal ports of Fig. 4.9. The internal port lengths (h) are varied to 30, 100, 150 and 200 μm . Two different cross-sections of internal port are considered – $1\mu\text{m} \times 1\mu\text{m}$ and $7.5\mu\text{m} \times 7.5\mu\text{m}$. In all cases there is a linear behaviour of inductance in relation with the port length and the two definitions provide the same inductance values. The smaller cross sections result in higher inductances – e.g. in the case of 200 μm length the inductances are 227 and 151 pH for the smaller and larger cross sections respectively.

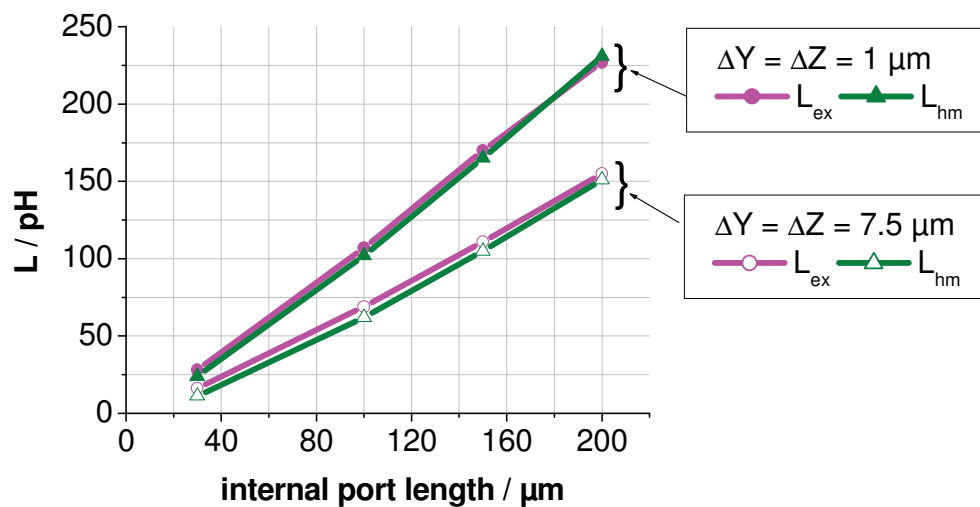


Fig. 4.16 Comparison of L_{ex} and L_{hm} as a function of the internal port length for different cross sections of the internal port cells.

Fig. 4.17 shows the extracted parasitic inductances (L_{ex}) of the internal ports of Fig. 4.9 as a function of port cross-sections for different port lengths. As L_{hm} in each case are same to L_{ex} , only one curve L is drawn. From this graph, it is evident that the inductance decreases with the increase in cross section while increasing approximately linearly with the increase in length. It is worth to mention here that the parasitic inductances are in the similar range with the line inductance. For example, in the case of 200 μm port length and $1 \mu\text{m} \times 1 \mu\text{m}$ port cross section, the line ($l=1600 \mu\text{m}$) possesses total inductance of 1.32 nH (0.82 pH / μm) whereas the parasitic inductance is 227 pH, which is 18% of the line inductance. This implies that in matched condition at the internal ports, the parasitic inductances have very significant influence on the line, i.e. the reflection coefficients, especially when the simulated structure is small compared to the internal port length.

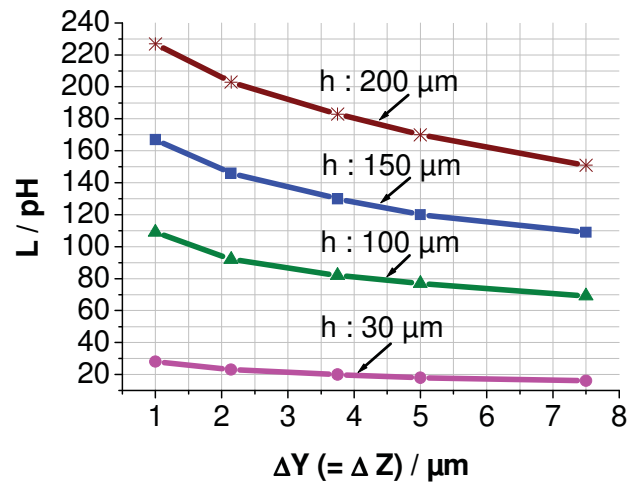


Fig. 4.17 Internal port parasitic inductance L (in Fig. 4.9) as a function of cross sectional cell dimensions of the current path ($\Delta Y = \Delta Z$) of the cells for different internal port length (h).

Following the same procedure of calculating internal port parasitic inductance in the case of a MS line in Fig. 4.9, a CPW line (Fig. 4.18) is studied. Again the internal ports are placed at the ends of the lines. The paths of the internal ports are defined in this case in the y direction and the cross sections are in the XZ planes. L_{ex} and L_{hm} are calculated for different discretizations and gaps (g) between the signal and ground lines. It is found that both values of parasitic inductances agree well in all cases of different discretizations and gaps. The parasitic inductances (L_{ex}) are plotted in Fig. 4.19. Again, it is evident that the inductance decreases with the increase in cross section while increasing linearly with the increase in length.

Furthermore it is interesting to compare the MS and CPW cases (see Fig. 4.17 and 4.19). Both yield identical parasitic inductances – for example for $30 \mu\text{m}$ internal port length, cross sections of $1 \mu\text{m} \times 1 \mu\text{m}$ and $5 \mu\text{m} \times 5 \mu\text{m}$, shows the inductance values of 30 pH and 20 pH in both the cases of MS and CPW lines.

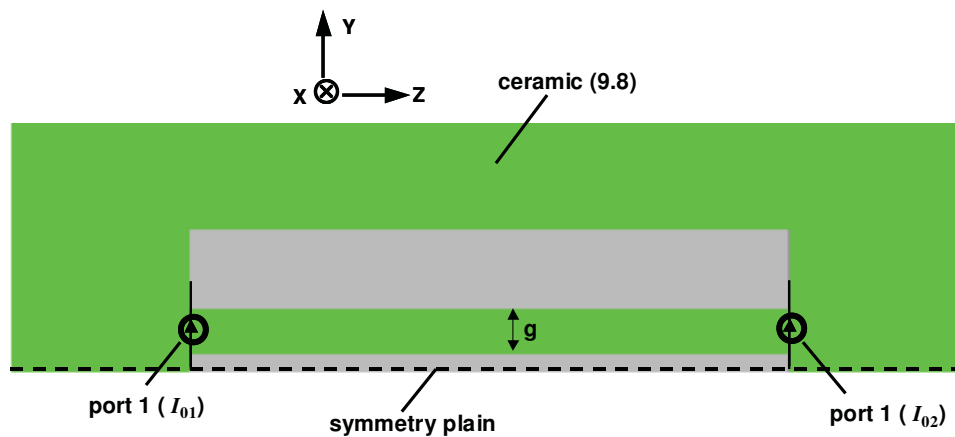


Fig. 4.18 CPW: The conductor backed ceramic substrate is $254 \mu\text{m}$ thick. The thickness of the metallizations is $5 \mu\text{m}$. The widths of the signal and ground lines are $60 \mu\text{m}$ and $120 \mu\text{m}$ respectively. The ground to signal gap (g) is varied. Only the half structure made by magnetic wall symmetry plain is simulated. The internal ports are inserted between the ground and signal lines at the two ends of the line.

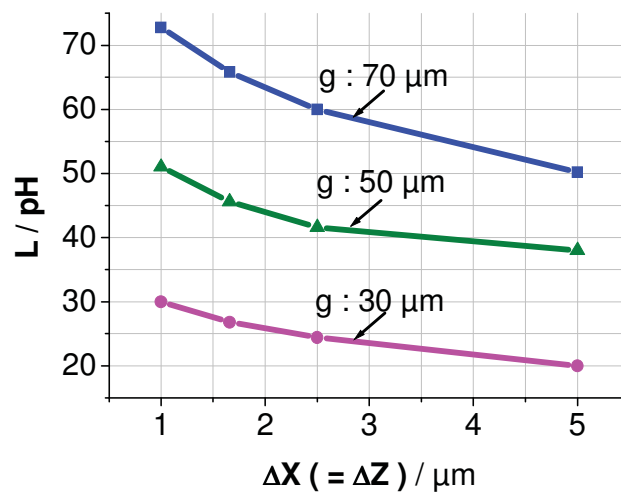


Fig. 4.19 Internal port parasitic inductance L_{ex} for the CPW structure of Fig. 4.18 as a function of cross sectional cell dimensions of the current path ($\Delta X = \Delta Z$) for different internal port length (h).

4.5 Simulations with Internal Port

In the previous subsections feasibility and parasitic effects of the conduction current internal ports were verified using MS and CPW lines. Here some applications of internal ports will be demonstrated. First, the conversion (i.e. connection) of an internal port to a lumped resistor will be examined by a T-junction. Second, the current distribution on the gate and drain fingers of the taper shaped HEMT structure of Fig. 1.2 will be examined using internal ports.

4.5.1 T-junction

The T-junction is realized with thin-film micro-strip lines on BCB substrate (Fig. 4.20). All conductors are lossless. The characteristic impedances of the lines are 50Ω . The ground pads are connected to the ground PEC with vias. Three internal ports are inserted between the centers of signal pads and the ground underneath the substrate. After calculating the Z-matrix for the T-junction, internal port 3 is connected to a 50Ω resistor. See Appendix 7.4 for the connecting lumped elements to internal ports.

The resulting 2-port Z- and S-parameters are compared with the measurement results (Fig. 4.21). During measurement of such T-junction the same procedure is applied – one port was terminated with a known resistor (usually 50Ω) and the S-parameters were measured between the other two ports. In the case of simulations, the reflection coefficients are 0.33 and transmission coefficients are 0.66 for the whole frequency range. The measurement results show good fitting with the simulation results, although the simulation is carried out with a lossless structure.

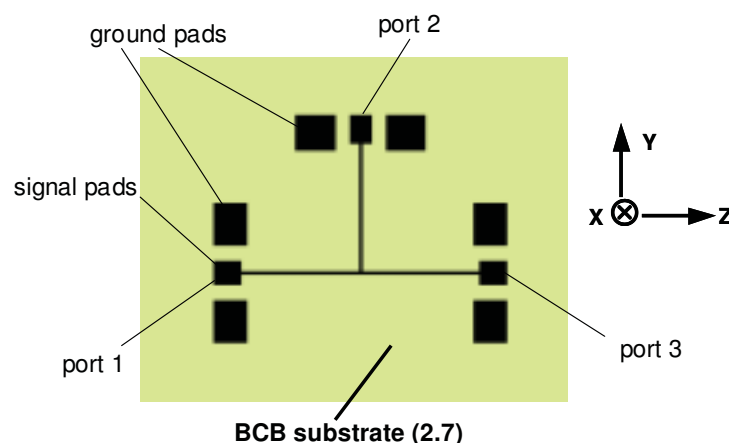


Fig. 4.20 The MS lines and pads of the T-junction are located on $5.3\ \mu\text{m}$ thick BCB substrate ($\epsilon_r = 2.7$). Each arm of the MS line is $325\ \mu\text{m}$ long, $8\ \mu\text{m}$ wide. The ground and signal pads are of $92\ \mu\text{m} \times 110\ \mu\text{m}$ and $75\ \mu\text{m} \times 60\ \mu\text{m}$ cross sections. The top metallization is $4\ \mu\text{m}$ thick.

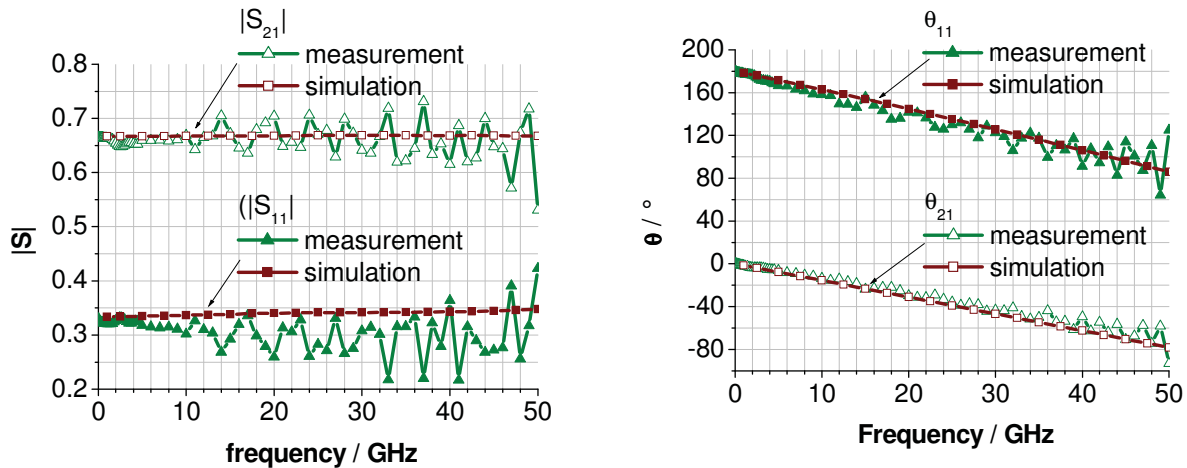


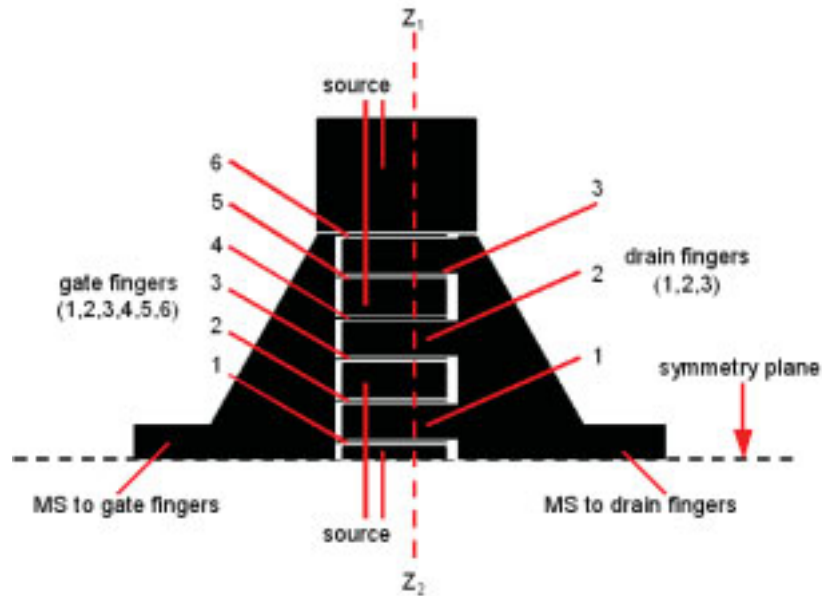
Fig. 4.21 Comparison between simulation (with internal port) and measurement for the S-parameters (magnitude in the left and phase in the right). In simulation a 50Ω resistor is connected to the port 3, while in measurement port 3 is terminated by 50Ω as well.

4.5.2 HEMT Structure

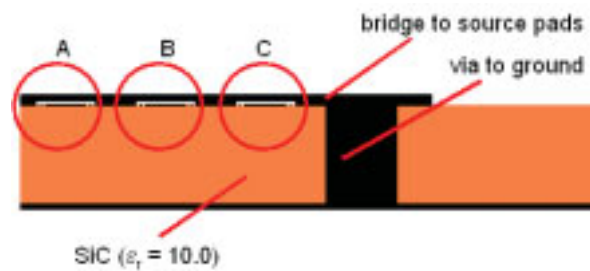
A taper shaped HEMT structure (Fig. 1.2) was introduced in Chapter 1 in order to show the necessity and use of internal ports. Such HEMT structures are optimized in [52] in order to provide an equal distribution of current to the gate and drain fingers of the transistors. The structure here is not optimized yet, presented just to show the application of internal ports.

For clarity Fig. 1.2 is redrawn here as Fig. 4.22. Half of the structure is realized by a symmetry plane (magnetic wall) and considered for the simulation. The different dimensions of the structure are listed in Tab. 4.2. Between the MS and fingers the taper (triangular metallization) is $150\ \mu\text{m}$ long in the direction of the MS line and $275\ \mu\text{m}$ long in the direction perpendicular to the MS line. 6 gate fingers as well as 3 drain fingers are connected to the corresponding MS lines through tapers (a). The source pads are connected to each other through a bridge and to the ground through a via (b). All of these metallizations are placed on SiC substrate. Internal ports are placed between the gate fingers and source bridge as well as between the drain fingers and source bridge. The MS lines are also fed by internal ports at the ends of the lines. The encircled regions of A, B and C in (b) are the same – i.e. all the transistors are of the same dimensions. (c) shows the zoomed region of encircled A (or B or C) where the three internal ports are inserted between the fingers and source bridge. A total of 11 internal ports is used for this structure - 6 internal ports are used for the 6 gate fingers, 3 internal ports for the 3 drain fingers and 2 internal ports at the outer ends of the MS lines. A 3D simulation with all these internal ports provides a Z-matrix of dimension 11×11 . The goal was to determine the current distribution through the gate and drain fingers varying the output impedances of the gate and drain fingers.

a) : Top view



b) : Z_1 - Z_2 cross-section



c) : A, B, C (zoom) :

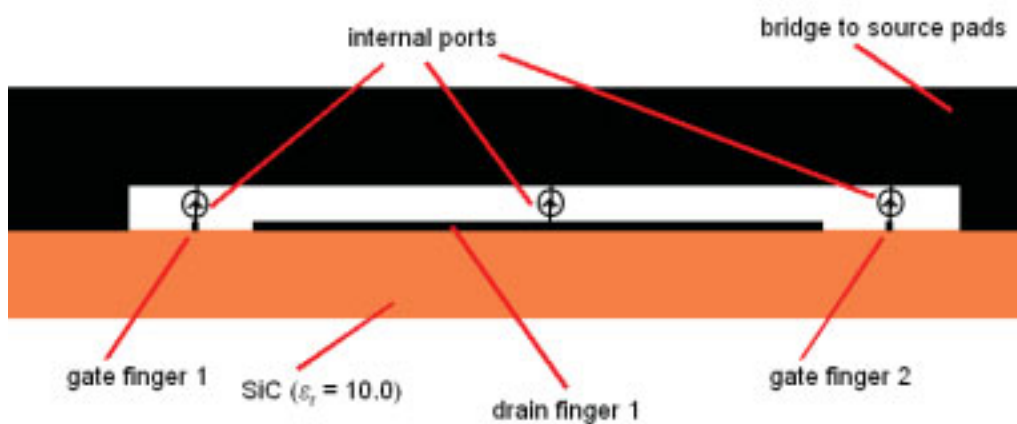


Fig. 4.22 Taper shaped transistor (HEMT) structure (half above the symmetry plane).

- organisation of the gate, drain fingers and source pads together with the MS line connecting the gate and drain fingers through the tapers.
- cross-sectional view of the structure at Z_1 - Z_2 of (a). The source pads are connected with each other through a bridge and to the ground through a via. The substrate used is SiC ($\epsilon_r = 10.0$).
- The encircled regions of A, B and C are identical. The zoomed region of encircled A (or B or C) shows the three internal ports between gate finger and source bridge, and between drain finger and source bridge.

	SiC	MS	gate finger	drain finger	source pad
thickness (μm)	100	7	0.5	0.5	0.5
width (μm)	600	90	0.36	47.12	47.84
Length (μm)		100*	135	125	140

Tab. 4.2 Dimensions of the tapered HEMT structure of Fig. 4.22 taken from [52].

Fig. 4.23 shows the schematic to calculate the currents at each gate as well as drain fingers after the EM-simulations have been performed. The resulting Z-matrix is fed by two currents I_{in}^g and I_{in}^d replacing the internal ports at the outer ends of the MS lines, which connect the gate and drain fingers, respectively. Each gate and drain finger is terminated by load impedances of Z_{out}^g and Z_{out}^d , respectively connected to the internal ports at the fingers. The currents through the loads are monitored while varying the load impedances. The impedance values are taken according to [52].

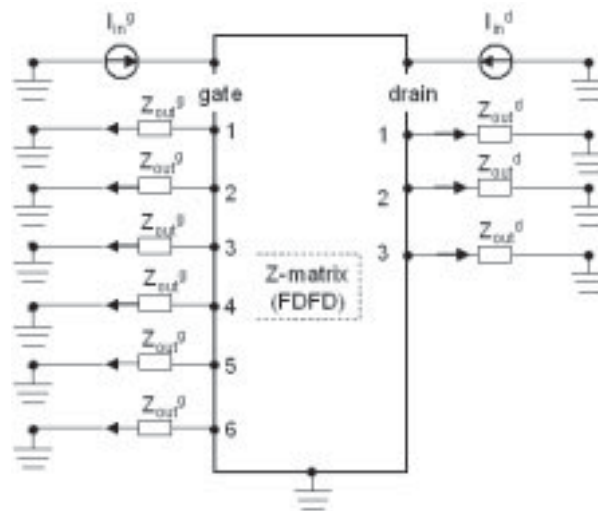


Fig. 4.23 The structure in Fig. 4.22 is simulated by means of the FDFD method. The resulting Z-matrix is fed by two current sources (I_{in}^g and I_{in}^d) placed at the outer ends of the MS lines. The internal ports at the fingers are terminated by Z_{out}^g and Z_{out}^d . The resulting currents through the gate and drain fingers are calculated.

Fig. 4.24 shows the magnitudes and phases of the output currents through the gate and drain terminations for $Z_{out}^g = 43.2 \Omega$ and $Z_{out}^d = 100.5 - j84 \Omega$, respectively. The input currents are 1 mA. Here G1 denotes gate finger 1, D1 drain finger 1 in Fig. 4.22, etc. The magnitudes of the currents through the gate fingers increase from gate 1 at the center to gate 6 at the periphery. The differences increase with the increase in frequency. At 15 GHz, for example, the current through gate 6 (G6) is 10.5% larger than the current through gate 1 (G1) whereas at 20 GHz the difference is 12.5%. The current distributions among the drain fingers are also not equal. The inner-most drain finger (D1) allows more current than the outer-most drain finger (D3). Again the difference increases in higher frequencies. At 15 and 20 GHz the difference in current magnitudes between the inner and outer drain fingers are 6% and 10%, respectively. In terms of power this difference is just double – e.g. at 15 GHz the power level at gate 6 is 25% larger than the power level of gate 1.

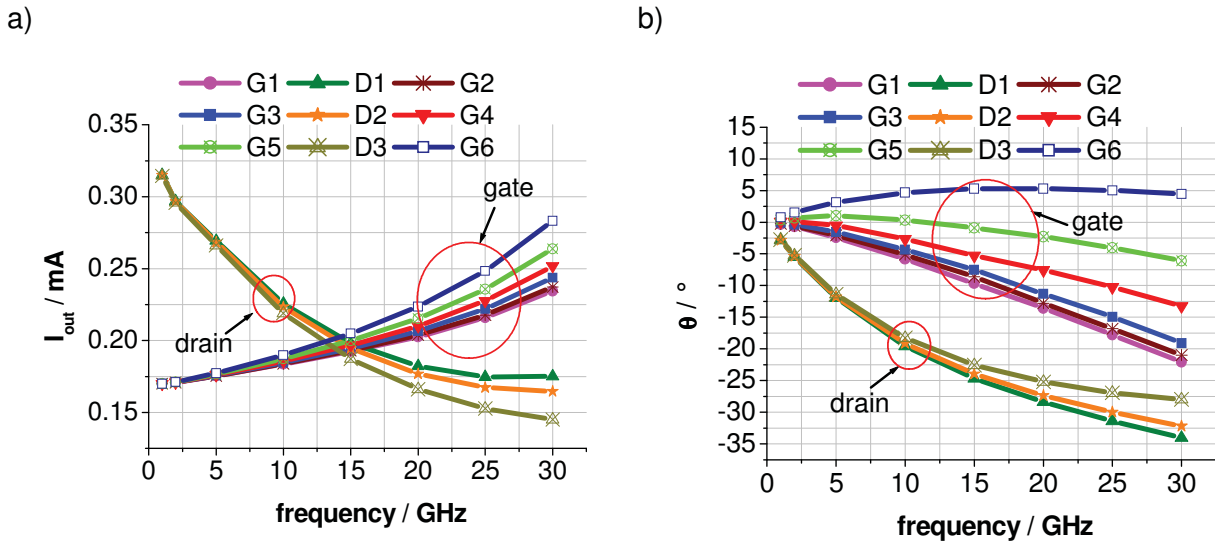


Fig. 4.24 Magnitudes (a) and phases (b) of the output currents through the gate and drain fingers ($Z_{out}^g = 43.2 \Omega$, $Z_{out}^d = 100.5-j84 \Omega$ and $I_{in}^g = I_{in}^d = 1 \text{mA}$).

This uneven distribution of currents among the gate and drain fingers depends greatly on the impedance values of their terminations. If the gate terminations are 100Ω , we do not see significant change in current magnitude among the gate fingers (Fig. 4.25.a). However if the terminations are 20Ω , there is a very large difference in current magnitudes among the gate fingers (Fig. 4.25.b). Already at 10 GHz, the outer-most gate (G6) current is 16% larger than the inner most gate (G1) current. The same is also true for the current distribution among the drain fingers. Even though identical transistors are used, their output powers at the gate and drain fingers may vary considerably depending on the impedances at the gate and drain fingers.

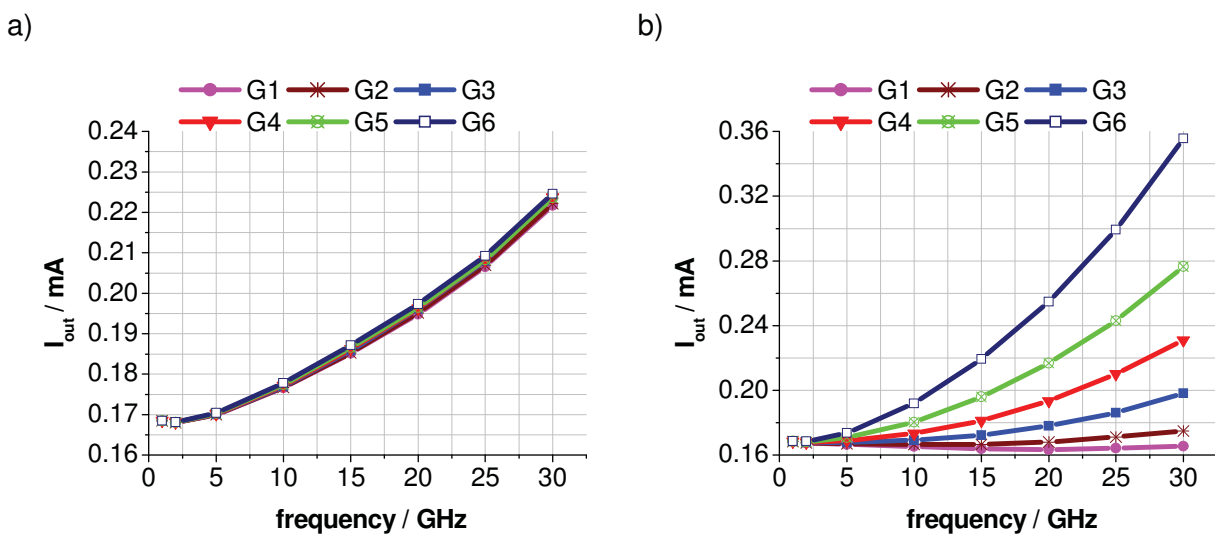


Fig. 4.25 Magnitudes of the output currents through the gate fingers. $I_{in}^g = I_{in}^d = 1 \text{mA}$.
 (a) : $Z_{out}^g = 100 \Omega$ and (b) : $Z_{out}^g = 20 \Omega$

4.6 Conclusion

Internal ports are used to feed a structure at certain points inside the structure, especially when the structure is entirely bounded by PML as well as electric/magnetic walls. They allow to interface network descriptions of sub-structures or active elements with EM-simulation, which is particularly important if active elements and/or sub-structures with considerable smaller dimensions are to be included.

Two different approaches for implementing internal ports in FDFD method are examined. The first one is the relaxation current source, where two lumped time varying charges of equal magnitudes but opposite polarities are inserted at the two nodes of the internal port. It is shown that this approach excites non-physical solutions and therefore is not feasible to work as an internal port.

The more important approach is the conduction current or line-current source, where a path of cells is defined between two conductors and a source current is introduced along the path. This approach proved to be a very useful and versatile tool.

A more detailed study reveals that the conduction current internal port approach comes up with a parasitic inductance. According to the FDFD discretization scheme, this inductance has been estimated as the inductance of a rectangular wire (L_{hm}) assuming a homogeneous current density over the cross section of the wire. Two line structures, MS and CPW are examined in order to extract the parasitic inductance numerically (L_{ex}), where two internal ports are placed at the ends of the lines. It is found that the closed-form approximation for the parasitic inductance approximates the actual values with good accuracy.

Finally, a T-junction and a HEMT feeding structure are treated demonstrating usefulness of the internal-port concept.

5 4-Quadrant Slot Antenna

5.1 Introduction

Distributed sensor systems are presently a hot topic of research and development, since they offer various applications in industry, production lines, environmental controlling and furthermore, such sensor systems comprise numerous very small sensor nodes in order to control and measure local properties, e.g. temperature, material density, viscosity etc. These sensor nodes are used to be self-dependent, i.e. equipped with full functionalities so that they can exchange information with each other and eventually send the desired information to the base node. Keeping in mind such necessities, an antenna for low power monolithic 24.1 GHz front-ends was developed within the framework of a BMBF project. This is presented in the following.

The antenna is designed for lateral radiation, which makes it more attractive to be integrated with the planer circuit boards and allows the separation of radiation into four quadrants, each of which works like a horn type slot antenna. It can be readily integrated with the front-end circuitry for the use of transmission chip. The integration of the front-end chip within the antenna reduces the number and length of the device-frontend interconnects and connecting signal lines, thereby results in reduced parasitic effects/ losses. The antennas are compact and compatible with standard packaging techniques.

Fig. 5.1a shows the basic antenna system with each antenna to be controlled by the RF circuitry independently from each other.

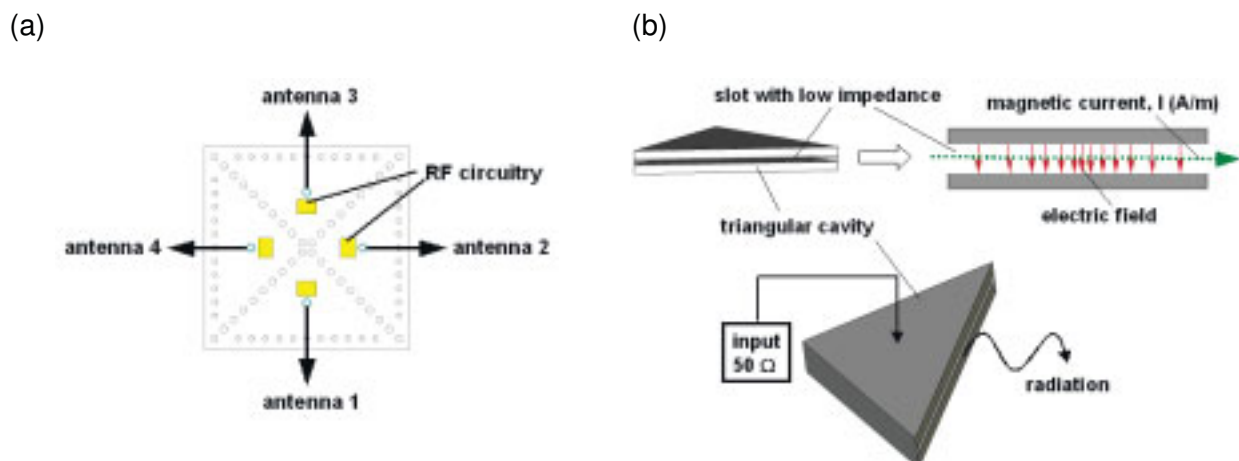


Fig. 5.1 The four quadrants antenna structure made up of triangular cavities separated by diagonally placed bump fences between two rectangular metal plates. (b) describes the working principle of one of the triangular cavities of (a). The bump fences are here replaced by closed metal walls for simplicity.

One quadrant of the antenna can be thought of as a triangular cavity resonator, a half of a common rectangular cavity resonator (Fig. 5.1b). The cavity is formed by a thin slot between two metal plates and separated from the other cavities by diagonally placed bump fences. The slot has a low characteristic impedance. When the cavity is excited, radiation takes place. The thin slot with the electric fields can be described by an equivalent line of magnetic current source [44], radiating in the free space. Due to the thin slot the radiation takes place laterally. In order to have the maximum radiation the cavity must be tapped in such a way that the excitation at a certain position in the cavity results in resonance and the cavity acts as a transformer. In addition, as the resonance takes place at the frequency of operation, the antenna provides automatically a filtering behavior.

The basic challenges in simulating such an antenna structure are the huge mesh size due to the diverse dimensions and the open boundaries to evaluate radiations. Moreover, waveguide ports are not suitable in this case as the whole structure is to be bounded by PML absorbing boundary conditions. Therefore, internal ports are necessary to excite the antenna internally. In Chapter 2 it has been shown how the bad convergence behavior due to the inclusion of anisotropic PML in the FDFD method can be alleviated. The excitation of a structure internally through internal ports has been described in Chapter 4. The slot antenna will be demonstrated in this chapter as a practical example where both the PML and internal ports are exploited in the simulations based on the FDFD method. In the FDFD simulations the PML walls used are non-overlapping and PML cell sizes are the largest ones in the whole mesh. Finally, the simulation results according to the FDFD method are compared with those obtained CST MWS in FDTD method.

5.2 Antenna Design

The basic structure of the antenna is given in Fig. 5.2. The antenna is built as a sandwich structure. It consists of an upper and a lower metalized planar substrate stacks which are flip-chip mounted face-to-face thus forming a parallel-plate resonator and creating an air gap as thick as the bump height. This resonator is partitioned into 4 quadrants by the bump fences. The metal blocks below and above this sandwich structure are arbitrary blocks with proper shielding (electric walls) which ensure appropriate beam-forming. In reality, these blocks may contain a further stack of substrates with low frequency electronic modules or the battery, for instance. The only condition is that these blocks need via fences or similar arrangements at the sides to shield them against the RF radiation from the slot. The arrangement of the antenna structure allows to integrate an RF frontend together with a complete transceiver function into a cube of compact size.

Fig. 5.3 shows a more detailed view of the lower half of the antenna with its layers in a hierarchical view. Backside-metalized Rogers 4003 material ($\epsilon_r = 3.38$) of 508 μm thickness is used for the antenna substrates. The slot metallization is 35 μm thick and the aperture height, i.e., the distance between the two metallization of the parallel-plate wave guide, is 300 μm . The excitation bump is connected to the upper metallization and the current flows back through the bump fences over the lower metallization.

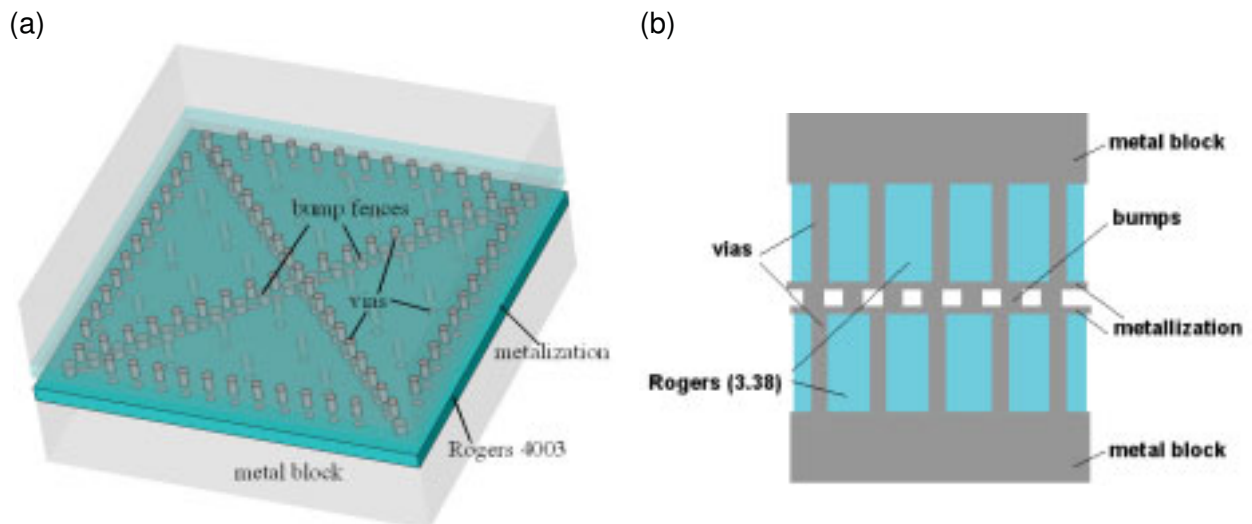


Fig. 5.2 The basic structure of the 4-quadrant slot antenna (a). The diagonally placed bump fences separate the structure into four triangular horn type antenna sectors. (b) provides a cross-sectional view. The slot is formed between the metalizations.

The bump fences reflect the electromagnetic waves generated by the excitation bump in a way similar to a horn antenna and form an electrical separation between the 4 quadrants. So each quadrant works as a horn type slot antenna, can be understood as a triangular cavity with an open slot at the outer boundary and excited by the bump near the centre of the cavity. Because of the low cavity height there is a strong mismatch between the cavity impedance and that of the outer space. Therefore the cavity is operated near the resonance, which allows impedance transformation and results in a resonant antenna with filtering properties. The bumps also have the function of mechanically connecting the upper and lower half of the resulting set-up. Within the upper and the lower substrate, via fences at the edges form an artificial shielding to block the RF radiation originating out of the slot from penetrating into the substrate. Inside the substrate vias are needed to prevent resonances in the substrate excited at excitation bump. For this purpose, some vias are distributed over each quadruple section.

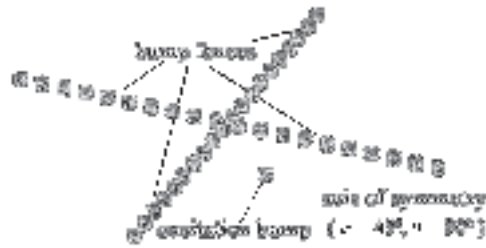
Regarding design the most essential specification for the antenna is that its resonant frequency should meet the centre frequency of the ISM band around 24.1 GHz. The shape of the antenna lobe is not an equally important issue because the antenna is to be applied in near-range communications with comparatively low constraints on radiation pattern.

The bump and via fences must have a certain density to make sure that there is only low coupling between the sections and that no resonances occur in the substrates, respectively. On the other hand, the distance between the bumps cannot be chosen arbitrarily small because the bump pitch has a lower limit for technological reasons. Similar restrictions hold for the minimum via pitch in the substrate.

There are different parameters that cause large tolerances, which in turn result in a shift of the resonance frequency or change in the radiation level. Among these, the most important parameters are the length of the slot (i.e. the outer dimension of the antenna), the position,

height and diameter of the excitation bump and the height of the metal block. Electromagnetic simulations are carried out to check the tolerances of the above parameters, to find out the parasitic resonances and to optimize the layout.

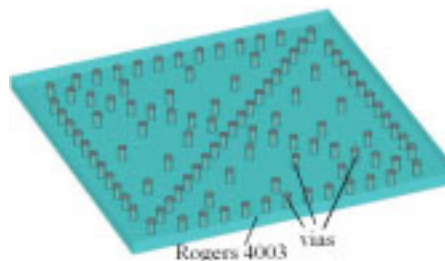
(a)



(b)



(c)



(d)

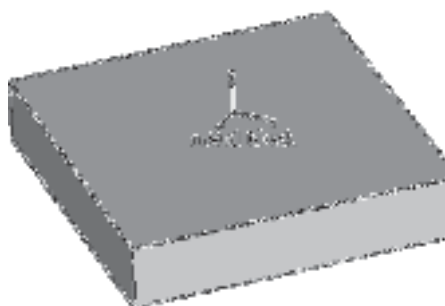


Fig. 5.3 Hierarchical view of the lower symmetrical half of the antenna. (a): the bump fences that realize separation of the rectangular cavity into four quadrants. (b): the lower metallization with the opening for the excitation bump. (c): The Rogers substrate with vias. (d): the metal block which serves here as a representation for the space where further functionalities can be realized.

5.3 Simulation results in FDFD

The F3D simulator based on the FDFD method with PML and internal ports is used for design issues and to determine the influence of tolerances of the physical parameters of the antenna. As the four triangular antennas, i.e. the four quadrants, are electrically separated and decoupled from each other by the diagonally placed bumps, it is sufficient to simulate only one of those antennas. Fig. 5.4 shows one half of the whole antenna structure. In comparison to the basic structure given in Fig. 5.2 and Fig. 5.3, rectangular-type vias and bumps of same cross-sectional areas are used. The height of the metal block (h , see Fig. 5.4.b) is varied between $35\ \mu\text{m}$ to $2500\ \mu\text{m}$. PML walls of five layers are used for the open boundaries.

At the beginning, some investigations were carried out in order to estimate the number of vias and bumps in the fences which are necessary to keep crosstalk among the quadrants sufficiently low. For very coarse fences, additional resonances occur due to the relatively strong coupling. Increasing the bump density, the desired single-resonance behaviour is found but the value of the resonant frequency still changes because the resulting inductance of the bump fences varies. For the targeted purposes, it is found that 9..10 vias or bumps at each arm yield good results.

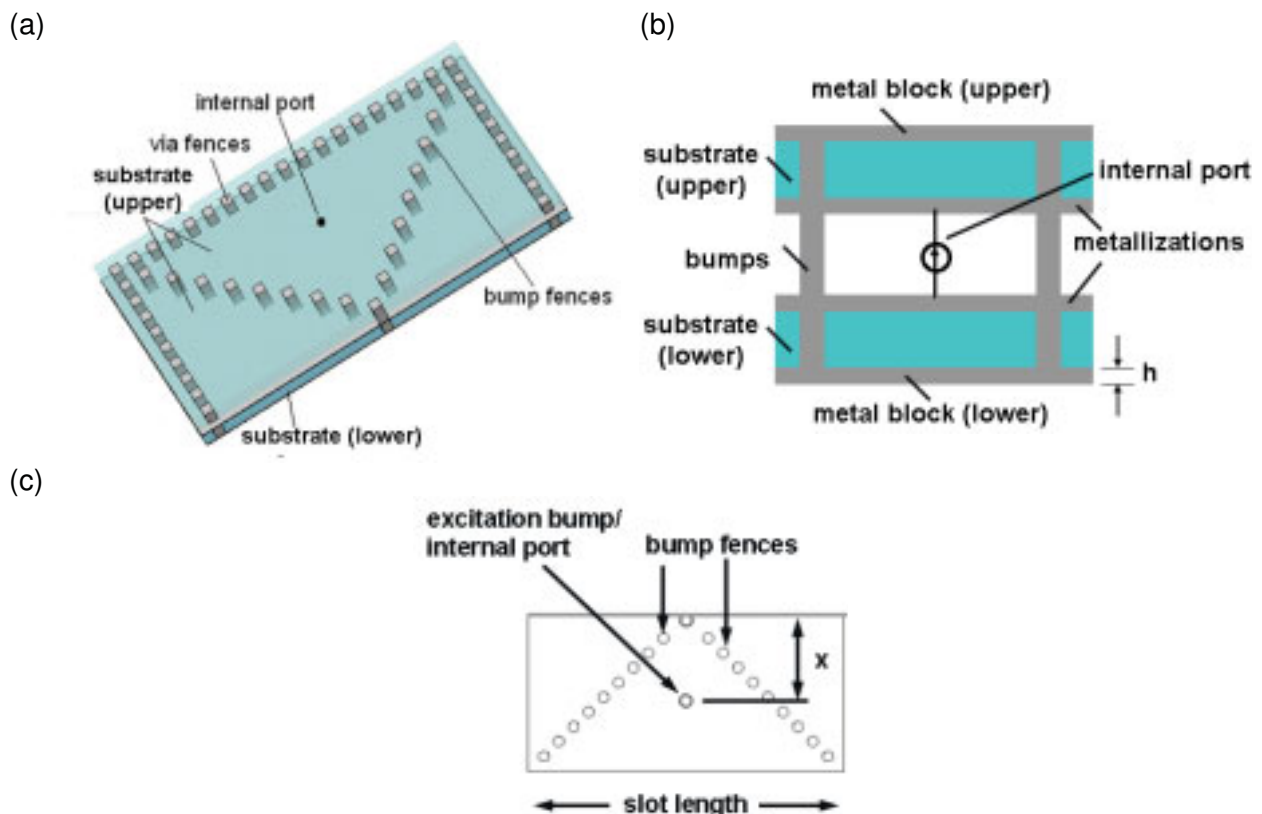


Fig. 5.4 a): the structure simulated: one half of the basic antenna structure given in Fig. 5.2.
 b): cross-sectional view (not scaled) – bumps are extended through the substrates to work as vias as well. Internal port is placed between the two metallizations.
 c) : top view (from at the center of the slot) – definition of the slot length and the position of the excitation bump / internal port (x) from the center of the 4-quadrant antenna

The length of the slot (see Fig. 5.4.c), i.e. the outer dimension of the antenna determines the resonance frequency. Fig. 5.5 shows the reflection at the internal port for different slot lengths varied between 11 to 13 mm. A 1 mm change in the slot length results in around 2 GHz shift in frequency. For a center frequency of 24.1 GHz, one has a slot length of around 11.6 mm. It should be noted here that the antenna is excited by an internal port placed along the symmetry axis (Fig. 5.3.a) between the upper and lower metalizations without taking into account the excitation bump itself (Fig. 5.4.b). The height of the metal block (h) is 35 μm here.

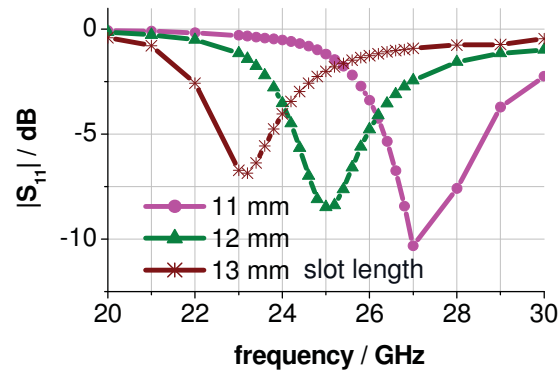


Fig. 5.5 Influence of the slot length on the resonant frequency. An internal port between the upper and lower metallization is used without excitation bump. The metal block is assumed to be 35 μm thick (h).

The tolerances of the height of the aperture, i.e., the distance between the two metal plates (metallizations, see Figs. 5.2, 5.3 and 5.4.b), are checked by simulating the structure both in F3D and CST MWS. Again the antenna is excited by an internal port and the metal block is 35 μm thick. The corresponding results are plotted in Fig. 5.6. The bandwidth, i.e. selectivity characteristics of a slot antenna, is same as that of the magnetic dipole antenna (complementary dipole) [49]. Increase in the slot height, i.e. smaller ratio between the slot length and slot height results in the increase in the band width of the slot antenna, in the same way as increasing the thickness of a dipole increases its bandwidth. As one can see in each case of FDFD and FDTD, increasing the slot height from 250 μm to 350 μm increases the bandwidth without shift in the resonance frequency.

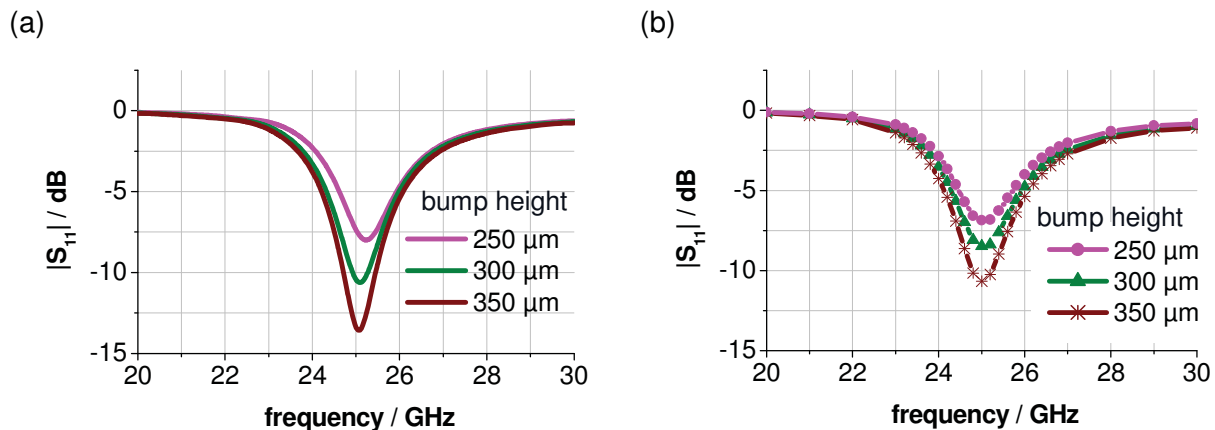


Fig. 5.6 Effect of slot height (bump height) calculated using FDFD method (a) and CST MWS (FDTD method) (b). The metal block is assumed to be 35 μm thick (h).

The position of the excitation bump (x , Fig.5.4.c) is important in order to achieve a good matching. Therefore, the structure in Fig. 5.4 is simulated again for varying x with both the F3D simulator in FDFD method and CST MWS and the metal block height of 35 μm . It means that the internal port representing the excitation bump is moved along the symmetry axis (Fig. 5.3a) with various distances from the centre point of the antenna, the crossing point of the diagonals. The simulation results of reflection coefficients at the internal port for different positions of it are shown in Fig. 5.7. From the results of both the FDFD and FDTD procedures it is evident that by changing the position of the excitation the impedance of the internal port (input impedance, 50 Ω) can be matched with the characteristic impedance of the slot resulting in a higher level of radiation (i.e. high return loss). However, shifting the bump causes also a slight shift in resonance frequency, with different level of radiation depending on the actual position. The shift in the port position in either direction by 300 μm results in more than 5 dB change in radiation level as well as more than 0.2 GHz shift in frequency. Thus, the slot length has to be adapted iteratively in order to fix the resonant frequency to the specified value.

Also, the height of the metal block (h) has an influence on the matching. The radiation levels in the previous calculations were too low, because a relatively thin block of 35 μm was assumed. The same calculations are done except that the metal block is assumed to be to 2.5 mm. Fig. 5.8.a shows the reflection levels out of the simulations in FDFD for varying slot heights. Comparing Fig. 5.6.a and 5.8.a yields that radiation level is increased in all cases of different slot heights due to the increase in the thickness of the metal block from 35 μm to 2.5 mm, e.g. from -8 dB to -28 dB for the slot height of 300 μm . The simulation results carried out in FDTD method are shown in Fig. 5.8.b and provide, when compared with those of Fig. 5.6.b, good resemblance with those of the FDFD method, e.g. from -11 dB to -29 dB for the slot height of 300 μm

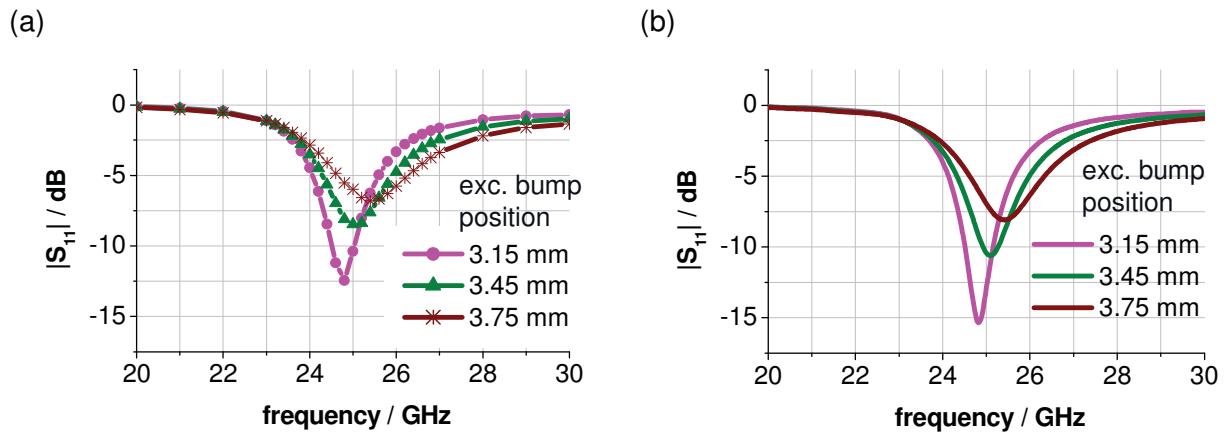


Fig. 5.7 Effect of the excitation bump position, the distance between the centre of the antenna and the internal port position along the symmetry axis (see x in Fig.5.4.c and Fig. 5.3a). The calculations are carried out using F3D simulator (a) as well as with CST MWS (b).

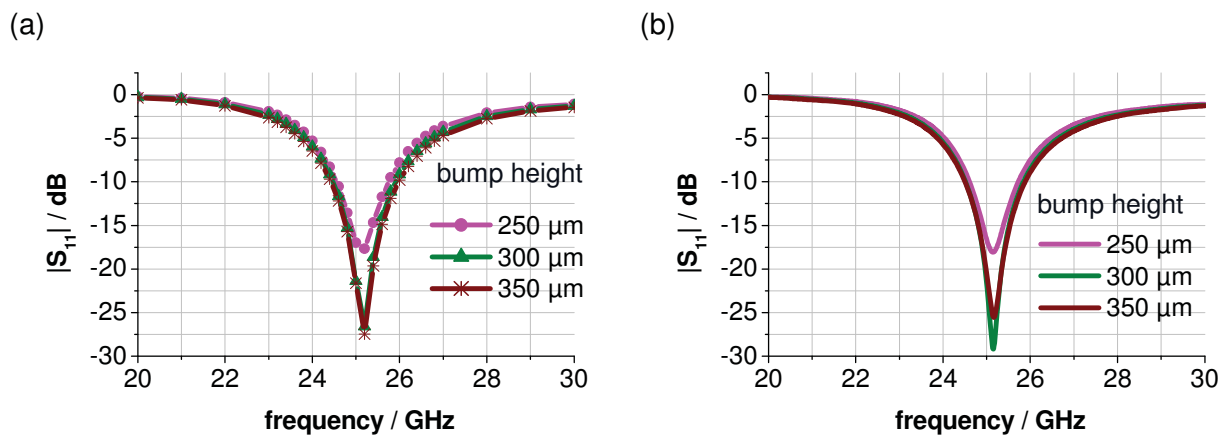


Fig. 5.8 Influence of the metal block (h) on the reflection level for varying slot heights calculated with FDFD method (a) and with FDTD method (b). ($h = 2.5\text{mm}$)

So far, the simulations are carried out directly with an internal port placed between the metallizations without taking into the effects of the excitation bump. In the following the influence of the dimension of the excitation bump and the opening that realizes the pad for the excitation bump (with a square cross section of $300\ \mu\text{m} \times 300\ \mu\text{m}$) will be checked. The internal port is placed within the opening between the center of the pad and the lower metallization. As shown in Fig. 5.9.a and 5.9.b the excitation bump is placed on the pad with a $150\ \mu\text{m}$ opening around it. The resulting S-parameters for different excitation bump heights, i.e. different slot heights of the antenna, are given in Fig. 5.9.c. Unlike in Fig. 5.6 and 5.7, there is a clear shift (0.1 GHz) in the resonance frequency for the different slot heights, which is mainly due to the presence of the opening. Due to the opening a part of the input power couples into the substrate and is trapped due to the substrate resonances. The substrate resonances, which are originated by the triangular substrate cavity surrounded by the via and bump fences between the lower metallization and metal block, can be clearly seen at 28 GHz.

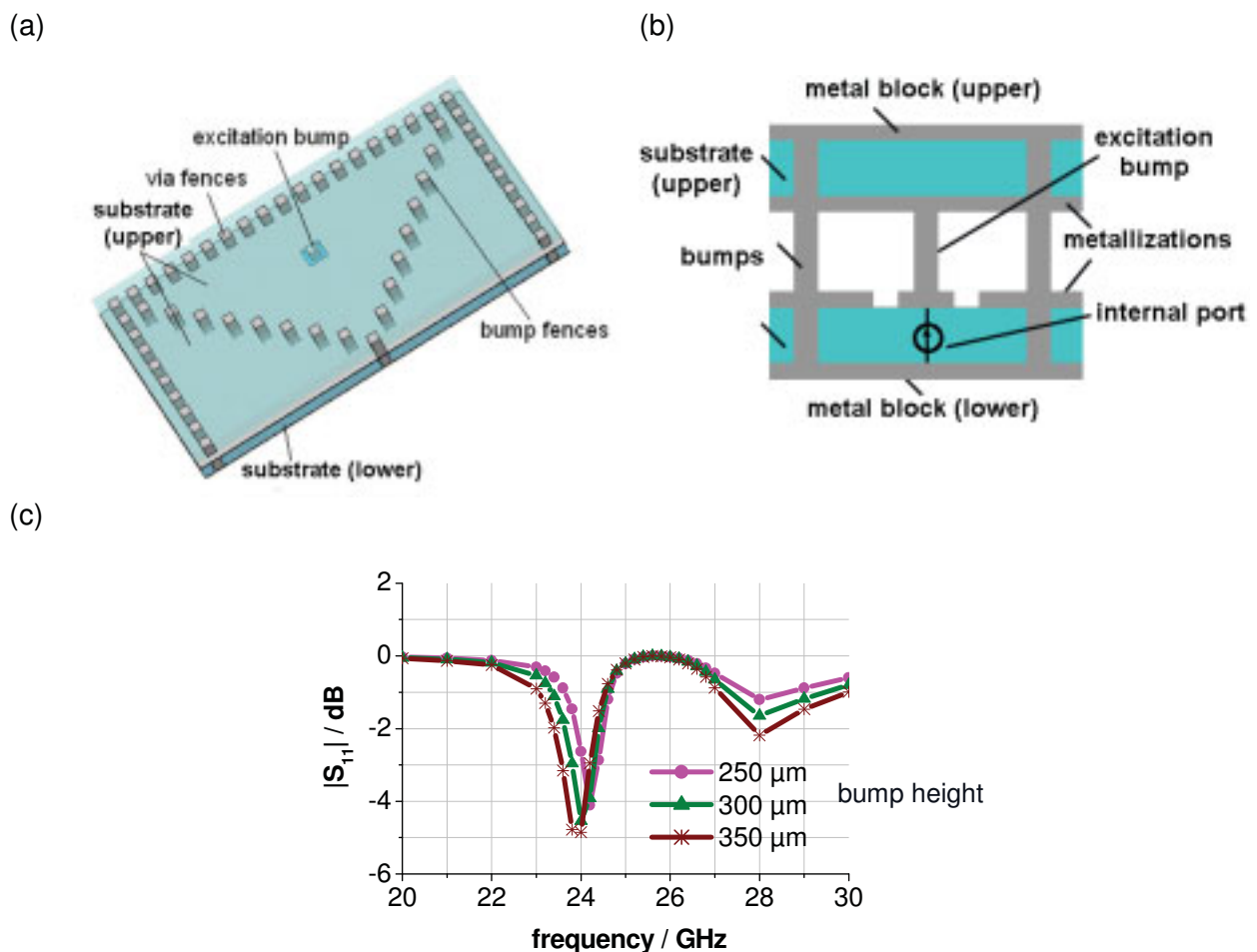


Fig. 5.9 (a): Exciting the antenna with an excitation bump. The internal port is placed between the excitation bump and the lower metal block in the lower substrate without the internal vias.

(b): cross-sectional view (not scaled) – excitation bump, opening around it and placement of the internal port

(c): The effect of the opening for the excitation bump on the input reflection of the Antenna for varying slot heights (bump heights) in FDFD method.

In order to suppress these unwanted substrate resonances, inside the substrates several vias are placed as given in Fig. 5.10.a, unlike the vias at the periphery of the substrates which are used to block the penetration of the RF radiation from outside. The size of the excitation bump, i.e. the sides of the squared cross-sectional areas, is varied from 300 μm to 400 μm while keeping the slot height at 300 μm constant and the resulting S-parameters are plotted in Fig. 5.10.b. It is clear that the resonances around 28 GHz are now absent and further more the deeper dip at 24 GHz indicates that the radiation level is increased for different bump sizes in general. If one compares the 300 μm case (slot height) of Fig. 5.9.a and 300 μm case (excitation bump size) of Fig. 5.10.b, where the difference between them is only the absence and presence of the vias inside the substrates, $|S_{11}|$ decreases from -5 dB to -20 dB. However, the shift in frequency due to different bump sizes, as shown in Fig. 5.10.b is only around 0.15 GHz.

The bonding process allows relatively large tolerances for size of the excitation bump as well as for the other bumps that separate the sectors. The balls with an initial diameter of 400 μm vary their diameter after soldering and bonding. The resulting dimension is between 340 μm and 420 μm . Again assuming rectangular shape, the side of the cross-sectional areas may vary between 300 and 375 μm . The shape of the other bumps, i.e., those in the fences, shows less influence than that of the excitation bump.

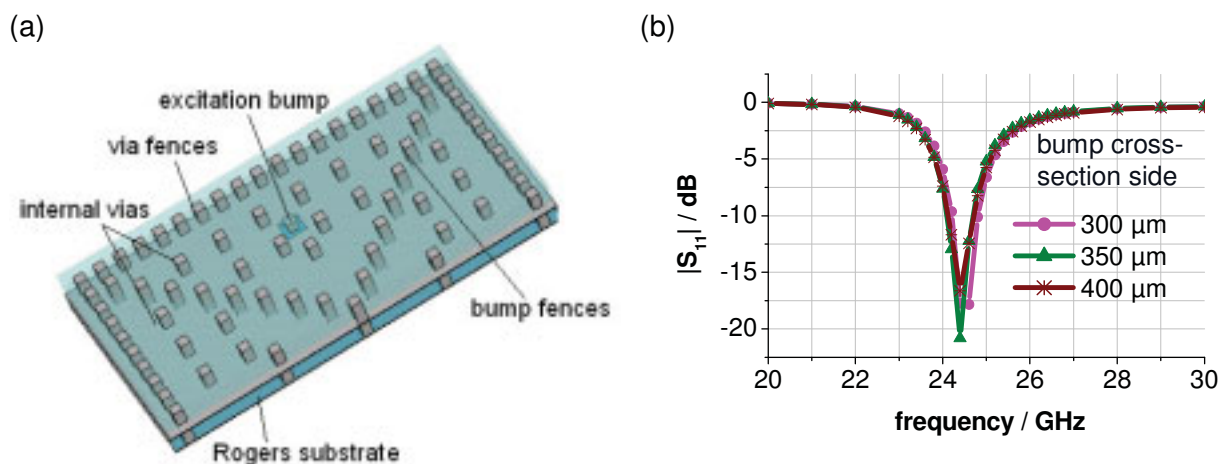


Fig. 5.10 (a): Inserting vias inside the substrate to suppress substrate resonances. (b): The effect of the size of the excitation bump. The side length from 300 μm to 400 μm of the square cross-section of the excitation bump is varied.

For the placement of the excitation bump and internal port see Fig. 5.9.b.

5.4 Realization and Measurement Results

As already mentioned the RF circuitry is integrated with the antenna. Integrating the chips of the RF circuitry into the antenna cavity needs specific design and processing efforts. Fig. 5.11.a illustrates how the chip is located inside the antenna. Here a dummy passive chip is used, which replaces the active RF circuitry for the simulations. The flip-chip mounting is used in realization of the chip integration, where two different bump sizes are used, because the chip must be smaller than the height of the cavity. The presence of the chip disturbs the field distribution inside the cavity. The disturbance takes place in two ways. Firstly due to the dielectric loading of the high dielectric constant chip (GaAs, $\epsilon_r = 12.9$) and secondly due to the CPW feeding line which contains gaps and interrupts the current flow on the metallization of the ideal slot antenna. It should be noted that in the final version of the antenna the CPW line with this shape and length will not be used, rather the CPW line will be smaller and bounded in the vicinity of the chip within the triangular sector in order to make connection between the chip and the excitation bump. Here in Fig. 5.11, the CPW line is chosen in this way in order to model the measurement test structure (Fig. 5.12). The investigations regarding the optimum location of the chip and the excitation bumps as well as the routing of the CPW line, which allows less perturbation in the surface current flow, are given in [37].

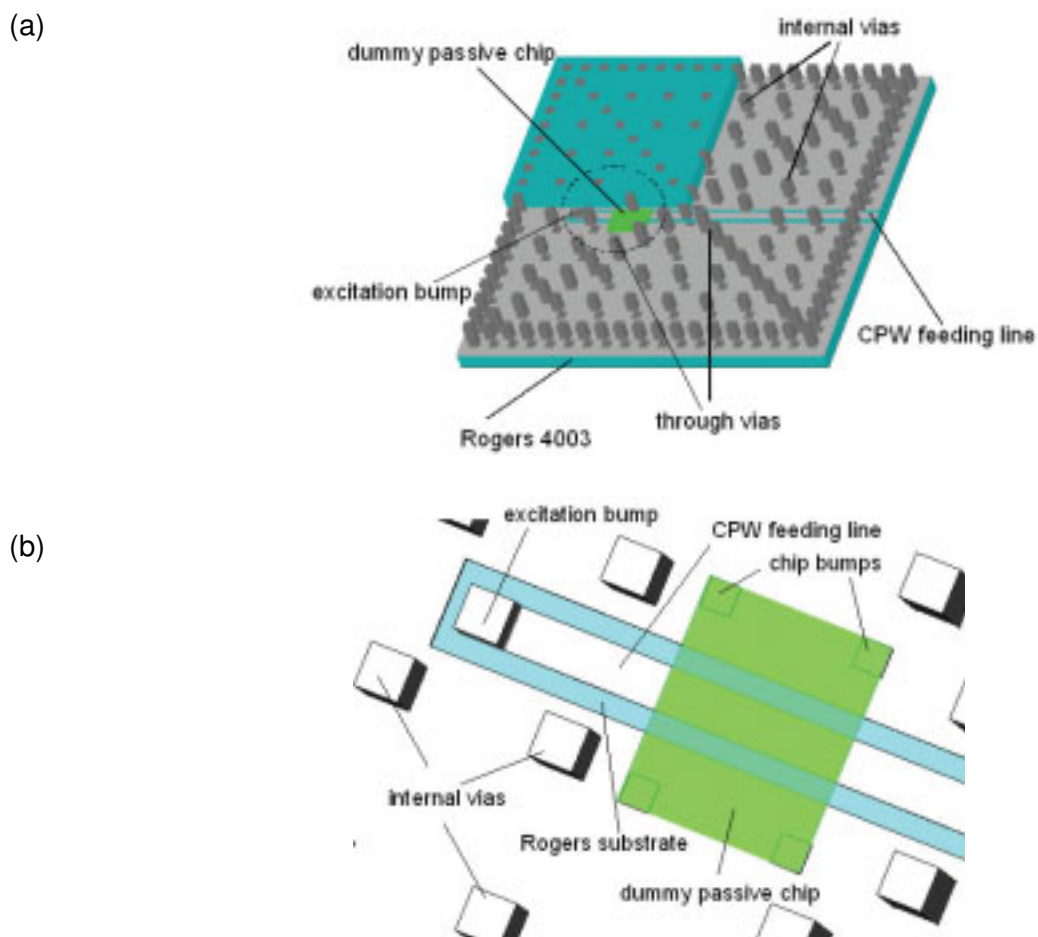
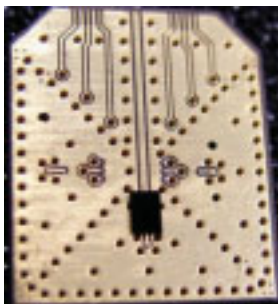


Fig. 5.11(a): Integration of the dummy chip into the antenna cavity. The antenna is fed by the CPW line through the excitation bump. (b): a detail of Fig. 5.11.a (dashed encircled region) - the dummy passive chip flip-chip mounted on the lower metallization. The chip is assumed to be GaAs with a continuous metallization on top.

For fabrication the Rogers substrates are structured by using a standard hybrid soft board process. This process is cost-effective but results in relatively large tolerances. In order to mount the passive chip, AuSn ball bumps of 80 μm diameter are deposited by using a ball bumper. The bumps need to be placed on the chip because lateral alignment is most critical here. Then, the chip, together with the balls, is flip-chip mounted onto the Rogers substrate by solder bonding. In the same way, the lower substrate with the chip is flip-chip mounted to the upper substrate, there; of course, larger bumps are needed to maintain enough margin so that the height of the mounted chip on the lower substrate is small enough compared to the resulting bump height of the second flip-chip process. Therefore, 400 μm balls have been used for this process, which defines the height of the antenna cavity. The tolerance in nominal height (300 μm) of the antenna slot is about 15...20 μm .

Fig. 5.12.a presents a photograph of the lower Rogers board after mounting the chip. The completed antenna after the second flip-chip process is shown in Fig. 5.12.b. The lower board is extended on one side to provide room for on-wafer probing or bonding of the feeding lines. The vias are realized as through-vias here. They are located along the outer edges of the substrate for shielding purposes as well as inside, where the diagonal fences separate the four sections from each other in order to avoid substrate crosstalk and the remaining vias are distributed in a way to suppress substrate resonances. The antenna corresponding to Fig. 5.12 with a CPW feeding line and a dummy chip above this line is measured. The metal block in the measured antenna is 35 μm high. This allows easy connection to a wafer prober or an SMD connector (see vertical CPW in Fig. 5.12.a). Measured data for this device is plotted together with simulation results by F3D (FDFD) and CST MWS (FDTD) in Fig. 5.13. In the simulation the structure is assumed to be lossless. The internal port is placed at the end of the CPW line opposite to the excitation bump between the CPW line and the lower metal block.

(a)



(b)



Fig. 5.12 (a): Test flip-chip integration of the chip onto the lower substrate stack. The chip is fed by the CPW line.

(b): Photograph after the second flip-chip process of placing the upper substrate stack on the lower one via bumps.

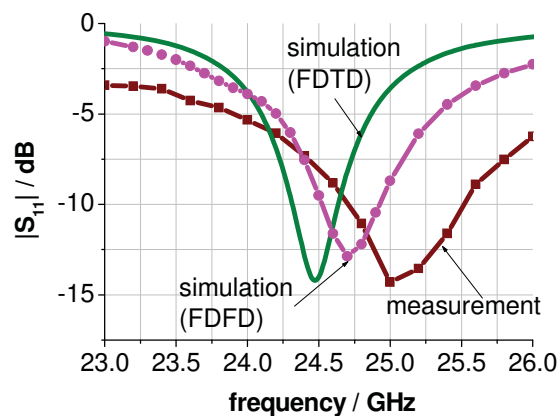


Fig. 5.13 Input reflection factor vs. frequency: comparison of measurement and simulation data by FDFD and FDTD method. The simulations and measurements refer to the structures of Fig. 5.11 and 5.12, respectively.

The shift in frequency between FDFD and FDTD cases is below 0.2 GHz. Both the simulation results differ by shifts in frequency from the measurement results despite of the good qualitative agreement. The reasons behind the deviations in the simulation and measurement results can be summarized as follows:

1. the measured antenna was the first prototype and thus showed larger tolerances than assumed a priori. This is true particularly for position and size of the excitation bump which have a distinct influence on the resonance frequency. The effect of tolerances in the antenna dimension, position of the excitation bump, size of the excitation bump are given in Fig. 5.4, 5.7 and 5.8, respectively
2. discretization error: even though the numbers of cells in both cases of the FDFD and FDTD procedures have been kept approximately the same, the cell sizes and number of cells at different discontinuities, e.g. the opening around the CPW line, vias, bumps etc., are different.
3. the conductor loss of the CPW line (approximately 10 mm long) is not considered in the simulations. However, it is hardly possible that it causes purely a shift in resonance. Rather, it causes an overall decrease in $|S_{11}|$ as can be seen from Fig. 5.13.
4. parasitics mainly due to the feeding structure, which was not part of the simulated geometry.

The determination of loss and efficiency of the antenna is given in [37] where two antennas as given in Fig. 5.11 were in face-to-face a few millimeters apart and the transmission loss was measured resulting in a loss value of 3dB per antenna which corresponds to 50% efficiency. With the help of CST MWS the directivity of the antenna was calculated 7dBi. So, the gain of the antenna is 4 dB.

In order to demonstrate functionality of the active slot antenna, a complete antenna with an integrated GaAs-HBT VCO instead of the dummy passive chip (that is why it is called an active slot antenna) [37] is realized. The MMIC chip was fabricated using the FBH GaAs-HBT process. Chip size and layout are adapted to meet the constraints given by the antenna integration. It is a coplanar circuit with a 100 μm thick substrate. The antenna with the VCO was mounted on a probe station with the appropriate DC bias and control signals applied by a probe card. The radiated signal was detected by a horn antenna as a receiver. Fig. 5.14 illustrates the measurement set-up. The results of this measurement are depicted in Fig. 5.15. What is plotted is the frequency of the received signal at the horn antenna when varying the tuning voltage and thus frequency of the VCO in the active slot antenna. An almost linear tuning range from 23.3 GHz to 25.0 GHz is observed. This proves functionality of the active antenna concept. In the final realization, the transmitter VCO is to be realized on a single chip together with a mixer and an LO, which forms a complete RF frontend. Then, the bias supply as well as the IF signals can be fed through vias from the backside so that the four sections can be operated independently.

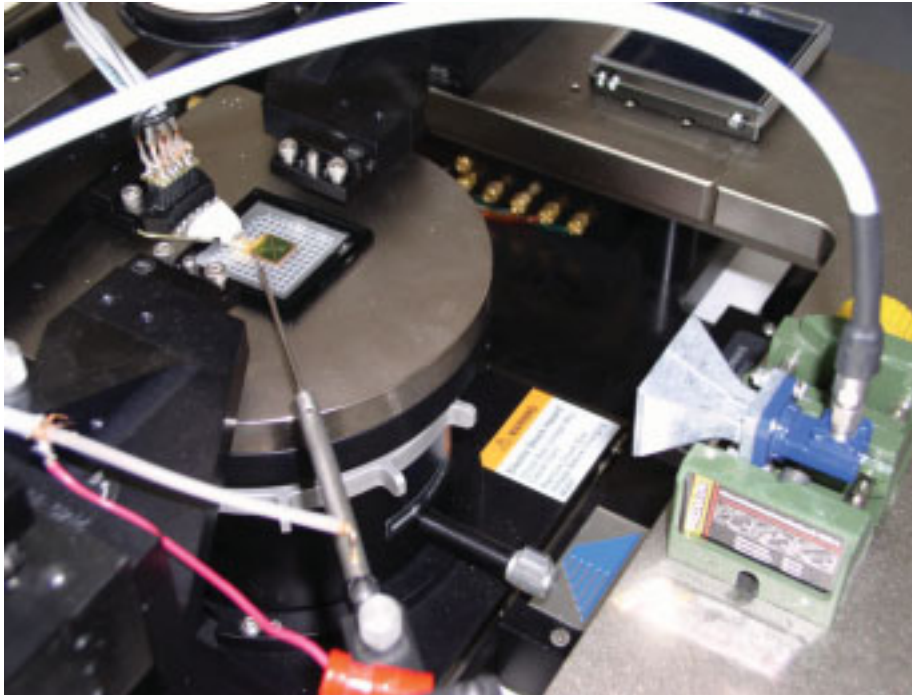


Fig. 5.14 Measurement set-up for the active antenna with horn antenna as a receiver.

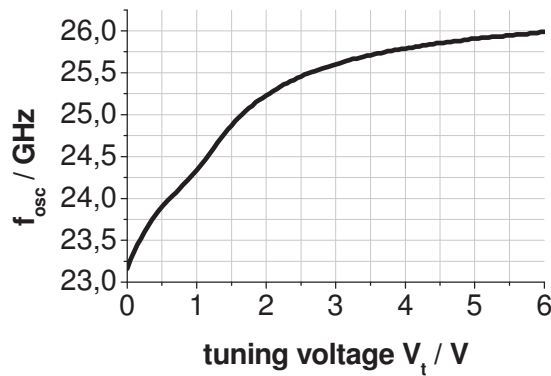


Fig. 5.15 Measured frequency at the horn-antenna receiver as a function of tuning voltage of the active antenna (set-up according to Fig. 5.14).

5.5 Conclusion

A 4-quadrant slot antenna designed for the ISM band at 24.1 GHz and based on a two-step flip-chip process is analyzed and optimized. The size and shape of the antenna makes it compact and suitable to be used in sensor nodes, for instance.

Investigations on several design issues as well as fabrication tolerances are demonstrated in order to check the functionality of the PML boundary condition (to define the surrounding open boundary condition of the antenna) as well as the internal port (in order to excite the antenna internally, needed when a structure is totally bounded by PML) which were included in the F3D software, based on FDFD method. The F3D simulation results are compared with the simulation results obtained by CST MWS as well as measurement results and the comparisons provide very good agreement with each other.

Regarding the antenna results, it is found that the slot length and height determines the resonance frequency and bandwidth of the antenna, respectively. The excitation bump position and the height of the metal block determine the matching of the antenna with the low characteristic impedance of the slot. In addition, the excitation bump position also shifts the resonance frequency. Any opening like that around the excitation bump pad let the input power to penetrate into the substrate which is trapped there due to the substrate resonances. The insertion of vias inside the substrate is necessary to suppress unwanted resonances. The efficiency, directivity and gain of the antenna are 50%, 7dBi and 4dB, respectively. Last but not least, functionality of the antenna with an integrated GaAs-HBT VCO is demonstrated.

6 Summary

PML absorbing boundary condition and internal ports are essential tools included in EM simulators in order to overcome the limitations by mesh size, open-space description and waveguide excitation. They facilitate the way towards simulating electrically large microwave structures, especially when active and/or sub-structures with considerably smaller dimensions are to be included. PML provides the open boundary condition as matched absorber and helps to keep the mesh size at a reasonable size. Internal ports allow to feed structures internally, especially when feeding otherwise (i.e. by waveguide port) is not possible, and to include lumped elements into the mesh. With the help of internal ports such structures of different dimensions can be simulated easily part by part and interfaced to network descriptions, i.e. in terms of S- and/or Z-parameters, including also active elements.

While the benefits of these tools are clear, they give rise to parasitics as well, which sometimes even outperform the advantages. In the FDFD method, where a large system of equations needs to be solved, PML deteriorates numerical condition thus corrupting the convergence behavior of the iterative solver. With this motivation the work presented here is focused on the following three areas:

1. resolving the impact of PML on the convergence of the iterative solution.
2. sorting the desired physical modes out of the unwanted ones when analysing a waveguide with layered PML walls.
3. implementing internal ports in the FDFD method and determining their parasitics.

Regarding PML, the anisotropic PML approach [18] is followed here which shows partly active characteristics (due to complex η). Numerically, this enlarges the range of the magnitudes of the elements of the system matrix. Several rows of the system matrix are affected where the ratios between the sum of the magnitudes of the non-diagonal elements and the diagonal element becomes larger than unity. This leads to numerical problems – the PML media makes the system matrix ill-conditioned so that the system shows bad convergence, i.e. the number of iterations (thereby the CPU time) increases drastically. This restricts the utilisation of the PML significantly. The convergence problems are even worse if the PML layers are overlapped at the corners and edges. The following key factors were found to circumvent the PML-related convergence problems by redefining PML regions and optimizing PML parameters:

1. Overlapping regions increase the iteration count of the equation by a factor > 15 . Our investigations show that by avoiding any overlapping, the high count of the number of iterations can be lowered very significantly; replacing overlapping corners and edges by complete PML walls (defined as non-overlapping PML walls). Several structures (e.g. patch antenna, flip-chip interconnects, spiral inductors, coupler etc) are investigated validating this concept.

2. PML cell size is the most important parameter regarding the convergence of the iterative solution. The iteration level can be lowered drastically by making the PML cell sizes the largest ones in the whole mesh.
3. The choice of the nominal reflection error (r_{th}) for the PML has a significant influence over the iteration count. On the other hand, it is very important to ensure that the absorption level of the PML approaches the given nominal reflection error. A thumb rule is developed for estimating the relative dielectric constant in the PML region, if the PML wall is inserted in a layered media, in order to calculate the nominal reflection error that is nearly equal to the absorption level of the PML wall.

Another unwanted effect occurs if PML is used as lateral boundary for waveguides or transmission lines. Then, the mode spectrum consists of physical modes and non-physical modes which are related to the PML walls. In [25] it is suggested to use the part of the power transported in the PML regions to distinguish the two types of modes, the so-called PPP value. Our investigation recalls that filtering the PML modes out by the PPP criterion may lead to the exclusion of surface wave modes. This suggests that the PPP criterion should be used carefully, which may differ from structure to structure. A careful observation following the 2D (using mode fields, PPP criterion) as well as 3D simulations (checking the coupling among the unwanted PML, box and physical modes) is needed in order to remove unnecessary modes from the calculation domain.

The implementation of internal port in the FDFD code is tried following two different approaches. In the first approach (relaxation current source), two lumped time varying charges of equal magnitudes but opposite polarities are inserted at the two nodes of the internal port. It is shown that this approach strongly excites non-physical solutions and thereby is not useful to work as an internal port. In the second approach (conduction current source) a line-current source is assumed along a path of cells between two conductors. The feasibility of this approach is checked and it is found to be accurate and very useful.

However, the advantages of the conduction current internal port do not come for free. It introduces extra magnetic fields surrounding it and thereby a parasitic inductance. It is shown that this inductance can be estimated as the inductance of a rectangular wire (L_{hm}) with a homogeneous current density at the cross section of the wire. This assumption is similar to the basic assumptions of FDFD method – where within the cells the material properties are assumed to be homogenous and changes are only allowed at the surfaces of the cells. The parasitic inductances are extracted (L_{ex}) numerically for two line structures of MS and CPW, where two internal ports are placed at the ends of the lines. A closed-form expression for the parasitic inductance is given, which allows easy calculation of its value so that it can be deembedded from the port behaviour. This is essential in using internal ports because the parasitic inductance can change the results significantly.

Internal ports represent an important tool in interfacing EM-simulations with active elements. A taper shaped HEMT structure is demonstrated as a structure of practical interest, where the internal ports are used at the gate and drain fingers. The resulting Z-matrix is used to check the current distribution at the fingers – showing how simulation results with internal

ports can be used in network simulators. It is shown that the output currents at the fingers differ significantly depending on the gate and drain impedances.

As a comprehensive example for application of PML and internal ports, a 24GHz 4-quadrant slot antenna is presented, where the slot works as magnetic dipole and each quadrant works as a horn antenna. Several design issues as well as the influences of fabrication tolerances of the slot are investigated successfully in order to check the functionality of the PML boundary condition and the internal ports. The simulations with the F3D solver based on FDFD method are compared with those obtained in FDTD method (CST MWS) as well as measurement results and the comparisons provide good agreement with each other. The antenna is realized following two step flip-chip process. The efficiency, directivity and gain of the antenna are 50%, 7dBi and 4dB respectively. The integration of a GaAs-HBT VCO in side the antenna with is demonstrated as well.

7 Appendix

7.1 FDFD Discretization

The time harmonic Maxwell's equations in source free case are given by 7.1 and 7.2, with the complex permittivity according to 7.3.

$$\oint_{\partial A} \frac{1}{\mu} \vec{B} \cdot d\vec{s} = \int_A j\omega \varepsilon \vec{E} \cdot d\vec{A} \quad (7.1)$$

$$\oint_{\partial A} \vec{E} \cdot d\vec{s} = \int_A (-j\omega \vec{B}) \cdot d\vec{A} \quad (7.2)$$

$$\varepsilon = \varepsilon_r \varepsilon_0 + \frac{\kappa}{j\omega} \quad (7.3)$$

The FDFD method deals with a boundary value problem. A rectangular box is treated as the boundary region and the box is subdivided into elementary cells by a three-dimensional non-equidistant Cartesian grid (see Fig. 1.3). Each elementary cell (Fig. 7.1) is filled with homogeneous material described by its permittivity and permeability. A change in material properties is allowed only at the surfaces of the elementary cells. The E-field components are defined at the center of the corresponding cell edges and magnetic fields are defined at the center of each cell surfaces. If the numbers of cells in x, y and z directions are n_x , n_y and n_z , then the total number of cells is $n_x \times n_y \times n_z$. Each elementary cell is identified by an index of (i, j, k) .

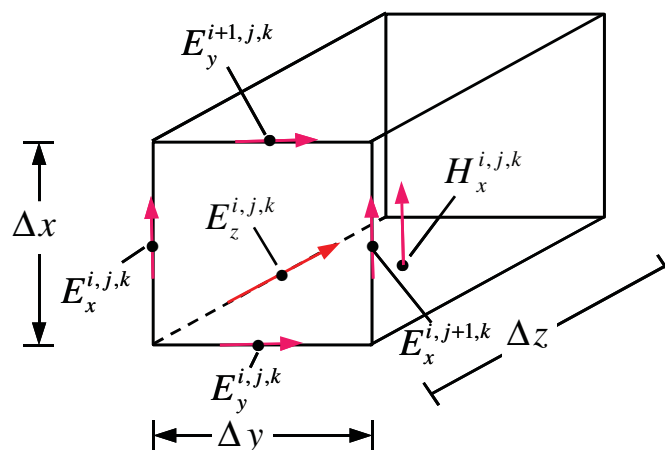


Fig. 7.1 FD elementary cell and the assignment of the field quantities. The elementary cell is identified by an index of (i, j, k) .

$$i = 1 \dots n_x, j = 1 \dots n_y \text{ and } k = 1 \dots n_z$$

n_x , n_y and n_z are the number of cells in x, y and z directions respectively.

The discretizations of the analytical equations are carried out by fitting the Maxwell's analytical equations in the Cartesian grid system. The line integral of tangential vectors, here for example E-fields, are approximated by multiplying the value at the center point of the corresponding edge with the line length as given by 7.4.

$$\oint \vec{E} \cdot d\vec{s} \approx E_x^{i,j,k} \left(\frac{\Delta x}{2}\right) \cdot \Delta x + E_y^{i,j,k} \left(\frac{\Delta y}{2}\right) \cdot \Delta y - E_x^{i,j+1,k} \left(\frac{\Delta x}{2}\right) \cdot \Delta x - E_y^{i+1,j,k} \left(\frac{\Delta y}{2}\right) \cdot \Delta y \quad (7.4)$$

In the same way, the surface integral is represented by the multiplication of the value of a field component in the center of the surface with the surface area, e.g. given by 7.5.

$$\iint_A \vec{H} \cdot d\vec{A} = \int_0^{\Delta y} \int_0^{\Delta z} H_x^{i,j,k} \left(\frac{\Delta y}{2}, \frac{\Delta z}{2}\right) \cdot dy \cdot dz \approx H_x^{i,j,k} \left(\frac{\Delta y}{2}, \frac{\Delta z}{2}\right) \cdot \Delta y \cdot \Delta z \quad (7.5)$$

[7, 8] shows how the discretized form of Maxwell's equation as well as the wave equation given by 7.6 can be derived following the examples of 7.4 and 7.5. The discretized wave equation of 7.6 corresponds to the analytical form given by 7.7. Here A is a canonical matrix where as D 's are diagonal matrices that contain the information on all dimensions and material properties of each cell. \vec{e} is a vector that contains all the electric field components in x, y and z directions for each cell inside the rectangular enclosure containing the structure under test.

$$(A^T D_{s/\mu} D_A^{-1} A D_s - k_0^2 D_{A\epsilon}) \vec{e} = 0 \quad (7.6)$$

$$\nabla^2 \vec{E} + \omega^2 \epsilon \mu \vec{E} = 0 \quad (7.7)$$

Equation 7.6 represents a boundary value problem. Suitable sources can be added through waveguide ports at the boundaries or by inserting internal ports (conduction or relaxation current source), which results in a non-zero right-hand side in 7.6.

7.2 Excitation by Relaxation Current (Internal Port) Source

Time varying charges are used in order to excite the structure internally by a relaxation current internal port. An input current I_0 (e.g. 1 mA) is converted to the time varying charges as given by 7.8 and 7.9. The excitation is carried out by inserting two lumped charges of equal magnitudes but of opposite polarities and thereby using the relaxation current between the charges.

$$I_0 = \oiint \vec{J}_s \cdot d\vec{s} = -\frac{\partial}{\partial t} Q = -j\omega Q \quad (7.8)$$

$$Q = \frac{I_0}{-j\omega} \quad (7.9)$$

For zero static space charge, equation (7.10) must hold, which is true only for dielectric regions, because charges may exist in the metallic walls and inlays.

$$\nabla \cdot \epsilon \vec{E} = \rho = 0 \cong \oint \epsilon \vec{E} \cdot d\vec{A} = 0 \quad (7.10)$$

Now the time varying input charge (Q) is added in equation 7.10 and it results in equation 7.11.

$$\oint \epsilon \vec{E} \cdot d\vec{A} = Q \quad (7.11)$$

Following the FDFD discretization procedure 7.11 is converted to the matrix equation given by 7.12 where \vec{q} is a vector containing information of charges at each cell. In [6, 7] it is shown that all the static charges from the dielectric region are removed in order to avoid irrotational static fields and improve the convergence – this corresponds to $\vec{q} = 0$. On the other hand, the time varying input charges are added at the corners of cells (e.g. at the centers of the corresponding dual cells [8]) of interest. For each internal port there will be two cells assigned with time varying charge ($Q \neq 0$). All other cells except those which include metal walls/plates etc. are free of static charges ($Q = 0$). Fig. 7.2 shows an example of assigning a time varying charge at a particular cell. If only one internal port is treated, for example, the vector \vec{q} should look like 7.13, where Q_1 and Q_2 are the input charges at the two nodes of the internal port.

$$BD_{A\epsilon} \vec{e} = \begin{pmatrix} \vec{q} \\ \epsilon_0 \end{pmatrix} \quad (7.12)$$

$$\vec{q} = \begin{pmatrix} 0 \\ \dots \\ Q_1 = Q \\ 0 \\ 0 \\ \dots \\ Q_2 = -Q \\ \dots \\ \dots \\ 0 \end{pmatrix}_{n_{xyz} \times n_{xyz}}, \quad Q = \frac{I_0}{-j\omega} \quad (7.13)$$

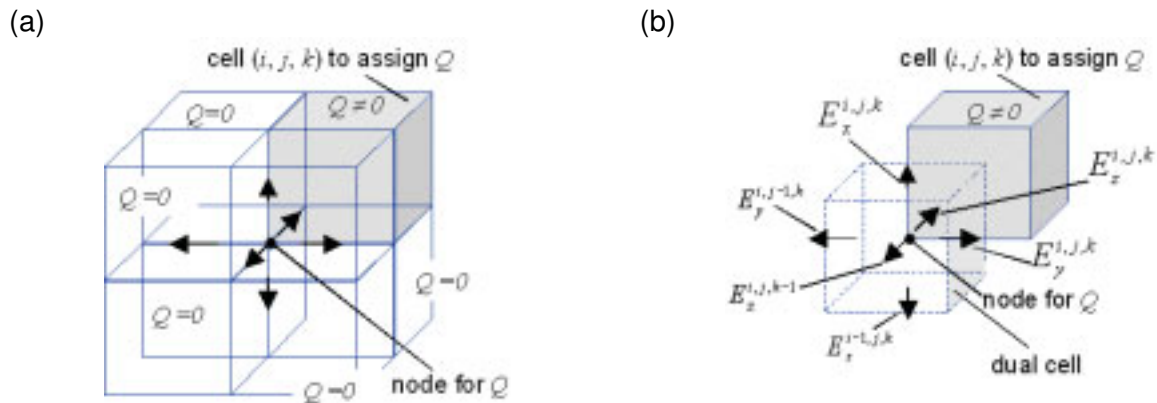


Fig. 7.2 Assignment of time varying charge Q in an FDFD cell (a). All other non metal cells are charge (static) free. The assignment of the electric field components surrounding the node where Q is assigned (b).

The wave equation in continuous space given by 7.7 turns to 7.14 when space charges ρ are included assuming neither conduction loss nor impressed current. Equation 7.12 is converted to 7.15 which represents the integral form of the right-hand side of equation 7.14. Again the diagonal matrices (D 's) contain information on dimensional and material properties of the structure under consideration and B is canonical matrix [7, 8]. The Finite difference discretized wave equation in matrix form corresponding to the analytical wave equation of 7.14 is given by 7.16. After some mathematic manipulation, 7.16 is converted to the symmetric one given by 7.17, where the vector \vec{r}_r stands for the relaxation current internal port source. M_1 and M_3 correspond to rotational and irrotational (static) electric fields respectively. The dimensions and form of the vector \vec{r}_r is given by 7.18 where p is the index of the vector components.

$$\nabla^2 \vec{E} + \omega^2 \epsilon \mu \vec{E} = \frac{1}{\epsilon} \nabla (\nabla \cdot \epsilon \vec{E}) = \frac{1}{\epsilon} \nabla \rho \quad (7.14)$$

$$D_s^{-1} D_{A\epsilon} B^T D_{v\epsilon\epsilon}^{-1} B D_{A\epsilon} \vec{e} = D_s^{-1} D_{A\epsilon} B^T D_{v\epsilon\epsilon}^{-1} \begin{pmatrix} \vec{q} \\ \epsilon_0 \end{pmatrix} \quad (7.15)$$

$$(A^T D_{s/\mu} D_A^{-1} A D_s - k_0^2 D_{A\epsilon} + D_s^{-1} D_{A\epsilon} B^T D_{v\epsilon\epsilon}^{-1} B D_{A\epsilon}) \vec{e} = D_s^{-1} D_{A\epsilon} B^T D_{v\epsilon\epsilon}^{-1} \begin{pmatrix} \vec{q} \\ \epsilon_0 \end{pmatrix} \quad (7.16)$$

$$M \vec{e} = (M_1 + M_2 + M_3) \vec{e} = \vec{r}_r \quad (7.17)$$

where,

$$M_1 = \left(D_s^{\frac{1}{2}} A^T D_{s/\mu} D_A^{-1} A D_s^{\frac{1}{2}} \right) D_s^{\frac{1}{2}}, \quad M_2 = \left(-D_s^{\frac{1}{2}} k_0^2 D_{A\epsilon} D_s^{-\frac{1}{2}} \right) D_s^{\frac{1}{2}}, \quad M_3 = \left(D_s^{-\frac{1}{2}} D_{A\epsilon} B^T D_{v\epsilon\epsilon}^{-1} B D_{A\epsilon} D_s^{-\frac{1}{2}} \right) D_s^{\frac{1}{2}}$$

and

$$\vec{r}_r = D_s^{-\frac{1}{2}} D_{A\epsilon} B^T D_{v\epsilon\epsilon}^{-1} \begin{pmatrix} \vec{q} \\ \epsilon_0 \end{pmatrix}$$

$$\begin{matrix}
 D_s^{-\frac{1}{2}} \cdot & D_{Ae} \cdot & B^T \cdot & D_{v\epsilon\epsilon}^{-1} \cdot & \vec{q} & = & \vec{r}_r = & \left(\begin{matrix} \vec{r}_{rx} = \begin{pmatrix} r_{rx} \\ \vdots \\ r_{rx} \end{pmatrix}_{p=1\dots n} \\ \vec{r}_{ry} = \begin{pmatrix} r_{ry} \\ \vdots \\ r_{ry} \end{pmatrix}_{p=n+1\dots 2n} \\ \vec{r}_{rz} = \begin{pmatrix} r_{rz} \\ \vdots \\ r_{rz} \end{pmatrix}_{p=2n+1\dots 3n} \end{matrix} \right)_{3n \times 1}
 \end{matrix} \quad (7.18)$$

The assignment of the time varying charge Q as shown in Fig. 7.2 is accomplished by assigning the components of \vec{r}_r vector of 7.18 at the centres of the surfaces of the corresponding dual cells which contain the nodes of the internal ports. Fig. 7.3 shows such an assignment at the m^{th} dual cell which is to contain an internal port node for example. Assignments in x (a) and y (b) directions are shown and the same is also true for Z direction. The charge Q is assigned as the divergence of the electric fields at the centers of the corresponding cell edges where the electric fields are also defined in FDFD scheme.

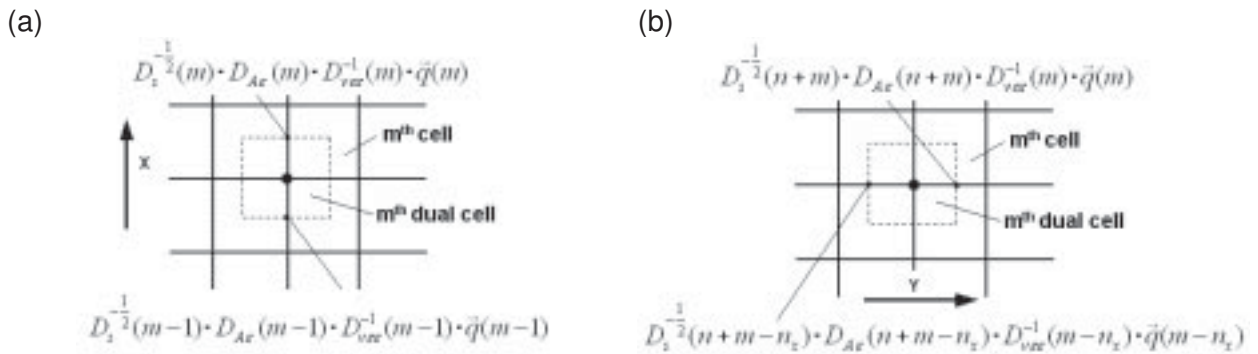


Fig. 7.3 FD elementary cell and the assignment of the fields quantities. The elementary cell is identified by an index of (i, j, k) .

$$m = 1 + (i-1) \cdot M_u + (j-1) \cdot M_v + (k-1) \cdot M_w$$

$$M_u = 1, M_v = n_x, M_w = n_x \cdot n_y,$$

$$i = 1 \dots n_x, j = 1 \dots n_y \text{ and } k = 1 \dots n_z$$

$$n = n_x \cdot n_y \cdot n_z$$

n_x, n_y and n_z are the number of cells in x, y and z directions respectively.

$q(m)$: m^{th} component of the \vec{q} vector etc.

$D_s(m)$: m^{th} component of the diagonal matrix D_s etc.

Now if one internal port is treated and the two nodes of the port are contained in the dual cells of m_1 and m_2 , then the sub vectors of \vec{r}_{rx} , \vec{r}_{ry} and \vec{r}_{rz} look like 7.19.1-3. Both m_1 and m_2 are calculated in the same way as the calculation of m in Fig. 7.3. The vector \vec{r}_r can have maximum 12 nonzero components per internal port.

$$\begin{pmatrix} r_{rx} \end{pmatrix}_{n \times 1} = \begin{pmatrix} -D_s^{-\frac{1}{2}}(m_1-1)D_{A\epsilon}(m_1-1)D_{v\epsilon\epsilon}^{-1}(m_1)\vec{q}(m_1) & \leftarrow p = m_1 - 1 \\ D_s^{-\frac{1}{2}}(m_1)D_{A\epsilon}(m_1)D_{v\epsilon\epsilon}^{-1}(m_1)\vec{q}(m_1) & \leftarrow p = m_1 \\ -D_s^{-\frac{1}{2}}(m_2-1)D_{A\epsilon}(m_2-1)D_{v\epsilon\epsilon}^{-1}(m_2)\vec{q}(m_2) & \leftarrow p = m_2 - 1 \\ D_s^{-\frac{1}{2}}(m_2)D_{A\epsilon}(m_2)D_{v\epsilon\epsilon}^{-1}(m_2)\vec{q}(m_2) & \leftarrow p = m_2 \end{pmatrix} \quad (7.19.1)$$

$$\begin{pmatrix} r_{ry} \end{pmatrix}_{n \times 1} = \begin{pmatrix} -D_s^{-\frac{1}{2}}(n+m_1-n_x)D_{A\epsilon}(n+m_1-n_x)D_{v\epsilon\epsilon}^{-1}(m_1)\vec{q}(m_1) & \leftarrow p = n + m_1 - n_x \\ D_s^{-\frac{1}{2}}(n+m_1)D_{A\epsilon}(n+m_1)D_{v\epsilon\epsilon}^{-1}(m_1)\vec{q}(m_1) & \leftarrow p = n + m_1 \\ -D_s^{-\frac{1}{2}}(n+m_2-n_x)D_{A\epsilon}(n+m_2-n_x)D_{v\epsilon\epsilon}^{-1}(m_2)\vec{q}(m_2) & \leftarrow p = n + m_2 - n_x \\ D_s^{-\frac{1}{2}}(n+m_2)D_{A\epsilon}(n+m_2)D_{v\epsilon\epsilon}^{-1}(m_2)\vec{q}(m_2) & \leftarrow p = n + m_2 \end{pmatrix} \quad (7.19.2)$$

$$\left(\begin{array}{c} r_{\vec{r}_c} \\ \end{array} \right)_{n \times 1} = \left(\begin{array}{c} -D_s^{-\frac{1}{2}}(2n+m_1-n_{xy})D_{A\epsilon}(2n+m_1-n_{xy})D_{v\epsilon\epsilon}^{-1}(m_1)\vec{q}(m_1) \\ D_s^{-\frac{1}{2}}(2n+m_1)D_{A\epsilon}(2n+m_1)D_{v\epsilon\epsilon}^{-1}(m_1)\vec{q}(m_1) \\ -D_s^{-\frac{1}{2}}(2n+m_2-n_{xy})D_{A\epsilon}(2n+m_2-n_{xy})D_{v\epsilon\epsilon}^{-1}(m_2)\vec{q}(m_2) \\ D_s^{-\frac{1}{2}}(2n+m_2)D_{A\epsilon}(2n+m_2)D_{v\epsilon\epsilon}^{-1}(m_2)\vec{q}(m_2) \\ \end{array} \right) \begin{array}{l} \leftarrow p = 2n + m_1 - n_{xy} \\ \leftarrow p = 2n + m_1 \\ \leftarrow p = 2n + m_2 - n_{xy} \\ \leftarrow p = 2n + m_2 \end{array}$$

(7.19.3)

7.3 Excitation by Conduction Current (Internal Port) Source

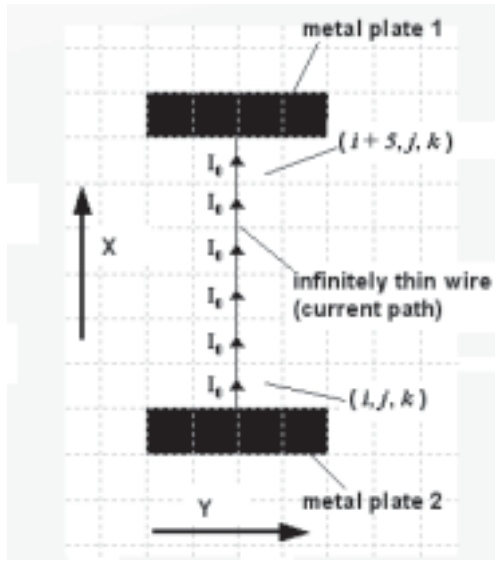
In order to add a conduction current source, equation 7.20 must be used instead of equation 7.1, where \vec{J}_e stands for a conduction current density. In this case equation 7.17 will turn to 7.21, where \vec{r}_c refers to the conduction current source. The form and components of \vec{r}_c will be explained by examples below.

$$\oint_{\partial A} \frac{1}{\mu} \vec{B} \cdot d\vec{s} = \int_A j\omega\epsilon\vec{E} \cdot d\vec{A} + \int_A \vec{J}_e \cdot d\vec{A} \quad (7.20)$$

$$M\vec{e} = (M_1 + M_2 + M_3)\vec{e} = \vec{r}_r + \vec{r}_c \quad (7.21)$$

In FDFD mesh conduction current (internal port) source is accomplished by inserting a line current along the cell edges. An arbitrary but continuous path of cells is chosen between the metal plates to define the rectangular wire and the current I_0 is assigned at the centers of the cell edges in order to form a continuous current path. The path can be straight, e.g. directed in x direction as shown in Fig 7.4.a or oriented in different directions, e.g. in x and y directions as given in Fig. 7.4.b.

(a)



(b)

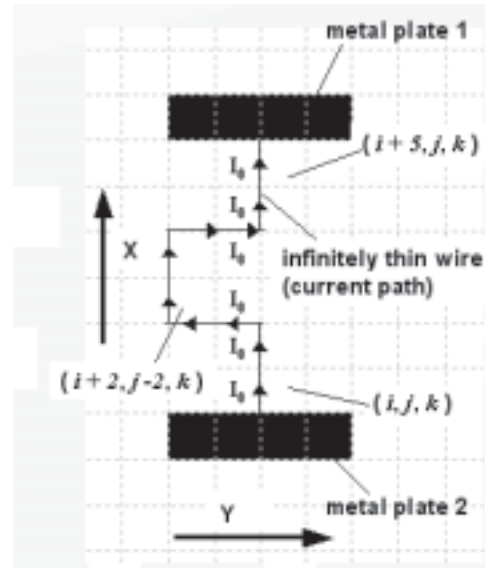


Fig. 7.4 Assignment of the conduction current source in FDFD mesh.

$$\begin{aligned}
 m(i, j, k) &= 1 + (i-1) \cdot M_u + (j-1) \cdot M_v + (k-1) \cdot M_w \text{ etc.} \\
 m(i+5, j, k) &= 1 + (i+5-1) \cdot M_u + (j-1) \cdot M_v + (k-1) \cdot M_w \text{ etc.} \\
 M_u &= 1, M_v = n_x, M_w = n_x \cdot n_y, \\
 i &= 1 \dots n_x, j = 1 \dots n_y \text{ and } k = 1 \dots n_z \\
 n &= n_x \cdot n_y \cdot n_z \\
 n_x, n_y \text{ and } n_z &\text{ are the number of cells in x, y and z directions respectively.}
 \end{aligned}$$

For the example of Fig. 7.4.a the conduction current source vector will look like as given by equation of 7.22. In this case only the vector components with indices from $m(i, j, k)$ to $m(i+5, j, k)$ possess nonzero values. In the same way the conduction current source vector for the example of Fig. 7.4.b is given by equation 7.23. Again only the nonzero components with respect to the indices are shown. In this way any arbitrary conduction current path can be achieved also in the z direction, which is not shown here for simplicity.

$$\vec{r}_c = \begin{pmatrix} \vec{r}_{cx} \\ \vec{r}_{cy} \\ \vec{r}_{cz} \end{pmatrix}_{3n \times 1}, \quad \vec{r}_{cx} = \begin{pmatrix} I_{m(i,j,k)} = I \\ I_{m(i+1,j,k)} = I \\ I_{m(i+2,j,k)} = I \\ I_{m(i+3,j,k)} = I \\ I_{m(i+4,j,k)} = I \\ I_{m(i+5,j,k)} = I \end{pmatrix}_{n \times 1}, \quad \vec{r}_{cy} = \begin{pmatrix} 0 \end{pmatrix}_{n \times 1}, \quad \vec{r}_{cz} = \begin{pmatrix} 0 \end{pmatrix}_{n \times 1}, \quad I = -j2\omega\mu I_0 \tag{7.22}$$

$$\vec{r}_c = \begin{pmatrix} \vec{r}_{cx} \\ \vec{r}_{cy} \\ \vec{r}_{cz} \end{pmatrix}_{3n \times 1}, \quad \vec{r}_{cx} = \begin{pmatrix} I_{m(i,j,k)} = I \\ I_{m(i+1,j,k)} = I \\ I_{m(i+2,j-2,k)} = I \\ I_{m(i+3,j-2,k)} = I \\ I_{m(i+4,j,k)} = I \\ I_{m(i+5,j,k)} = I \end{pmatrix}_{n \times 1}, \quad \vec{r}_{cy} = \begin{pmatrix} I_{m(i+2,j-2,k)} = -I \\ I_{m(i+2,j-1,k)} = -I \\ I_{m(i+4,j-2,k)} = I \\ I_{m(i+4,j-1,k)} = I \end{pmatrix}_{n \times 1}, \quad \vec{r}_{cz} = \begin{pmatrix} 0 \end{pmatrix}_{n \times 1}, \quad I = -j2\omega\mu I_0 \quad (7.23)$$

If more than one internal port is used, the procedure is same. For each internal port an arbitrary current path is chosen with an arbitrary current (i.e. I_0 can be different for different ports) flowing through it. Then the vectors of each internal port are added to get the resulting vector that refers all the conduction current sources as given by 7.24.

$$\vec{r}_c = \begin{pmatrix} \vec{r}_{cx} \\ \vec{r}_{cy} \\ \vec{r}_{cz} \end{pmatrix}_{3n \times 1}^{port 1} + \begin{pmatrix} \vec{r}_{cx} \\ \vec{r}_{cy} \\ \vec{r}_{cz} \end{pmatrix}_{3n \times 1}^{port 2} + \begin{pmatrix} \vec{r}_{cx} \\ \vec{r}_{cy} \\ \vec{r}_{cz} \end{pmatrix}_{3n \times 1}^{port 3} + \begin{pmatrix} \vec{r}_{cx} \\ \vec{r}_{cy} \\ \vec{r}_{cz} \end{pmatrix}_{3n \times 1}^{port 4} + \dots \quad (7.24)$$

7.4 Conduction Current Internal Ports as Lumped Elements

If p numbers of conduction current internal ports are used, assuming that no other sources exist, then a 3D simulation results in a Z -matrix of dimension $p \times p$. The currents through the internal ports are known as these are the input currents. After the 3D simulation the electric fields at the center of each cell edge is known. So the voltages across the internal ports are calculated by summing up the products of the respective electric fields and cell sizes along the continuous current paths of the corresponding internal ports. In order to calculate all the components of the Z -matrix, the structure under test must be excited p times, where in each excitation the input currents must be linearly independent from those of the other excitations. For the t^{th} ($t = 1 \dots p$) excitation the current voltage relationship looks like the equation 7.25. v^t and i^t are the vectors which contain the calculated voltages across the internal ports and input current through the internal ports respectively for the t^{th} excitation. V_p^t and I_p^t are the voltage and current of the p^{th} ($p = 1 \dots p$) port of the t^{th} excitation. After the p number of excitations, there will be p number of linearly independent equations such as 7.25. After some mathematical manipulations of these p number of equations, all the components of the Z -matrix can be found by 7.26, where s stands for the row index in the Z -matrix and the vector z^s contains all the components of the Z -matrix in the s^{th} row. In $(\)_i^s$ matrix the s^{th} row contains the input currents of t^{th} excitation and all other components are equal to zero.

$$\vec{v}^t = Z \cdot \vec{i}^t \Rightarrow \begin{pmatrix} V_1^t \\ V_2^t \\ \cdot \\ \cdot \\ V_p^t \end{pmatrix}_{p \times 1} = Z \cdot \begin{pmatrix} I_1^t \\ I_2^t \\ \cdot \\ \cdot \\ I_p^t \end{pmatrix} \quad (7.25)$$

$$\begin{pmatrix} ()_1^1 & ()_1^2 & \cdot & \cdot & \cdot & ()_1^p \\ \cdot & \cdot & \cdot & \cdot & \cdot & \cdot \\ \cdot & \cdot & \cdot & ()_t^s & \cdot & \cdot \\ \cdot & \cdot & \cdot & \cdot & \cdot & \cdot \\ \cdot & \cdot & \cdot & \cdot & \cdot & \cdot \\ ()_p^1 & ()_p^2 & \cdot & \cdot & \cdot & ()_p^p \end{pmatrix}_{(p \times p) \times (p \times p)} \cdot \begin{pmatrix} \bar{z}^1 \\ \bar{z}^2 \\ \cdot \\ \cdot \\ \bar{z}^s \\ \cdot \\ \bar{z}^p \end{pmatrix}_{(p \times p) \times 1} = \begin{pmatrix} \bar{v}^1 \\ \bar{v}^2 \\ \cdot \\ \bar{v}^t \\ \cdot \\ \bar{v}^p \end{pmatrix}_{(p \times p) \times 1} \quad (7.26)$$

where,

$$()_t^s = \begin{pmatrix} 0 & 0 & 0 & 0 & \cdot & 0 & 0 \\ \cdot & \cdot & \cdot & \cdot & \cdot & \cdot & \cdot \\ 0 & 0 & 0 & 0 & \cdot & \cdot & 0 \\ I_1^t & I_2^t & I_3^t & I_4^t & \cdot & I_{p-1}^t & I_p^t \\ 0 & 0 & 0 & 0 & \cdot & \cdot & 0 \\ \cdot & \cdot & \cdot & \cdot & \cdot & \cdot & \cdot \\ 0 & 0 & 0 & 0 & \cdot & 0 & 0 \end{pmatrix}_{p \times p} \Leftarrow s^{th} \text{ row}, \quad \bar{z}^s = \begin{pmatrix} Z_{s1} \\ Z_{s2} \\ \cdot \\ Z_{ss} \\ \cdot \\ Z_{sp} \end{pmatrix}_{p \times 1}$$

It is possible to eliminate some of the internal ports and thus to reduce the order of Z -matrix, if these internal ports are converted (i.e. connected) to lumped elements. If v ($v < p$) number of internal ports are to be converted into lumped elements, then a matrix equation of 7.27 can be formed in such a way that \vec{v}_u and \vec{v}_v contain the voltages across the rest of the internal ports (u number, $u = p-v$) and the voltages across the lumped elements respectively. Same way \vec{i}_u and \vec{i}_v contain the currents through the rest of the internal ports and through the lumped elements. The Z -matrix is divided into sub matrices correspondingly. Equation 7.27 can be broken into two equations of 7.28 and 7.29. Equation 7.30 represents the voltage-current relationship of the lumped elements, where R is a diagonal matrix containing the impedance values of the lumped elements. Combining 7.29 and 7.30 results in 7.31. From 7.31 and 7.28 the new Z -matrix (Z^{new}) can be found by replacing \vec{i}_v , given by 7.32. Z^{new} represents the Z -matrix of the rest of the internal ports while taking the effect of the lumped elements into account.

$$\begin{pmatrix} \vec{v}_u \\ \vec{v}_v \end{pmatrix}_{p \times 1} = Z \cdot \begin{pmatrix} \vec{i}_u \\ \vec{i}_v \end{pmatrix}_{p \times 1} = \begin{pmatrix} (Z_{11})_{u \times u} & (Z_{12})_{u \times v} \\ (Z_{21})_{v \times u} & (Z_{22})_{v \times v} \end{pmatrix}_{p \times p} \cdot \begin{pmatrix} \vec{i}_u \\ \vec{i}_v \end{pmatrix}_{p \times 1} \quad (7.27)$$

$$\vec{v}_u = (Z_{11})_{u \times u} \cdot \vec{i}_u + (Z_{12})_{u \times v} \cdot \vec{i}_v \quad (7.28)$$

$$\vec{v}_v = (Z_{21})_{v \times u} \cdot \vec{i}_u + (Z_{22})_{v \times v} \cdot \vec{i}_v \quad (7.29)$$

$$\vec{v}_v = -(R)_{v \times v} \cdot \vec{i}_v \quad (7.30)$$

$$\vec{i}_v = -((R)_{v \times v} + (Z_{22})_{v \times v})^{-1} \cdot (Z_{21})_{v \times u} \cdot \vec{i}_u \quad (7.31)$$

$$(Z)_{u \times u}^{new} = \frac{\vec{v}_u}{\vec{i}_u} = (Z_{11})_{u \times u} - (Z_{12})_{u \times v} \cdot ((R)_{v \times v} + (Z_{22})_{v \times v})^{-1} \cdot (Z_{21})_{v \times u} \quad (7.32)$$

7.5 Deembedding Conduction Current Internal Port Parasitics

Each conduction current internal port possesses parasitic inductances, since the current flowing through the internal port generates magnetic fields which are not present there when a structure is excited by any current source at two certain points of the structure. The procedure of deembedding of this parasitic inductance is shown in Fig. 7.5. After 3D calculation, the evolved Z -matrix (Z_{total}) is a function of Z_{par} and Z_{DUT} , where Z_{par} contains the parasitics of all the internal ports and Z_{DUT} is the desired Z -matrix free of parasitic influences. Z_{total} is defined by 7.33, where n is the number of internal ports.

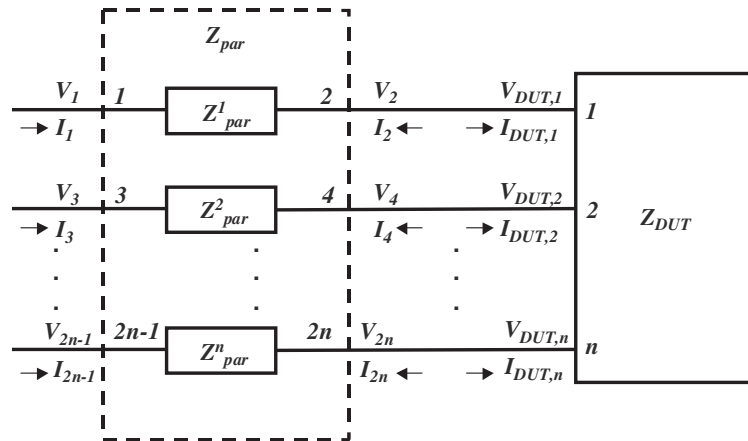


Fig. 7.5 Deembedding of internal port parasitics when n numbers of internal ports are treated.

Z_{DUT} is the desired Z -matrix after deembedding. $I_1, I_3, \dots, I_{2n-1}$ are the input currents flowing through the internal ports, where as $V_1, V_3, \dots, V_{2n-1}$ are the voltages calculated across the internal ports (source voltages) after the 3D simulation. Z_{par} matrix represents the parasitic impedances of all the internal ports. Z_{par}^n stands for the parasitic impedance matrix of the n^{th} internal port. $I_{DUT,n}$ is the current which enters the device under test out of the n^{th} internal port after deembedding. $V_{DUT,n}$ is the voltage across the two nodes of the internal port after deembedding (excluding the parasitics of the internal ports).

$$Z_{total} = \vec{v}_1 \cdot \vec{i}_1^{-1} \quad (7.33)$$

where,

$$\vec{i}_1 = \begin{pmatrix} I_1 \\ I_3 \\ I_5 \\ \cdot \\ I_{2n-1} \end{pmatrix}_{n \times 1}, \quad \vec{v}_1 = \begin{pmatrix} V_1 \\ V_3 \\ V_5 \\ \cdot \\ V_{2n-1} \end{pmatrix}_{n \times 1}$$

Z_{par} is defined by 7.34. Z_{par}^i ($i = 1 \dots n$) represents the impedances of a two port network. So the voltages and currents of these two port networks can be related by 7.35, where Z_{par}^a is just another arrangement of Z_{par} . Again Z_{par}^a can be divided into sub matrices as given by 7.36.

$$Z_{par} = \begin{pmatrix} Z_{par}^1 & 0 & 0 & \cdot & \cdot & 0 & 0 \\ 0 & Z_{par}^2 & 0 & \cdot & \cdot & \cdot & 0 \\ 0 & 0 & \cdot & \cdot & \cdot & \cdot & \cdot \\ \cdot & \cdot & \cdot & Z_{par}^i & \cdot & \cdot & \cdot \\ \cdot & \cdot & \cdot & \cdot & \cdot & 0 & \cdot \\ 0 & \cdot & \cdot & \cdot & 0 & Z_{par}^{n-1} & 0 \\ 0 & 0 & \cdot & \cdot & \cdot & 0 & Z_{par}^n \end{pmatrix}_{2n \times 2n} \quad (7.34)$$

where,

$$Z_{par}^i = \begin{pmatrix} Z_{2i-1,2i-1} & Z_{2i-1,2i} \\ Z_{2i,2i-1} & Z_{2i,2i} \end{pmatrix}, \quad e.g. \Rightarrow Z_{par}^1 = \begin{pmatrix} Z_{1,1} & Z_{1,2} \\ Z_{2,1} & Z_{2,2} \end{pmatrix}$$

$$\begin{pmatrix} V_1 \\ V_2 \\ V_3 \\ V_4 \\ \cdot \\ V_{2n-1} \\ V_{2n} \end{pmatrix}_{2n \times 1} = Z_{par} \cdot \begin{pmatrix} I_1 \\ I_2 \\ I_3 \\ I_4 \\ \cdot \\ I_{2n-1} \\ I_{2n} \end{pmatrix}_{2n \times 1} \Rightarrow \begin{pmatrix} V_1 \\ V_3 \\ \cdot \\ V_{2n-1} \\ V_2 \\ V_4 \\ \cdot \\ V_{2n} \end{pmatrix}_{2n \times 1} = Z_{par}^a \cdot \begin{pmatrix} I_1 \\ I_3 \\ \cdot \\ I_{2n-1} \\ I_2 \\ I_4 \\ \cdot \\ I_{2n} \end{pmatrix}_{2n \times 1} \quad (7.35)$$

$$\begin{pmatrix} \vec{v}_1 \\ \vec{v}_2 \end{pmatrix}_{2n \times 1} = Z_{par}^a \cdot \begin{pmatrix} \vec{i}_1 \\ \vec{i}_2 \end{pmatrix}_{2n \times 1} = \begin{pmatrix} Z_{11}^a & Z_{12}^a \\ Z_{21}^a & Z_{22}^a \end{pmatrix}_{2n \times 2n} \cdot \begin{pmatrix} \vec{i}_1 \\ \vec{i}_2 \end{pmatrix}_{2n \times 1} \quad (7.36)$$

where,

$$\vec{i}_1 = \begin{pmatrix} I_1 \\ I_3 \\ I_5 \\ \vdots \\ I_{2n-1} \end{pmatrix}_{n \times 1}, \quad \vec{v}_1 = \begin{pmatrix} V_1 \\ V_3 \\ V_5 \\ \vdots \\ V_{2n-1} \end{pmatrix}_{n \times 1}, \quad \vec{i}_2 = \begin{pmatrix} I_2 \\ I_4 \\ I_6 \\ \vdots \\ I_{2n} \end{pmatrix}_{n \times 1} \quad \text{and} \quad \vec{v}_2 = \begin{pmatrix} V_2 \\ V_4 \\ V_6 \\ \vdots \\ V_{2n} \end{pmatrix}_{n \times 1}$$

From Fig. 7.5 it is clear that V_{2n} and $V_{DUT,n}$ are equal and I_{2n} and $I_{DUT,n}$ are also equal but opposite in direction. Z_{DUT} can be related to the vectors of \vec{v}_2 and \vec{i}_2 by the equations of 3.37 and 7.38. Through some mathematical manipulations between 7.36 and 7.38, equation for Z_{DUT} can be derived as given by 7.39.

$$\begin{pmatrix} V_{DUT,1} \\ V_{DUT,2} \\ V_{DUT,3} \\ \vdots \\ V_{DUT,n} \end{pmatrix}_{n \times 1} = Z_{DUT} \cdot \begin{pmatrix} I_{DUT,1} \\ I_{DUT,2} \\ I_{DUT,3} \\ \vdots \\ I_{DUT,n} \end{pmatrix}_{n \times 1} \Rightarrow \begin{pmatrix} V_{DUT,1} = V_2 \\ V_{DUT,2} = V_4 \\ V_{DUT,3} = V_6 \\ \vdots \\ V_{DUT,n} = V_{2n} \end{pmatrix}_{n \times 1} = Z_{DUT} \cdot \begin{pmatrix} I_{DUT,1} = -I_2 \\ I_{DUT,2} = -I_4 \\ I_{DUT,3} = -I_6 \\ \vdots \\ I_{DUT,n} = -I_{2n} \end{pmatrix}_{n \times 1} \quad (7.37)$$

$$\begin{pmatrix} V_2 \\ V_4 \\ V_6 \\ \vdots \\ V_{2n} \end{pmatrix}_{n \times 1} = -Z_{DUT} \cdot \begin{pmatrix} I_2 \\ I_4 \\ I_6 \\ \vdots \\ I_{2n} \end{pmatrix}_{n \times 1} \Rightarrow \vec{v}_2 = -Z_{DUT} \cdot \vec{i}_2 \quad (7.38)$$

$$Z_{DUT} = \left(-Z_{12}^a{}^{-1} (Z_{total} - Z_{11}^a) \cdot Z_{21}^a{}^{-1} \right)^{-1} - Z_{22}^a \quad (7.39)$$

The two port network of Z_{par}^i ($i = 1 \dots n$) is shown in Fig. 7.6. The components of Z_{par}^i are defined by 7.40 and 7.41.

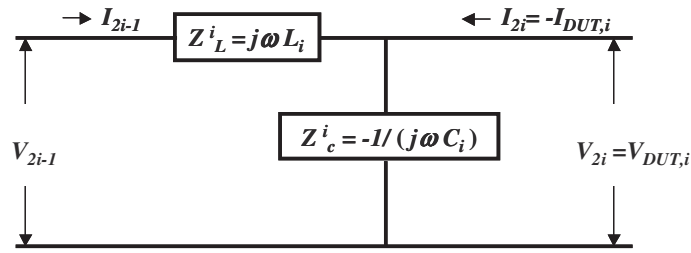


Fig. 7.6 Parasitic impedances of an (i^{th}) internal port. L_i is the inductance of the internal port and C_i stands for the end effect capacitance which is not part of the internal port parasitics, rather accounts for the fringing fields, i.e. true only for the special case treated here.

$$Z_{2i-1,2i-1} = Z_L^i + Z_C^i \tag{7.40}$$

$$Z_{2i-1,2i} = Z_{2i,2i-1} = Z_{2i,2i} = Z_C^i \tag{7.41}$$

7.6 Excitation by Waveguide Ports

The excitation procedure by waveguide ports together with extraction of modes in 2D calculation and S-parameter calculation following the 3D calculation is given in details in [5, 10]. For the completeness, the 2D and 3D excitation procedures will be shown here in brief with the help of a simple example of two waveguide ports as shown in Fig. 7.7. Let us assume for simplicity that the number of propagating modes at gate 1 and 2 are 1 and 2, respectively, at a certain frequency.

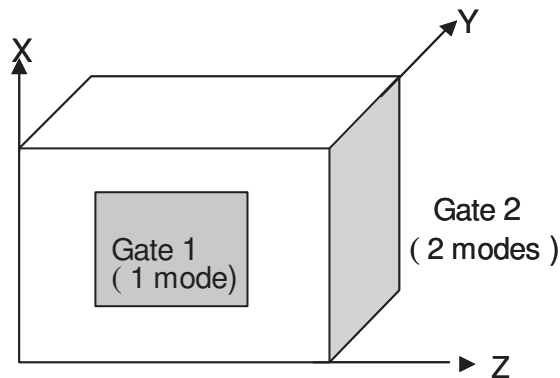


Fig. 7.7 Gate 1 lies in the XZ plane and gate 2 at XY plane.

For 2D calculation, equation 7.17 turns to equation 7.42 which deals with an eigenvalue problem assuming no source at the boundary and inside the structure (no internal port excitation). Dimension of M_{2D} is for gate 1 and 2 is $2.n_x.n_z \times 2.n_x.n_z$ and $2.n_x.n_y \times 2.n_x.n_y$ respectively. The components of this matrix list the material and dimensional information of the cells at the cross section of a particular gate. The matrix is built in such a way that the curl and divergence formulations in the Maxwell's equations are also preserved. Dimension of \vec{e} is for gate 1 and 2 is $2.n_x.n_z \times 1$ and $2.n_x.n_y \times 1$ respectively. λ stands for all the eigenvalues (λ_i).

$$M_{2D} \vec{e} = \lambda \vec{e}, \quad M_{2D} = M_{2D}(\varepsilon, \mu, \kappa, d, \omega) \quad (7.42)$$

Equation 7.42 is solved for each gate to get the eigenvalues and eigenvectors \vec{e}_i . Each eigenvalue refers to a specific mode and the propagation constant is calculated out of that eigenvalue. The corresponding eigenvector provides the mode pattern and lists in the vector all the transversal field components on the gate, on which the vectors are calculated. According to the assumptions at the beginning, three propagating modes have three eigenvalues. The first 2D solution at gate 1 provides eigenvalue λ_{11} and the corresponding eigenvector \vec{e}_{11} . The second 2D solution provides eigenvalues of λ_{21} and λ_{22} , and the corresponding eigenvectors \vec{e}_{21} and \vec{e}_{22} . \vec{e}_{11} lists the transversal fields components of mode 1 in the XZ plane on gate 1 where as \vec{e}_{21} and \vec{e}_{22} list the transversal field components in the XY plane of the mode 1 and 2 on gate 2 respectively.

In 3D calculation these eigenvectors are used for excitations (as source) at the waveguide ports. So for waveguide port excitation, equation 7.17 is modified to 7.43 assuming no relaxation and conduction current sources (\vec{r}_r and \vec{r}_c are equal to zero). \vec{r}_w stands for the waveguide port excitation and defined by 7.44 for k number of waveguide ports. w_1, w_2 etc are constants, represent the sum of amplitudes of the incoming and outgoing fields of the corresponding mode, and have unit in volt. For this particular example of three modes, 7.44 turns into 7.45. It should be noted that in \vec{e}_{11} the E_y components are zero and, in \vec{e}_{21} and \vec{e}_{22} the E_z components are zero – only cross sectional fields are necessary. Equation 7.43 is solved k times (in this example 3 times) numerically in order to get all the components of vector \vec{e} . The sets of values of w_i must be linearly independent as it is with the internal ports.

$$M \vec{e} = \vec{r}_w \quad (7.43)$$

$$\vec{r}_w = (w_1 \quad w_2 \quad w_3 \quad \dots \quad w_k) \begin{pmatrix} \vec{e}_1 \\ \vec{e}_2 \\ \vec{e}_3 \\ \dots \\ \vec{e}_k \end{pmatrix} = w_1 \vec{e}_1 + w_2 \vec{e}_2 + w_3 \vec{e}_3 + \dots + w_k \vec{e}_k \quad (7.44)$$

$$\vec{r}_w = w_1 \cdot \vec{e}_{11} + w_2 \vec{e}_{21} + w_3 \vec{e}_{22} = w_1 \cdot \begin{pmatrix} E_{x,1} \\ E_{x,2} \\ \dots \\ \dots \\ E_{x,n_{xyz}} \\ E_{y,1} = \mathbf{0} \\ E_{y,2} = \mathbf{0} \\ \dots \\ \dots \\ E_{y,n_{xyz}} = \mathbf{0} \\ E_{z,1} \\ E_{z,2} \\ \dots \\ \dots \\ E_{z,n_{xyz}} \end{pmatrix}_{11,k=1} + w_2 \begin{pmatrix} E_{x,1} \\ E_{x,2} \\ \dots \\ \dots \\ E_{x,n_{xyz}} \\ E_{y,1} \\ E_{y,2} \\ \dots \\ \dots \\ E_{y,n_{xyz}} \\ E_{z,1} = \mathbf{0} \\ E_{z,2} = \mathbf{0} \\ \dots \\ \dots \\ E_{z,n_{xyz}} = \mathbf{0} \end{pmatrix}_{21,k=2} + w_3 \begin{pmatrix} E_{x,1} \\ E_{x,2} \\ \dots \\ \dots \\ E_{x,n_{xyz}} \\ E_{y,1} \\ E_{y,2} \\ \dots \\ \dots \\ E_{y,n_{xyz}} \\ E_{z,1} = \mathbf{0} \\ E_{z,2} = \mathbf{0} \\ \dots \\ \dots \\ E_{z,n_{xyz}} = \mathbf{0} \end{pmatrix}_{22,k=3} \quad (7.45)$$

7.7 Improvements in the F3D Solver

The Weierstrass Institute for Applied Analysis and Stochastics (WIAS) improved the equation solver used for F3D-solver during the course of this thesis work. The F3D-solver based on the FDFD method is developed according to a Cartesian coordinate system where all the information of the materials, dimensions etc. as well as fields and sources are assigned to the system matrix and vector elements respectively cell by cell first of all in the x direction, then in the y direction and lastly in the z direction. The construction of the system matrix – i.e. the order of elements influences the convergence greatly, especially if a certain structure is simulated with PML overlapping regions.

The solver is modified by rearranging the system matrix $M = M(\epsilon_m, \mu_m, \kappa_m, d_m, \omega)$ of equation 7.46 where \vec{e} and \vec{b} are the unknown electric field vector to be solved and the input excitation vector respectively, and m specifies a particular cell. Rows and columns of M which possess only diagonal elements are separated in a way given by equation 7.47, where P_d is a permutation, D is a diagonal and H is a squared. Combining 7.46 and 7.47, we get a system of linear equations given by 7.48. The vector \vec{e}_d and \vec{e}_h can be calculated readily from equation 7.49 and 7.50 respectively.

$$M \cdot \vec{e} = \vec{b} \quad (7.46)$$

$$M \rightarrow P_d M P_d^T = \begin{pmatrix} D & \mathbf{0} \\ \mathbf{0} & H \end{pmatrix} \quad (7.47)$$

$$P_d M P_d^T \cdot P_d \vec{e} = P_d \vec{b} \Rightarrow \begin{pmatrix} D & \mathbf{0} \\ \mathbf{0} & H \end{pmatrix} \cdot \begin{pmatrix} \vec{e}_d \\ \vec{e}_h \end{pmatrix} = \begin{pmatrix} \vec{b}_d \\ \vec{b}_h \end{pmatrix} \quad (7.48)$$

where, $P_d \vec{e} = (\vec{e}_d, \vec{e}_h)^T$ and $P_d \vec{b} = (\vec{b}_d, \vec{b}_h)^T$

$$D \cdot \vec{e}_d = \vec{b}_d \quad (7.49)$$

$$H \cdot \vec{e}_h = \vec{b}_h \quad (7.50)$$

For the clarity, we define two solver versions: the new solver and the old solver. In the new version, H is rearranged as 7.51 according to different sorting rules (e.g. alternate, reverse, natural, ISODEG etc. [13]). The parameter ITR indicates in which order the graph of H is to be traversed. Whereas in the old version, H is rearranged as 7.50 without following any sorting rule (i.e. natural sorting rule). The upper left block B is block diagonal with block size IBZ and, E and C are sparse matrices [14,15]. The matrix B corresponds to the unknowns of independent sets. The procedure of forming independent sets is called Independent Set Ordering. This ordering transforms the original linear system 7.50 into the form given by 7.52.

$$H \rightarrow PHP^T = \begin{pmatrix} B & E^T \\ E & C \end{pmatrix} \quad (7.51)$$

$$\begin{pmatrix} B & E^T \\ E & C \end{pmatrix} \cdot \begin{pmatrix} \vec{y}_1 \\ \vec{y}_2 \end{pmatrix} = \begin{pmatrix} \vec{c}_1 \\ \vec{c}_2 \end{pmatrix} \quad (7.52)$$

where, $P \vec{e}_h = (\vec{y}_1, \vec{y}_2)^T$ and $P \vec{b}_h = (\vec{c}_1, \vec{c}_2)^T$

Since B is block diagonal, it is easy to eliminate \vec{y}_1 variable to obtain a system with only the variable \vec{y}_2 . The coefficient matrix (defined by 7.53) for this reduced system is the Schur complement S , which is still sparse.

$$S \cdot \vec{y}_2 = \vec{c}_2 - E \cdot B^{-1} \cdot \vec{c}_1 \quad (7.53)$$

where, $S = C - E \cdot B^{-1} \cdot E^T$

At the i^{th} level, the permutations P_i transform the matrices H_i with $H_0 = H$ in the form of 7.51. Then the following block factorization is computed [13, 14] :

$$\begin{pmatrix} I_i & \mathbf{0} \\ E_i B_i^{-1} & I_i \end{pmatrix} \cdot \begin{pmatrix} B_i & E_i^T \\ \mathbf{0} & C_i - E_i B_i^{-1} E_i^T \end{pmatrix} \cdot \begin{pmatrix} \vec{y}_{i,1} \\ \vec{y}_{i,2} \end{pmatrix} = \begin{pmatrix} \vec{c}_{i,1} \\ \vec{c}_{i,2} \end{pmatrix} \quad (7.54)$$

where, $\vec{y}_i = P_i \vec{e}_i = (\vec{y}_{i,1}, \vec{y}_{i,2})^T$ and $\vec{c}_i = P_i \vec{b}_i = (\vec{c}_{i,1}, \vec{c}_{i,2})^T$

The process is repeated recursively on the matrix $H_{i+1} = C_i - E_i B_i^{-1} E_i^T$ until a selected number of levels (LEV) is reached. The algorithm for solving equation 7.50 is described in the following [13]:

1. set $H_0 = H$, $\vec{e}_0 = \vec{e}_h$, $\vec{b}_0 = \vec{b}_h$
2. forward substitution : $i = 0, \dots, \text{LEV}-1$
 - (a) compute $P_i : P_i H_i P_i^T$, $\vec{y}_i = P_i \vec{e}_i$, $\vec{c}_i = P_i \vec{b}_i$
 - (b) compute $\vec{e}_{i+1} = \vec{y}_{i,2}$, $\vec{b}_{i+1} = \vec{c}_{i,2} - E_i B_i^{-1} \vec{c}_{i,1}$
 - (c) compute $H_{i+1} = C_i - E_i B_i^{-1} E_i^T$
3. solve $H_{LEV} \cdot \vec{e}_{LEV} = \vec{b}_{LEV}$
4. backward substitution : $i = \text{LEV}-1, \dots, 0$
 - (a) compute $\vec{y}_{i,2} = \vec{e}_{i+1}$, $\vec{y}_{i,1} = B_i^{-1} (\vec{c}_{i,1} - E_i^T \vec{y}_{i,1})$
 - (b) compute $\vec{e}_i = P_i^T \vec{y}_i$

In order to improve the robustness of the factorization (7.54) the numerical values are also considered. In this regard, a parameter TOL_ISO is used to filter out the rows that are least diagonally dominant to the complement set C_i in any independent set strategy [14].

Using Krylov-subspace method $H_{LEV} \cdot \vec{e}_{LEV} = \vec{b}_{LEV}$ is solved with SSOR preconditioning, where this system of linear algebraic equations is first transformed to 7.55, then is preconditioned as given by 7.56 and is finally solved for $\vec{\tilde{e}}$. In M_a and M_b [51], ω denotes the relaxation parameter of the SSOR preconditioning and L is the lower triangular matrix of \tilde{H} .

$$\tilde{H} \cdot \vec{\tilde{e}} = \vec{\tilde{b}} \quad (7.55)$$

where, $\tilde{H} = D_d^{-\frac{1}{2}} \cdot H_{LEV} \cdot D_d^{-\frac{1}{2}}$, $\vec{\tilde{e}} = D_d^{\frac{1}{2}} \cdot \vec{x}_{LEV}$, $\vec{\tilde{b}} = D_d^{-\frac{1}{2}} \cdot \vec{b}_{LEV}$ and $D_d = \text{diag}(H_{LEV})$

$$M_a^{-1} \tilde{H} M_b^{-1} \cdot M_b \vec{\tilde{e}} = M_a^{-1} \vec{\tilde{b}} \quad (7.56)$$

where, $M_a M_b = (M_a M_b)^T$, $M_a = (I + \omega L)$, $M_b = (I + \omega L^T)$ and $0 < \omega < 2$.

7.8 Acronyms and Symbols

- ABC - Absorbing Boundary Condition
- BCB - Benzocyclobutene
- BMBF - Bundes Ministerium für Bildung und Forschung
- CPU - Computer Processing Unit

CPW - Co-Planar-Waveguide
 EM - Electromagnetic
 FBH - Ferdinand Braun Institute für Höchstfrequenz Technik
 FD - Finite Difference
 FDFD - Finite Difference Frequency Domain
 FDTD - Finite Difference Time Domain
 FEM - Finite Element Method
 GaAs - Gallium-Arsenid
 HBT - Hetero-junction Bipolar Transistor
 HEMT - High Electron Mobility Transistor
 LTCC - Low Temperature Co-fired Ceramic
 MMIC - Monolithic Microwave Integrated Circuit
 MS - Micro-Strip
 PEC – Perfect Electric Conductor
 PML - Perfectly Matched Layer
 PPP - Power Part in PML
 PPL - Parallel Plate (Mode)
 SSOR - Symmetric Successive Over Relaxation (Procedure)
 TE - Transverse Electric
 TM - Transverse Magnetic
 TEM - Transverse Electro-Magnetic
 TLM - Transmission Line Method
 VCO - Voltage Controlled Oscillator
 WIAS - Weierstrass Institute for Applied Analysis and Stochastics
 2D - Two Dimensional
 3D - Three Dimensional

α - Attenuation constant

β - Phase constant

β_0 - Phase constant in open space

λ - Wave length

μ - Permeability

ε - Permittivity

ε_r - Relative Permittivity

ε_{r-eff} - Effective Relative Permittivity

j - $\sqrt{-1}$

r_{th} - Nominal reflection coefficient

η - Tensor elements

J_e - Conduction current density

q_v - Space charge density

$\omega = 2\pi f$ ($\pi = 3.141592654$, f = frequency in Hz)

\vec{E} - Electric field intensity

\vec{H} - Magnetic field Intensity

$\nabla \times \nabla \times$ - curl curl operator

$\nabla \nabla \cdot$ - grad div operator

8 Literature

FDFD/FDTD Method:

- [1] K. S. Yee, "Numerical solution of initial boundary value. problems involving Maxwell's equations in isotropic. media", IEEE Transactions on Antennas and Propagation, vol. 14, Nr. 5, pp. 302-307, 1966
- [2] T. Weiland, "On the Unique Solution of Maxwellian Eigenvalue Problems. in Three Dimensions", Particle Accel., vol. 17, pp. 227–242, 1985
- [3] T. Weiland, "Thee Dimensional Resonator Mode Computation by Finite Difference Method", IEEE Transactions on Magnetics, vol. Mag-21, No. 6, pp. 2340–2343, Nov. 1985
- [4] D. Schmitt, T. Weiland, "2D and 3D Computations of Eigenvalue Problems", IEEE Transactions on Magnetics, vol. 28, Nr. 2, pp. 1793–1796, Mar. 1992
- [5] A. Christ, H. L. Hartnagel, "Three-Dimensional Finite-Difference Method for the Analysis of Microwave-Device Embedding", IEEE Transactions on Microwave Theory and Tech., vol. MTT-35, No. 8, pp. 688-696, Aug. 1987
- [6] K. Beilenhoff, W. Heinrich, "Improved Finite-Difference Formulation in Frequency Domain for Three-Dimensional Scattering Problems", IEEE Transactions on Microwave Theory and Tech., vol. MTT-40, No. 3, pp. 540-546, Mar. 1992
- [7] K. Beilenhoff, "Simulation und Modellierung von Leitungs-Diskontinuitäten und -Verzweigungen für monolithisch integrierte Millimeterwellenschaltungen", Dissertation, TH Darmstadt, 1995
- [8] T. Weiland, "Elektromagnetische CAD – Rechnergestützte Methoden zur Berechnung von Feldern", Skriptum zur Vorlesung Feldtheorie 2, TU-Darmstadt.
- [9] K. S. Kunz and R. J. Luebbers, "The Finite Difference Time Domain Method for Electromagnetics", CRC Press, London.

F3D Solver:

- [10] G. Hebermehl, R. Schlundt and H. Zscheile, "Eigenmode solver for microwave transmission lines", Compel-Int J. Comput. Math. Electri. Electron. Eng., vol. 39, pp. 910-915, Jun. 1991.
- [11] G. Hebermehl, R. Schlundt, H. Zscheile, W. Heinrich, "Improved Numerical Solutions for the Simulation of Monolithic Microwave Integrated Circuits", Weierstrass-Institut für Angewandte Analysis und Stochastik, Preprint No. 236, ISSN 0946 – 8633, Berlin 1996.
- [12] G. Hebermehl, F. K. Hübner, R. Schlundt, T. Tischler, H. Zscheile, W. Heinrich, "On the Computation of Eigen Modes for Lossy Microwave Transmission Lines Including Perfectly

Matched Layer Boundary Condition”, *Compel-Int J. Comput. Math. Electri. Electron. Eng.*, vol. 13, pp. 948-946, Jun. 2001.

[13] G. Hebermehl, J. Scheffter, R. Schlundt, T. Tischler, H. Zscheile, W. Heinrich, “Simulation of Microwave and semiconductor laser structures including PML : Computation of the eigenmode problem, the boundary value problem, and the scattering matrix”, *Scientific Computing in Electrical Engineering*, Springer Verlag, pp. 203-214, 2006.

[14] Y. Saad, A. Soulaïmani and R. Touihri, “Adapting algebraic recursive multilevel solvers (ARMS) for solving CFD problems”, *Appl. Numer. Math.*, 51, pp. 305-327, 2004

[15] Y. Saad, “Iterative Methods for Sparse Linear Systems”, PWS Publishing Company, 1996.

PML:

[16] J.P Berenger, “A perfectly matched layer for the absorption of electromagnetic waves,” *J. Comput. Phys.*, vol. 114, pp. 185-200, Oct. 1994.

[17] R. Mittra and U. Pikel, “ A new look at the perfectly matched layer(PML) concept for the reflectionless absorption of electromagnetic waves”, *IEEE Microwave Guided Wave Letter*, vol. 5, pp. 84-87, Mar. 1995.

[18] Z. S. Sacks et al,“ A Perfectly Matched Anisotropic Absorber for Use as an Absorbing Boundary Condition”, *IEEE Trans. Antenna and Propagations.*, vol. 43, pp. 1460-1463, Dec. 1995.

[19] S. D. Gedney, “An Anisotropic Perfectly Matched Layer Absorbing Medium for the Truncation of FDTD Lattices,” *IEEE Trans. Antenna and Propagations.*, vol. 44, pp. 1630-1639, Dec. 1996.

[20] T. Tischler and W. Heinrich,“ The Perfectly Matched Layer as lateral Boundary in Finite-Difference Transmission-Line Analysis”, *IEEE Trans. Microwave Theory Tech.*, vol. 48, pp. 2249-2253, December. 2000.

[21] T. Tischler and W. Heinrich,“ Accuracy Limitations of Perfectly Matched Layers in 3D Finite Difference Frequency-Domain Method”, *IEEE MTT-S Int. Microwave Symp. Dig.*, vol 3, pp. 1885-1888, Jun. 2002.

[22] W. C. Chew and W. H. Weedon, “ A 3-D perfectly Matched Medium from Modified Maxwell’s Equation with Stretched Coordinates”, *Microwave Optical Technol. Lett.*, vol.7, no. 13. pp. 599-604, Sep. 1994.

[23] J. Fang and Z. Wu, “Generalized Perfectly Matched Layer for the Absorption of Propagating and Evanescent Waves in Lossless and Lossy Media”, *IEEE Trans. Microwave Theory Tech.*, vol. 44, nr. 12, pp. 2216-2222, Dec. 1996.

[24] P. K. Talukder, F. J. Schmückle, R. Schlundt, and W. Heinrich, "Optimizing the FDFD Method in Order to Minimize PML-Related Numerical Problems", IEEE MTT-S Int. Microwave Symp. Dig., vol 3., pp. 293-296, Jun. 2007.

[25] T. Tischler, "Die Perfectly Matched Layer Randbedingung in der Finite-Differenzen-Methode im Frequenzbereich : Implementierung und Einsatzbereiche", Dissertation, TU Berlin, 2003

Internal Ports / Lumped Elements:

[26] W. Thiel and W. Menzel, "Full-wave design and optimization of mm-wave diode-based circuits in finline technique" IEEE Trans. Microwave Theory Tech., vol. 47, Nr. 12, pp. 2460-2466, Dec. 1999.

[27] P. Schuh, H. Bilzer, W. Menzel, J. Kiwitt and M. Pitschi, "Full-wave Characterization of RF Ceramic Packages", 33rd European Microwave Conference 2003 – Munich, Germany.

[28] L. Borzetta, F. Alimenti, P. Ciampolini, P. Mezzanotte, L. Rosseli and R. Sorrentino, "Numerical parasitic reactances at the interface between FDTD mesh and lumped elements", IEEE MTT-S Int. Microwave Symp. Dig., vol 3., pp. 1585-1588, Jun. 1999.

[29] L. Borzetta, F. Alimenti, P. Ciampolini, P. Mezzanotte, L. Rosseli and R. Sorrentino, "Numerical parasitic reactances at the interface between FDTD mesh and lumped elements", IEEE MTT-S Int. Microwave Symp. Dig., vol 3., pp. 1585-1588, Jun. 1999.

[30] A. Taflove, "Computational Electrodynamics – The Finite Difference Time Domain Method", Arctech House, Boston, 1995

Slot Antenna:

[31] C.G. Christodoulou, P.F. Wahid, "Fundamentals of Antennas," SPIE Press, P.O. Box 10, Bellingham, Washington, USA.

[32] C.A. Balanis, "Antenna Theory: Analysis and Design," New York, Wiley 1982, 1996.

[33] German patent No. 10 2004 014 018 Mikrowellenantenne für in Flip-Chip Technologie-Hergestellte Halbleiterbaugruppen

[34] C. Meliani, P. Talukder, J. Hilsenbeck, M. Huber, G. Böck and W. Heinrich, "Integrated Circuits and 3-D-Packaging for Low-Power 24 GHz Front End," Frequenz 3-4, 2004, Vol. 58, pp. 74-79.

[35] P. Talukder, F.J. Schmückle, and W. Heinrich, "A Novel 24 GHz 4-Quadrant Slot Antenna," accepted for presentation at German Microwave Conference (GeMic), 2006, Karlsruhe, Germany.

[36] P. Talukder, M. Neuner, C. Meliani, F.J. Schmückle and W. Heinrich, "A 24 GHz Active Antenna in Flip-chip Technology with Integrated Frontends", IEEE MTT-S Int. Microwave Symp. Dig., pp. 1176-1179, Jun. 2006.

Others:

[37] F. Gardiol, "Microstrip Circuit", John Willey and Sons, Inc., New York

[38] F. Schnieder, T. Tischler and W. Heinrich, "Modelling Dispersion and Radiation Characteristics of Conductor-Backed CPW with Finite Ground Width", IEEE Trans. Microwave Theory Tech., vol. 51, nr. 1, pp. 137-143, Dec. 2003.

[39] W. Heinrich, F. Schnieder and T. Tischler, "Dispersion and Radiation Characteristics of Conductor-Backed CPW with Finite Ground Width", IEEE MTT-S Int. Microwave Symp. Dig., Vol. 3 pp. 1663-1666, Jun. 2000.

[40] Microwave Studio (MWS) from CST, Darmstadt, Germany, <http://www.cst.com/>

[41] R. K. Hoffman, "Integrierte Mikrowellenschaltungen", Springer-Verlag, Berlin, 1983.

[42] R. E. Collin "Field Theory of Guided Waves", Second Edition, IEEE Press.

[43] C. A. Balanis, "Advanced Engineering Electromagnetics", John Willey and Sons, Inc., New York

[44] C. Christopoulos, "Transmission-line modelling (TLM): A brief introduction and recent advances", IEE Colloquium, No. 2, pp. 1/1-1/6, Apr. 1993.

[45] N. O. Sadiku, "Numerical Techniques in Electromagnetic", CRC Press, London, 2000

[46] D. Pozar, "Microwave Engineering", Addison-Wesley Publishing Company, 1990.

[47] W. Heinrich, F. Schnieder, T. Tischler, "Dispersion and radiation characteristics of conductor-backed CPW with finite ground width" IEEE Trans. Microwave Theory Tech., vol. 3, Nr. 3, pp. 1663-1666, 2000.

[48] W. Heinrich, F. Schnieder, T. Tischler, "Modelling dispersion and radiation characteristics of conductor-backed CPW with finite ground width" IEEE Trans. Microwave Theory Tech., vol. 51, Nr. 1, pp. 137-143, 2003.

[49] J. D. Kraus, "Antennas", McGraw – Hill, Inc. New York, second edition.

[50] Gerschgorin Circle: Weisstein, Eric W. "Gershgorin Circle Theorem." From *Math World* - A Wolfram Web Resource. <http://mathworld.wolfram.com/GershgorinCircleTheorem.html>

[51] R. Schlundt, G. Hebermehl, W. Heinrich, H. Zscheile, "Iterative Solution of Systems of Linear Equations in Microwave Circuit Using a Block Quasi-Minimal Residual Algorithm", Lecture Notes in Computational Science and Engineering, Springer Verlag (Scientific Computing in Electrical Engg.), vol. 18, pp. 325-333, 2001.

[52] H. Klockenhoff, "Optimiertes Design von Mikrowellen-Leistungstransistoren und Verstärkern im X-Band", Dissertation, TU Berlin.

9 Curriculum Vitae

Personal details:

Name: Prodyut Kumar Talukder
Father: Khagendra Nath Talukder
Mother: Gita Rani Roy
Date of birth: 09.03.1976 (Netrakona, Bangladesh)
Nationality: Bangladeshi.
Marital status: married with Aditi Gupta since 22 Feb. 2004
Email: pktalukder@ieee.org

Academic qualifications:

1991

- SSC (Secondary School Certificate Examination)
- Anjuman Govt Model High School, Netrakona, Bangladesh

1991 - 1993

- HSC (Higher Secondary School Certificate)
- Dhaka College, Dhaka, Bangladesh

01.1995 - 06.2000

- B. Sc. in Electrical and Electronic Engineering
- Bangladesh University of Engineering and Technology (BUET), Dhaka, Bangladesh

10.2000 - 10.2002

- M. Sc. in Communication and Media Engineering
- The University of Applied Sciences (UAS), Offenburg, Germany

11.2002 - 07.2008

- PhD being pursued
- Microwaves Department, Ferdinand-Braun-Institute for High Frequency Engineering (FBH), Berlin, Germany

Innovationen mit Mikrowellen und Licht

Forschungsberichte aus dem Ferdinand-Braun-Institut für Höchsthfrequenztechnik

Herausgeber: Prof. Dr. G. Tränkle, Prof. Dr.-Ing. W. Heinrich

- Band 1:** **Thorsten Tischler**
Die Perfectly-Matched-Layer-Randbedingung in der
Finite-Differenzen-Methode im Frequenzbereich:
Implementierung und Einsatzbereiche
ISBN: 3-86537-113-2, 19,00 EUR, 144 Seiten
- Band 2:** **Friedrich Lenk**
Monolithische GaAs FET- und HBT-Oszillatoren
mit verbesserter Transistormodellierung
ISBN: 3-86537-107-8, 19,00 EUR, 140 Seiten
- Band 3:** **R. Doerner, M. Rudolph (eds.)**
Selected Topics on Microwave Measurements,
Noise in Devices and Circuits, and Transistor Modeling
ISBN: 3-86537-328-3, 19,00 EUR, 130 Seiten
- Band 4:** **Matthias Schott**
Methoden zur Phasenrauschverbesserung von
monolithischen Millimeterwellen-Oszillatoren
ISBN: 978-3-86727-774-0, 19,00 EUR, 134 Seiten
- Band 5:** **Katrin Paschke**
Hochleistungsdiodenlaser hoher spektraler Strahldichte
mit geneigtem Bragg-Gitter als Modenfilter (α -DFB-Laser)
ISBN: 978-3-86727-775-7, 19,00 EUR, 128 Seiten
- Band 6:** **Andre Maaßdorf**
Entwicklung von GaAs-basierten Heterostruktur-Bipolartransistoren
(HBTs) für Mikrowellenleistungszellen
ISBN: 978-3-86727-743-3, 23,00 EUR, 154 Seiten



Cuvillier Verlag

Internationaler wissenschaftlicher Fachverlag

